RICE UNIVERISITY

Engineering Application-Specific Plasmonic Nanoparticles: Quantitative Measurements and Precise Characterization

by

Lindsey J. E. Anderson

A THESIS SUBMITTED
IN PARTIAL FULFILLMENT OF THE
REQUIREMENTS FOR THE DEGREE
Doctor of Philosophy

APPROVED, THESIS COMMITTEE:

Jason Hafner
Associate Professor of Physics
and Astronomy
Associate Professor of Chemistry

Kevin Kelly
Associate Professor of Electrical and
Computer Engineering

Naomi Halas
Stanley C. Moore Professor in
Electrical and Computer
Engineering.
Professor of Biomedical
Engineering, Chemistry, Physics &
Astronomy

HOUSTON, TX
March 2013

Abstract

Engineering Application-Specific Plasmonic Nanoparticles: Quantitative Measurements and Precise Characterization

by

Lindsey Anderson

Nobel metal nanoparticles that exhibit plasmon resonances in the visible and near infrared have been of great interest in recent years. Strong light-matter interactions on the nanoscale have a range of interesting properties that may be useful in applications in medicine, sensing, solar energy harvesting and information processing. Depending on the application, particle materials and geometries can be optimized for performance. A novel method of quantifying individual nanoparticle scattering cross sections by comparing experiments with analytical theory for gold nanospheres is proposed and utilized. Results show that elongated particles scatter very brightly for their volumes. This brightness is due to a strong longitudinal plasmon resonance that occurs in the near infrared – where gold has minimal loss. Elongated particles, such as nanorods, are therefore ideal for applications that rely on particles scattering brightly from small spaces, such as biological imaging.

Next, gold nanobelts are discussed and characterized. These novel structures are akin to nanowires, but with a small, rectangular cross-sectional geometry. Gold nanobelts are shown to exhibit a strong transverse resonance that has never been reported previously in nanowires. The transverse resonance shifts linearly with cross-sectional aspect ratio. Other interesting products from the nanobelt synthesis, tapered and split nanobelts, are discussed. Gold nanobelts also support longitudinal propagating plasmons,

and have the smallest cross-sectional area of any elongated plasmonic structure that has been reported to do so. By analyzing the output tip signal of propagating plasmons for nanobelts of different lengths, the decay length is measured. Finite Difference Time Domain simulations and polarization measurements show the fundamental, azimuthally symmetric mode is very strong for thin structures such as these, but decays much more quickly than a higher-order mode, which begins to dominate at longer lengths. The cross-sectional mode area is given, illustrating the high confinement of plasmons in these structures. A figure of merit that takes into account both confinement and propagation length is calculated to be 1300 for the higher-order mode, the highest reported for nanoscale plasmonic waveguides. The high figure of merit makes gold nanobelts excellent candidates for studying strong coupling between plasmonic structures and objects that exhibit quantum behavior.

Acknowledgements

I consider myself very lucky to have had Jason Hafner as a mentor and friend. His love for science is contagious and I have learned so much by working with him in the lab. His availability, experimental expertise and outside-the-box thinking were of great assistance in all of my projects. Jason is respectful and always wants the best for his students, making my graduate school experience a very enjoyable. I want to thank my labmate Courtney Payne, chemist extraordinaire, for all of the great projects we have worked on together over the past several years and also for her kindness and friendship. Thanks to previous Hafner Lab group members Kathryn Mayer, Seunghyun Lee, Robbie Fraleigh and Yi Yang for all of their help, especially when I was getting started and current lab members James Matthews and Josue Lopez. The nanophotonics community at Rice has been a great source of learning, discussions and collaborations-acknowledgements especially to the groups of Naomi Halas, Stephan Link and Peter Nordlander. Thanks to Dimitri Lapotko for our collaboration working with photothermal nanobubbles and Yu-Rong Zhen for his electromagnetic simulations and insight to the deeper physics of my nanobelt experiments.

I am so grateful to my family for being so supportive and their enthusiasm about my work in science. Also, my friends and fellow graduate students have been a family of sorts, making Houston a home - Jed Pixley, Brian DeSalvo, Aditya Shashi, Marcel LaFlamme and Sara Haber. Special thanks to Jorge Zuloaga and Brent and Guinevere Kappos for fun conversations and making me feel relaxed. Last, but not least, Peri and Lexi, my closest companions.

Contents

List of Figures

List of Tables

List of Equations

1 Introduction

Plasmons polaritons are collective oscillations of the free electron gas density in a metal. The oscillating field of electromagnetic radiation excites plasmon modes which then propagate on the metal surface. Classically, the electrons can be thought of as an incompressible fluid and the SPR likened to a wave on this fluid. In this analogy, the incident light can be thought of as a "rock" hitting a "pond" of electrons, causing surface waves. Under certain excitation conditions one gets a strong coupling known as surface plasmon resonance (SPR). For metal particles on the order of or much smaller than the wavelength of incident light, a special, highly localized type of plasmon resonance occurs. Due to the small size of the metal particle compared with the wavelength of the light, the particle is effectively seeing the same electric field throughout its volume at any given time. The free electrons in the particle then *collectively* oscillate in what is termed a localized surface plasmon resonance (LSPR). On resonance, the extremely high confinement of the electromagnetic energy in and around the nanoparticle results in bright scattering, strong absorption, and intense electric field enhancements. [1-3]

Noble metal nanoparticles and nanostructures exhibit LSPR at visible and near-infrared frequencies. Over the past decade, a wide variety of plasmonic gold and silver structures have been fabricated through "bottom-up" chemical methods. [1, 4, 5] Their physical properties have generated great interest in these materials for applications in biomedical therapies and diagnostics.[6-8] Bright resonant scattering is useful for microscopic imaging contrast and microscopic particle tracking.[9, 10] Nanoparticles with sharp tips and gaps between nanoparticles create regions of highly enhanced

electromagnetic fields which amplify vibrational spectroscopies for sensing applications.[11, 12] Plasmonic nanoparticles can be coupled to fluorescent dyes or quantum dots to manipulate radiative decay rates and directions, thus fundamentally manipulating optical emission.[13, 14] All of these applications rely to some extent on the ability to tune nanoparticle plasmon resonances to match a biological window of tissue transparency, to coincide with an emitter excitation, or simply to match a laser source. The capability to tune the plasmon resonance has played a crucial role in stimulating the current interest in plasmonics.

Nanoparticle plasmon resonances can be characterized by a number of techniques, including ensemble spectral extinction measurements,[15] single particle spectral scattering measurements,[16-26] near field optical microscopy,[27, 28] electron energy loss spectroscopies,[29, 30] and cathodoluminsecence.[31, 32] Single nanoparticle studies are particularly powerful for characterizing plasmon resonances since they avoid the confounding effect of nanoparticle heterogeneity. They are often carried out by dark field microspectroscopy at high numerical aperture (>0.5), and have been applied to a variety of complex nanoparticle shapes for fundamental studies of the nature of the plasmon resonance.[16-23, 25]

For extended structures, surface plasmons propagate along the metal surface at the frequency of the incoming light, but with shorter wavelength. This plasmon propagation phenomenon may be used to transport optical information. [1, 6, 33-36] For example, light can be coupled into surface plasmons in a two-dimensional film through a defect, and its propagation can be manipulated by nanostructures within the film.[37-39] Recently there has been interest in plasmon propagation in one-dimensional plasmonic nanowires.[40-45] Long-

range plasmons can have propagation lengths of several microns in gold and silver for visible and NIR incident wavelengths.[46] Here light can be coupled into and out of the nanowires through symmetry broken sites such as tips, kinks, or nanoparticle-nanowire junctions, creating a plasmonic waveguide.[47-49] The coupling between propagating nanowire plasmons and nearby quantum dots could enable the integration of plasmonic structures into nanometer scale optoelectronic devices.[50-55] Nanowire propagating plasmon modes have been studied largely with silver nanowires that have cross sections of 75 – 260 nm in diameter.[42, 43, 47, 56] While these efficiently couple, transport, and emit light, their large size leads to transport based on a mixture of higher order plasmonic modes and may limit the strength of interactions with nearby emitters and other plasmonic structures.[57]

The work here focuses on the precise characterization of both the optical and geometrical properties of structures on the nano- and mirco-scale. Plasmonic nanoparticles are known for their intense scattering, which is visible in dark field microscopy, where count rates are measured with a charge-coupled device (CCD). A quantitative measure of scattering for spherical particles can be given as an effective cross-sectional area by the Mie Solution. There is not, however, an analytical solution for the scattering cross sections of nanoparticles of complex shapes. Chapter 2 outlines theory and experiments dealing with the quantification of single nanoparticle LSPR scattering cross sections. By comparing spherical particle scattering to the Mie Solution, a constant relating dark field scattering CCD count rates to the scattering cross section is obtained. This constant is then applied to gold nanorods and bipyramids and a quantitative comparison of nanoparticle scattering is given. The purpose of this work is to

optimize particle shapes that are used in applications that require particles that scatter brightly. In chapter 3, a new class of elongated plasmonic nanostructures is introduced: gold nanobelts. These structures exhibit bright, narrow plasmon resonances across their width and often change color along their length – containing many colorful resonances in a single structure. Most nanowires studied to date are too large in diameter to exhibit these narrow, localized plasmon resonances. Gold nanobelts also support propagating surface plasmon modes and have the smallest measured cross-sectional area of any elongated structures that have been reported to do so. Gold nanobelts are very interesting because they are the first reported single structure that supports both a localized transverse plasmon mode and two detectable long-range propagating plasmon modes. The properties of these types of plasmon modes are explored and discussed. Due to their small size, gold nanobelts display a high level of plasmon confinement, making them interesting for applications involving strong coupling between plasmons and quantum objects.

2 Quantifying Gold Nanoparticle Scattering Cross Sections

2.1 Background and Theory

If one imagines the electron density along a line around the circumference of the surface of a small, spherical particle, the fundamental plasmon mode would have two peaks: one positive and one negative, as shown in Figure 1. For higher order modes, which are very weak for increasing small particle size, the number of electron surface density peaks will increase. As particle size increases, higher order modes become stronger - with the total number of peaks increasing as powers of two. The asymmetry of mode orders that are not powers of two make those mode orders energetically unfavorable.

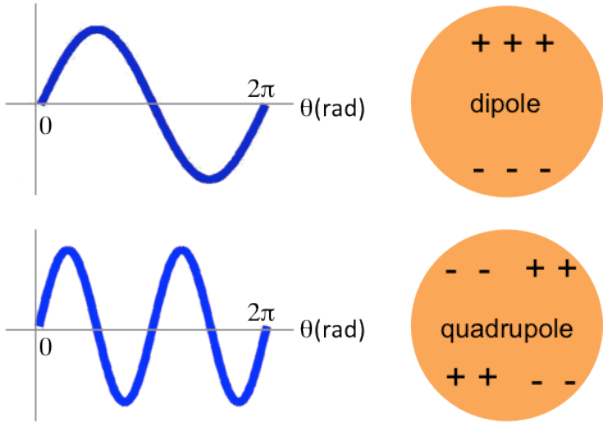

Figure 1 Electron surface charge density of a spherical nanoparticle with a dipolar (top) and quadrupolar (bottom) plasmon resonance.

The total amount of incident light that a nanoparticle either scatters or absorbs is referred to as the extinction (Figure 2). In other words, extinction quantifies how much light the particle "took out of" the incident wave. The amount a given particle scatters or absorbs at a given wavelength is quantified by a cross section. Nobel metal nanoparticles

exhibit a resonance in the visible/NIR, meaning there is a sharp distribution of wavelengths that interact strongly with the particle in that energy region. Cross sections are measured in the same units as a spatial area (m^2, for example), but gives an effective cross-sectional area for that particle as far as its scattering or absorption properties are concerned.

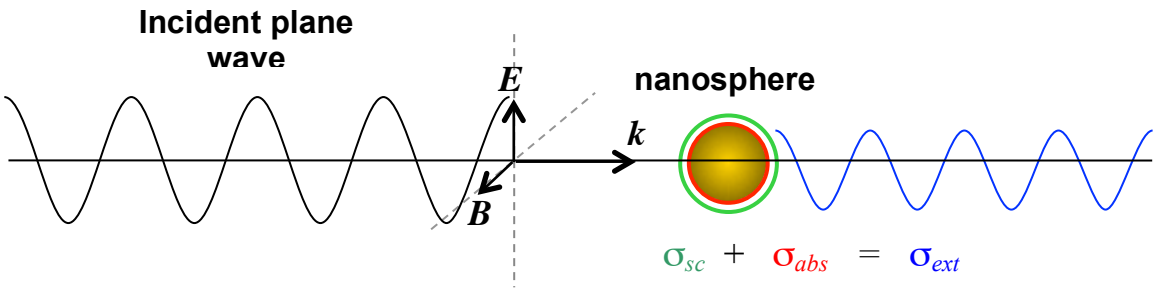

Figure 2 Schematic of an electromagnetic wave incident on a small gold sphere. Some of the incident radiation is absorbed by the particle, some is scattered, and the remainder continues traveling in the *k*-direction.

For sub-wavelength sized nanoparticles, the off-resonant optical extinction cross section is smaller than the cross section of the particle itself due to diffraction (Figure 3a). On resonance, however, the extinction cross section can be larger than the physical cross section (Figure 3b). The dashed line in Figure 3b is the effective size of the particle when on resonance. [58]

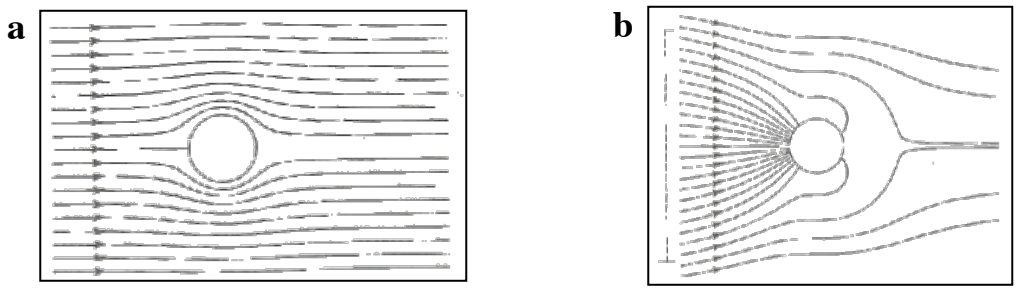

Figure 3 Field lines of the total Poynting vector (excluding the scattered) around a small aluminum sphere illuminated a) off resonance and b) on resonance. The dashed line in b indicates the effective absorption radius of the sphere.

While previous studies of single particle spectra have been well suited to measuring the resonant wavelength and spectral width, there are few reports on the precise experimental characterization of the amplitude of the resonance, which corresponds to the cross section.[59, 60] Such characterization could be valuable for determining nanoparticle concentrations, predicting heat generation and scattering signals, testing the accuracy of numerical simulations, and possibly evaluating near field enhancements.[61, 62] For intracellular imaging applications, particles need to be small enough to penetrate the cell wall, yet scatter a sufficient amount of detectable light. By quantifying the scattering cross section of different shaped nanoparticles, it will be possible to make particle choices that are application specific.

In their seminal paper, Schultz *et al* used single silver nanoparticles as specific biological labels for microscopic imaging, and estimated a single nanoparticle to provide approximately 10^6 more signal than a fluorescein molecule and approximately 10^5 more signal than a quantum dot.[63] The past decade has seen major advances in the synthesis of gold and silver nanoparticles with complex shapes and sizes that have also been considered for biological labeling. However, the measurements and estimates quoted

above were for an 80 nm diameter silver nanoparticle, and the scattering signal from other plasmon resonant nanoparticles varies widely. The scattering cross section is strongly dependent on the nanoparticle size and shape,[64] the spectral variation of the metal dielectric properties, and the refractive index of the medium. In fact, the peak total scattering cross section for gold and silver nanospheres between 10 and 100 nm diameters varies over five orders of magnitude Figure 4.

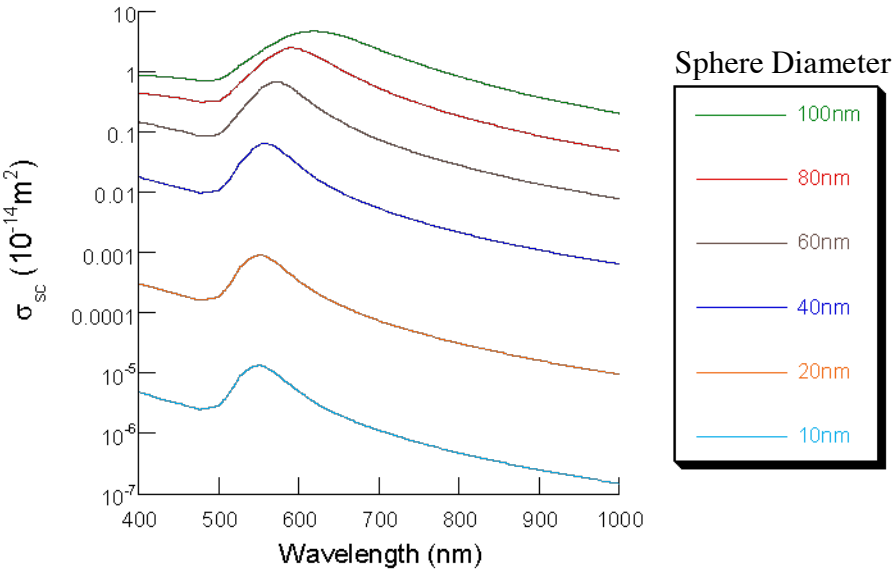

Figure 4 The total scattering cross section for gold nanospheres in a medium of refractive index 1.515.

The scattering signal collected in imaging applications will depend on the illumination angle and differential scattering cross section integrated over the solid angle of the imaging lens, so predictions based on the total scattering cross section can be misleading. While there have been some numerical simulations of the effect of nanoparticle size and shape on the magnitude of the scattering cross section,[65-67] the lack of direct experimental comparison has left plasmon resonant nanoparticles' scattering

properties ambiguous and at times perhaps even overstated. Here, an effort is presented to quantify the scattering from plasmon resonant nanoparticles with complex shapes by dark field microspectroscopy.

2.1.1 Scattering Cross section of a Sphere (Mie Solution)

The problem of scattering from a sphere due to an incident plane wave can be solved analytically. Following Bohren and Huffman,[58] a realizable time-harmonic electromagnetic field in a linear, isotropic, homogeneous medium must satisfy the wave equation:

$$\nabla^2\mathbf{E} + k^2\mathbf{E} = \mathbf{0} \qquad \nabla^2\mathbf{H} + k^2\mathbf{H} = \mathbf{0}$$

where $k^2=\omega^2\varepsilon\mu$, and have no divergence:

$$\nabla \cdot \mathbf{E} = \mathbf{0} \qquad \nabla \cdot \mathbf{H} = \mathbf{0}$$

Additionally, **E** and **H** are not independent:

$$\nabla \times \mathbf{E} = i\omega\mu\mathbf{H} \qquad \nabla \times \mathbf{H} = -i\omega\varepsilon\mathbf{E}$$

Vector functions that satisfy these requirements can be constructed:

$$\mathbf{M} = \nabla \times (\mathbf{c}\varphi) \qquad \mathbf{N} = \frac{\nabla \times \mathbf{M}}{k}$$

where φ is a scalar function and **c** is an arbitrary constant. **M** and **N** have all of the required properties of an electromagnetic field: they satisfy the vector wave equation, they are divergence free, and the curl of one is proportional to the other. Furthermore, it can be shown that if **M** satisfies the vector wave equation, φ satisfies the scalar wave equation. Therefore, the problem of finding solutions to the field equations reduces to the simpler problem of finding solutions to the scalar wave equation (for φ). φ is termed *the generating function* for the *vector harmonics* **M** and **N** and **c** is called the *guiding* or *pilot*

vector. Due to the spherical symmetry of the problem, functions φ that satisfy the wave equation in spherical coordinates are chosen and **c** is chosen to be the radius vector **r**.

In spherical coordinates, φ is of the form:

$$\varphi(r,\theta,\phi) = R(r)\,\Theta(\theta)\,\Phi(\phi)$$

Inserting this into the wave equation in spherical coordinates, the result is 3 separated equations:

$$\frac{d^2\Phi}{d\varphi^2} + m^2\Phi = 0 \tag{1}$$

$$\frac{1}{\sin\theta}\frac{d}{d\theta}\left(\sin\theta\frac{d\Theta}{d\theta}\right) + \left[n(n+1) - \frac{m^2}{\sin^2\theta}\right]\Theta = 0 \tag{2}$$

$$\frac{d}{dr}\left(r^2\frac{dR}{dr}\right) + \left[k^2r^2 - n(n+1)\right]R = 0 \tag{3}$$

where m and n are integers. For Φ, the linearly independent solutions are $\Phi_e = \cos m\phi$ and $\Phi_o = \sin m\phi$. Solutions to (2) are the associated Legendre functions of the first kind $P_n^m(\cos\theta)$ of degree *n* and order *m* (*n* = *m*, *m+1*,…). The Legendre functions ultimately give the angular dependence of the scattering cross section. Finally, the linearly independent solutions to (3) are the spherical Bessel functions or the first and second kind. By plugging these solutions into **M** and **N**, $\mathbf{M}_{emn}$, $\mathbf{M}_{omn}$, $\mathbf{N}_{emn}$ and $\mathbf{N}_{omn}$ are obtained. The scattering fields can be expressed as linear combinations of these vector spherical harmonics. Due to orthogonality, only Legendre functions of the first order are nonzero.

The incident plane wave is expressed in spherical coordinates as

$$\mathbf{E}_i = \mathbf{E_0} \sum_{n=1}^{\infty} i^n \frac{2n+1}{n(n+1)} (\mathbf{M}_{o1n}^{(1)} - i\mathbf{N}_{e1n}^{(1)}) \qquad \mathbf{H}_i = \frac{-k}{\omega\mu} E_0 \sum_{n=1}^{\infty} i^n \frac{2n+1}{n(n+1)} (\mathbf{M}_{e1n}^{(1)} - i\mathbf{N}_{o1n}^{(1)})$$

After imposing particle boundary conditions and the orthogonality of the vector harmonics, an expression for the scattered fields is given as:

$$\mathbf{E}_s = \sum_{n=1}^{\infty} E_n (ia_n \mathbf{N}_{e1n}^{(3)} - b_n \mathbf{M}_{o1n}^{(3)}) \qquad \mathbf{H}_s = \frac{k}{\omega\mu} \sum_{n=1}^{\infty} E_n (ia_n \mathbf{N}_{o1n}^{(3)} - b_n \mathbf{M}_{e1n}^{(3)})$$

where

$$a_n = \frac{m\psi_n(mx)\psi_n'(x) - \psi_n(x)\psi_n'(mx)}{m\psi_n(mx)\xi_n'(x) - \xi_n(x)\psi_n'(mx)} \tag{4}$$

$$b_n = \frac{\psi_n(mx)\psi_n'(x) - m\psi_n(x)\psi_n'(mx)}{\psi_n(mx)\xi_n'(x) - m\xi_n(x)\psi_n'(mx)} \tag{5}$$

m is the relative refractive index ($m = n_p/n_m$), n_p is the complex refractive index of the nanoparticle material, n_m is the refractive index of the medium, $x=kr$ where r is the nanoparticle radius, and ψ_n and ξ_n are the Riccati-Bessel functions. The incident and scattered fields in each polarization state can be related by the amplitude scattering matrix as follows:

$$\begin{pmatrix} E_{//s} \\ E_{\perp s} \end{pmatrix} = \frac{e^{ik(r-z)}}{-ikr} \begin{pmatrix} S_2 & S_3 \\ S_4 & S_1 \end{pmatrix} \begin{pmatrix} E_{//i} \\ E_{\perp i} \end{pmatrix}$$

where the incident plane wave is traveling in the z-direction. Writing this equation in a different way, it is possible to relate the intensity and polarization of the incident and scattered waves.

$$\begin{pmatrix} I_s \\ Q_s \\ U_s \\ V_s \end{pmatrix} = \frac{1}{k^2 r^2} \begin{pmatrix} S_{11} & S_{12} & S_{13} & S_{14} \\ S_{21} & S_{22} & S_{23} & S_{24} \\ S_{31} & S_{32} & S_{33} & S_{34} \\ S_{41} & S_{42} & S_{43} & S_{44} \end{pmatrix} \begin{pmatrix} I_i \\ Q_i \\ U_i \\ V_i \end{pmatrix}$$

Where

$$I_s = \left\langle E_{//s} E_{//s}^* + E_{\perp s} E_{\perp s}^* \right\rangle,\ Q_s = \left\langle E_{//s} E_{//s}^* - E_{\perp s} E_{\perp s}^* \right\rangle,\ U_s = \left\langle E_{//s} E_{\perp s}^* + E_{\perp s} E_{//s}^* \right\rangle,\ V_s = i\left\langle E_{//s} E_{\perp s}^* - E_{\perp s} E_{//s}^* \right\rangle$$

The elements of the scattering matrix are known as the Stokes parameters. Our experiments are done with unpolarized light, for which the state vector is (1 0 0 0), so the Stokes parameter $S_{11} = \frac{I_s}{I_i} = \frac{1}{2}\left(|S_1|^2 + |S_2|^2\right)$ are of interest, where *I* is simply the irradiance. Differential cross sections are of interest since they are experimentally relevant: $\frac{d\sigma_{sc}}{d\Omega} = r^2 S_{11}$. The scattering parameters S_1 and S_2 incorporate the angular functions defined as $\pi_n = P_n^1/\sin\theta$ and $\tau_n = dP_n^1/d\theta$ where θ is the polar angle of the scattered light relative to the incoming wave vector,

$$S_1 = \sum_n \frac{2n+1}{n(n+1)}(a_n \tau_n + b_n \pi_n) \qquad S_2 = \sum_n \frac{2n+1}{n(n+1)}(a_n \pi_n + b_n \tau_n)$$

Using these expressions, the differential scattering cross section is:

$$\frac{d\sigma_{sc}}{d\Omega} = \frac{1}{2k_m^2}\left(\left|\sum_n \frac{2n+1}{n(n+1)}(a_n \pi_n + b_n \tau_n)\right|^2 + \left|\sum_n \frac{2n+1}{n(n+1)}(a_n \tau_n + b_n \pi_n)\right|^2\right) \qquad (6)$$

where k_m is the wavenumber of the light in the surrounding medium ($k_m = 2\pi n_m/\lambda$), a_n and b_n are given in (4) and (5), and λ is the vacuum wavelength. The sums over *n* are over all multipole excitations. The total scattering cross section is expressed as:

$$\sigma_{sc} = \frac{2\pi}{k^2}\sum_{n=1}^{\infty}(2n+1)\left(|a_n|^2 + |b_n|^2\right) \tag{7}$$

A MATLAB program was written to calculate the differential and total scattering cross sections of spherical particles of a chosen material in a defined dielectric medium (Appendix A). Polar plots of the angular scattered irradiance for a water droplet in air show the expected dipole for small particles (Figure 5) for light polarized parallel (red) and perpendicular (green) to the scattering plane. As particle size increases, however, a larger fraction of the total scattering is in the same direction as the incident light (forward scattering). With the incoming light is along 0º, the plots in Figure 6 show the angular scattering pattern for increasing water droplet size. The black plots (left) are taken directly from Bohren & Huffman and the colored plots (right) were made to verify the calculations. These plots illustrate the importance of accounting for the size and angle of the objective when comparing dark field measurements with calculations, i.e. it is not safe to assume that the same fraction of scattered light is being measured for different particles. Furthermore, the scattering patterns are most likely much more complex for nonspherical particles.

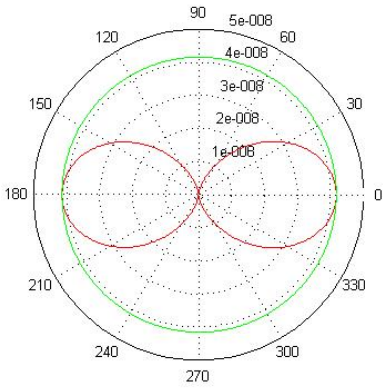

Figure 5 Dipolar scattering pattern for a spherical water droplet in the small particle limit for light polarized parallel (red) and perpendicular (green) to the scattering plane.

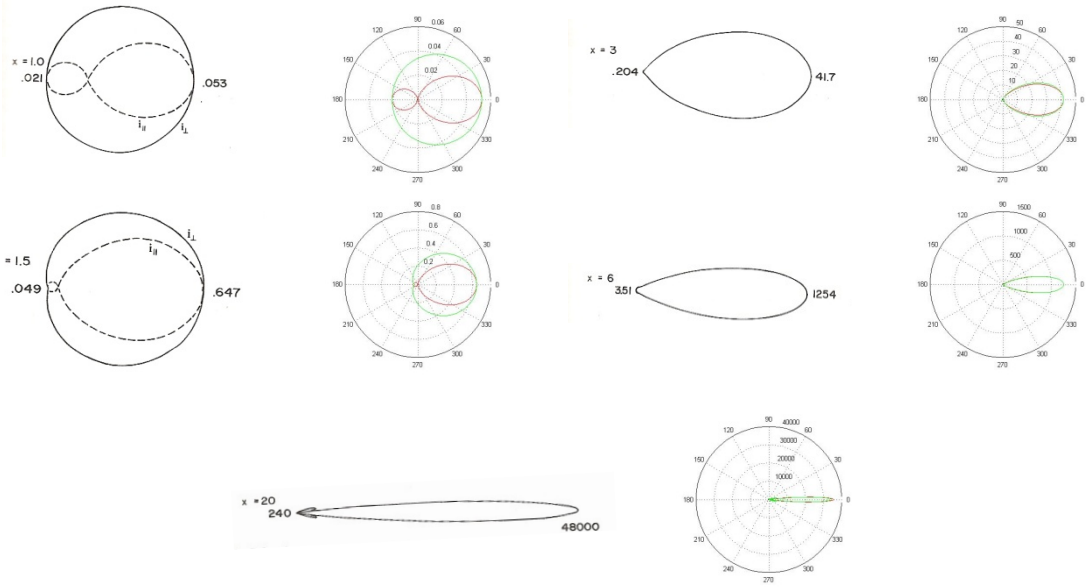

Figure 6 Angular scattering irradiance of a spherical water droplet where $x=2\pi n_p r/\lambda$. Forward scattering increases as the ratio of the particle size increases. Parallel (dashed and red lines) and perpendicular (solid and green lines) polarization of incident light.

2.2 Approximations and Extensions to the Mie Solution

The total cross section expressions from the Mie solution can be simplified by assuming particles that are much smaller than the wavelength of the incident light. Sometimes referred to as "the dipole approximation", the small particle approximation not only omits all but the $n = 1$ term in Equation 5 (dipole term), but also assumes that ($kr << 1$). In this case, only the first few terms in the power series expansions of the spherical Bessel functions are significant. The Mie solution for the total scattering cross section reduces to:

$$\sigma_{sc} = \frac{24\pi^3 V^2 \varepsilon_m^2}{\lambda^4}\left[\frac{(\varepsilon_1 - \varepsilon_m)^2 + \varepsilon_2^2}{(\varepsilon_1 + 2\varepsilon_m)^2 + \varepsilon_2^2}\right] \tag{8}$$

where V is the nanoparticle volume, ε_m is the dielectric function of the medium, and $\varepsilon_1 + i\varepsilon_2$ is the complex dielectric function of the nanoparticle. Note that complex refractive indices are often used to express the full Mie solution, but approximations for small particles are most succinctly written with the corresponding dielectric functions.

The Mie solution can be extended to spheroids in this small particle limit, yielding the following expression, known as the Gans Solution:

$$\sigma_{sc} = \frac{8\pi^3 V^2 \varepsilon_m^2}{9\lambda^4}\sum_j \frac{\frac{1}{P_j^2}\left[(\varepsilon_1 - \varepsilon_m)^2 + \varepsilon_2^2\right]}{\left(\varepsilon_1 + \frac{1 - P_j}{P_j}\varepsilon_m\right)^2 + \varepsilon_2^2} \tag{9}$$

where P_j are depolarization factors which depend on the nanoparticle aspect ratio.[68]

$$P_A = \frac{1-e^2}{e^2}\left[\frac{1}{2e}\ln\frac{1+e}{1-e} - 1\right] \qquad P_B = P_C = \frac{1-P_A}{2}$$

For prolate or elongated ellipsoids (A > B = C) where $e = \left(\frac{A^2 - B^2}{A^2}\right)^{1/2}$. To gauge the size range over which such approximations are accurate, Figure 7 displays the total scattering cross section calculated by Equation 5 (full Mie solution) and Equation 6 (small particle approximation) for 10, 60, and 100 nm diameter gold nanospheres. The MATLAB program in Appendix B was used for all calculations in this section. The small particle approximation is quite accurate for the 10 nm diameter nanosphere, it is blue-shifted but of similar magnitude for the 60 nm sphere, and it is completely inaccurate for the 100 nm sphere.

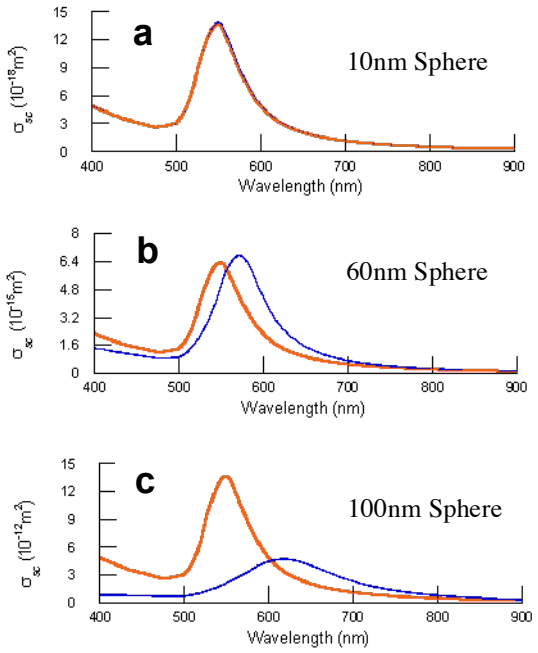

Figure 7 The total scattering cross sections for gold nanospheres of diameter 10nm, 60nm, and 100nm in oil calculated by the full Mie solution (blue) and the small particle approximation (orange).

It should be noted that referring to Equation 6 or a similar expression for the extinction as "the dipole approximation" is a bit of a misnomer. If the scattering cross section is calculated using only the dipole term (Equation 4, n=1), the calculations agree with the full Mie expression (summing over all multipole terms) for spheres larger than 100nm (Figure 8). It is the small particle approximation which simplifies the expression, and which makes the solution valid only for particles below 100 nm diameter.

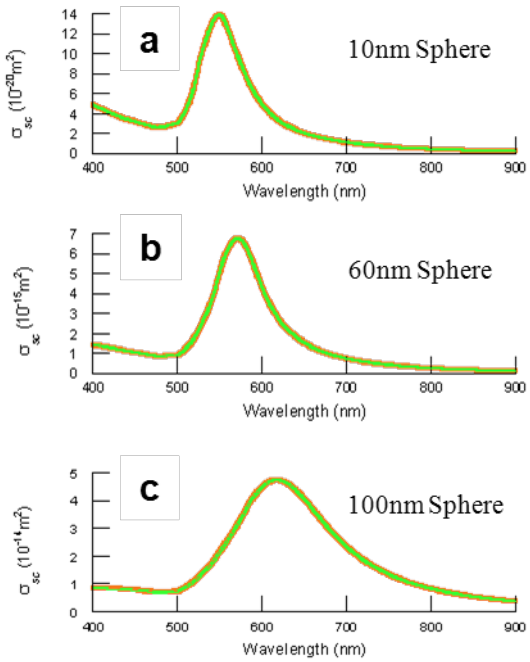

Figure 8 Scattering cross sections for gold nanospheres of diameter 10nm, 60nm, and 100nm in oil. The dipole term only (green) agrees well with the full Mie expression (red).

Full electromagnetic solutions for scattering from spheroids which could yield the differential scattering cross section for elongated nanoparticles have been derived,[69] but they have not yet been applied to nanoparticle plasmon resonances. Numerical simulations are certainly the most straightforward approach to predicting the brightness

of a specific nanoparticle of arbitrary shape. Several numerical methods have been employed to calculate the scattering properties of non-spherical particles, including Finite Element Method, Boundary Element Method, Finite Difference Time Domian, T-Matrix and Discrete Dipole Approximation, but they typically report the total cross section,[65-67, 70, 71] so they cannot be directly compared to the results presented here. Recently, numerical simulations have been reported which exactly match dark field measurements of nanoparticles on substrates.[72] If such simulations were designed to also report scattering cross sections, they could be quantitatively compared to the experimental observations described here.

As shown above, the Mie solution including angular dependence is the only analytical solution applicable to the problem of single particle scattering in the dark field geometry for particles in the 50-100nm range. Therefore, this solution can be used to calibrate dark field measurements with spheres to obtain the scaling constant between the scattering cross section at the angle of the objective and the CCD counts per second. After finding this constant for a specific microscope system, the constant can be used to find the scattering cross section at the angle of the objective of arbitrarily shaped particles.

2.3 Dark field Microscopy

The epi-illuminated dark field imaging geometry is illustrated in Figure 9. The illumination is directed to the sample from an annular ring around the objective lens. For an optically flat substrate, only light scattered from the nanoparticle enters the objective while the remainder of the light passes through the glass. If one assumes constant incident irradiance E_{inc}, to the nanoparticle, then the scattered radiant power that enters the objective, Φ_{sca}, will be proportional to the nanoparticle differential scattering cross section integrated over the solid area of the objective lens.

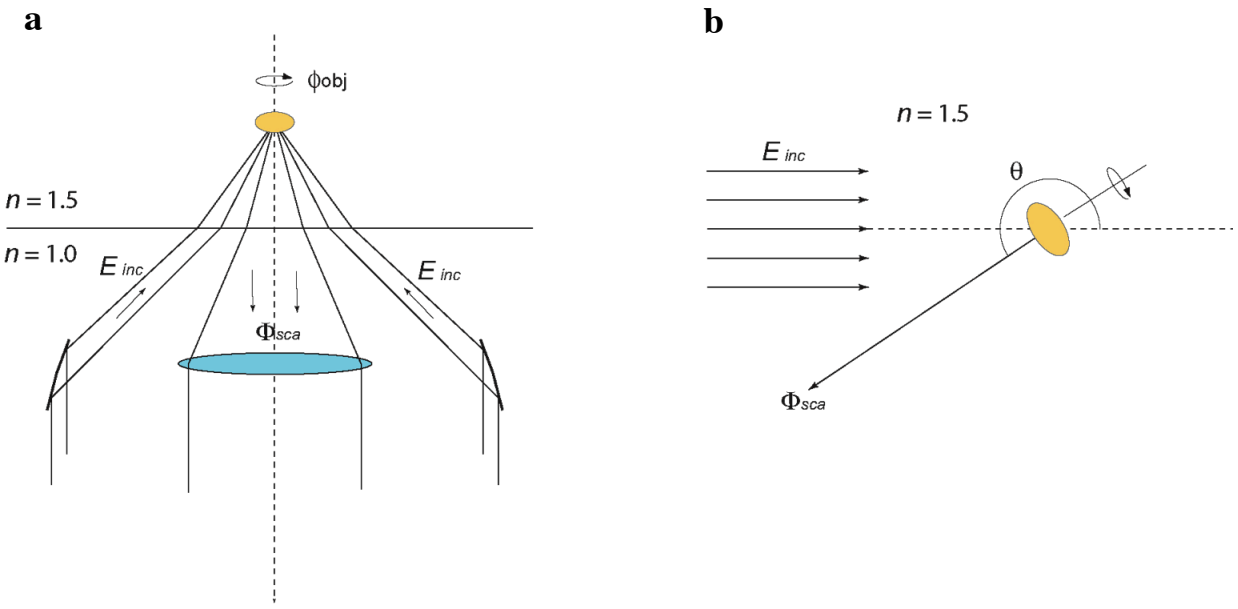

Figure 9 Schematics of the dark field imaging and scattering geometries.

This integrated value of the differential cross section will be referred to as σ_{obj}. When the scattered light reaches the CCD, it will generate a count rate that is proportional to Φ_{sca}, and therefore proportional to σ_{obj}. For the dark field microscope

objective used here (Zeiss LD Epi-plan 50x/0.5), the angle between the annular illumination and the optical axis of the objective lens is 45 degrees, and the numerical aperture of the objective indicates that light is collected into a 30 degree cone. The corresponding scattering diagram is shown in Figure 9b. If the optical axis is now taken to be along the incident illumination direction, one sees that the differential scattering cross section measured is backscattering approximately 225 degrees from the incident direction.

To achieve experimental conditions that match Mie scattering theory (see Figure 9a), nanoparticles were deposited onto glass substrates and covered with index matching oil and a cover slip so that the nanoparticles were in a homogenous dielectric medium rather than at a dielectric air-glass interface. The objective lens is not designed for oil immersion, but since it has a long working distance (6.7mm), it images well through the thin cover slip and oil layer (0.2 mm). The air-glass dielectric interface, although now separated from the nanoparticle, will affect the incidence and scattering angles. By approximating the imaging system with geometrical optics, the scattering angle θ was calculated to be 207 degrees. Since the illumination and light collection occur around the optical axis of the objective, the CCD signal is proportional to the azimuthally-averaged differential section around σ_{obj}, as illustrated in Figure 9b. For a nanoparticle with azimuthal symmetry (such as a nanosphere), this azimuthal dependence can be ignored.

2.4 Methods

2.4.1 Sample preparation

Gold nanospheres (Ted Pella) were deposited sparsely on a glass substrate. Figure 10a shows a schematic of the particles face-down (the dark field illumination and detection below the substrate). In order to correctly characterize each particle the location needed to be verified. An indexed TEM grid was placed on top of the particle side, then chrome and gold were evaporated onto the slide. After removal of the TEM grid, bare glass with particles is left in the previously covered areas (Figure 10b). Individual, isolated gold nanospheres were found and confirmed by correlated atomic force microscopy (AFM) and dark field imaging. Before measuring the single particle spectrum, index-matched oil was dropped on the slide, covered with a cover slip and sealed (Figure 10c).

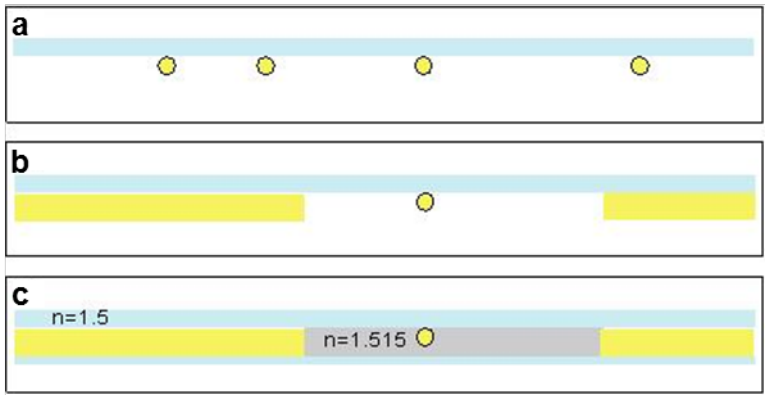

Figure 10 Schematic of reference grid evaporation process and oil immersion.

Following oil immersion, the spectrum of individual particles was measured with the dark field microspectrometer. Figure 11 shows the dark field image of a single

particle on glass within the indexed TEM grid. The particles were isolated in a horizontal slit, then the mirror reflecting light into the CCD was changed to a diffraction grating in order to measure the particle spectrum.

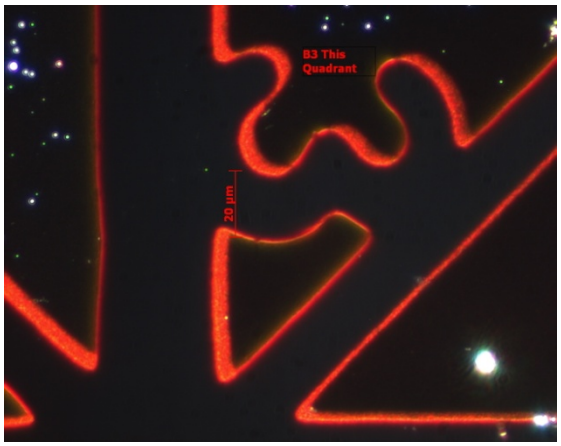

Figure 11 A dark field image of the particle substrate with the index grid. The green point is a single gold nanoparticle.

2.4.2 Data analysis

An example of a CCD image using the diffraction grating is shown in Figure 12. The bright line near the center of the image is the image of a single gold nanosphere isolated in a horizontal slit. The vertical axis is the wavelength of the scattered light, the horizontal axis is the position along the slit and the color intensity reveals the scattering intensity at that respective wavelength and position. The bright objects near the edges are due to the scattering of the alignment marks.

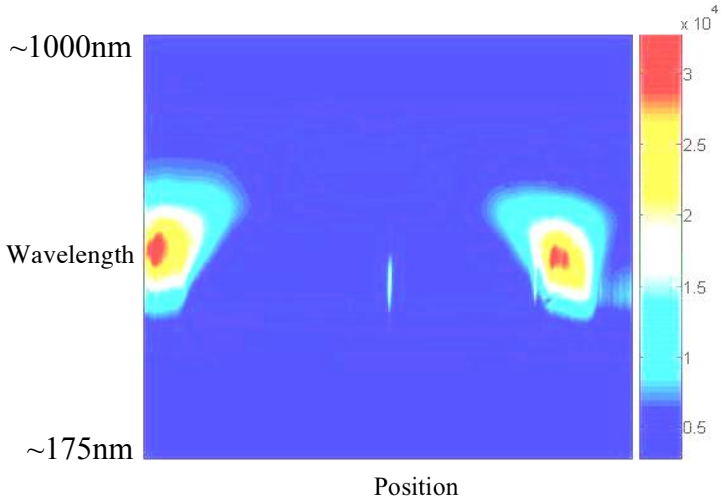

Figure 12 CCD image capturing a single nanoparticle spectrum.

These images were processed in MATLAB (Appendix C) in order to obtain a spectrum. Based on the image, the data analysis program asks the user to specify the particle position and width in pixels over which it sums the intensity. The background near the particle is fit to a polynomial of an order specified by the user and is subtracted from the particle signal. The result after the user enters the integration time of the image is the CCD counts per second as a function of the wavelength. Figure 13a displays the dark field spectral scattering rate for nanospheres that are 79 nm and 109 nm in diameter with the AFM images inset. For calibration, the differential scattering cross sections of the spheres were calculated from Mie scattering theory. The calculations included the first ten terms, and were integrated over the solid angle of the microscope objective to find σ_{obj}. The resulting cross sections are plotted in Figure 13b. The relative spectral magnitudes of the count rates and Mie calculations match quite well. Figure 13c displays the spectral "scattering constant" for the dark field microspectrometer, K_λ, found by dividing the count rate by σ_{obj} at each wavelength. Error bars, determined from the

experimental CCD counts in Figure 13a, are included. Since K_λ is simply a calibrated spectral efficiency of the dark field microspectrometer and independent of the sample, the 79 and 109 nm diameter nanoparticles yield similar curves (Figure 13c). K_λ can therefore be used to convert CCD count rates to cross sections for other nanoparticle shapes. Measurements on nanorods and bipyramids were analyzed with an average of the two curves presented in Figure 13c.

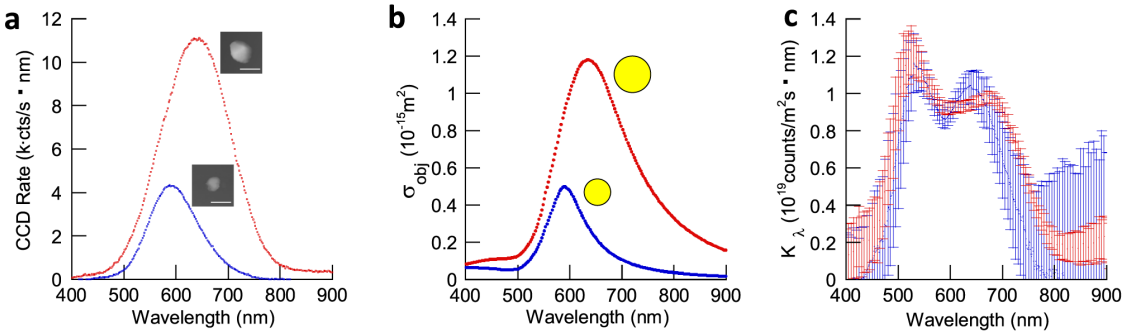

Figure 13 Calibration of the dark field scattering signal. a) The spectral CCD count rate from two nanospheres with inset AFM images (scale bar = 50 nm). b) The calculated differential cross sections of the same nanospheres integrated over the solid angle of the objective. c) The resulting spectral scattering constant.

2.5 Application to other particles

2.5.1 Gold bipyramid

Gold bipyramids have the shape of two elongated pentagonal pyramids connected at their bases. Bipyramids are synthesized by surfactant-directed growth (as are gold nanorods), but are much more monodisperse and generally larger in size.[26] An individual 135 x 53 nm bipyramid was located relative to alignment marks and characterized by environmental scanning electron microscopy (FEI Quanta 400 ESEM). The bipyramid was then immersed in oil, located in the dark field microspectrometer and its spectral count rate recorded. The spectral scattering constant was applied to convert the data to the σ_{obj} presented in Figure 14. As mentioned above, σ_{obj} represents the azimuthal average of the bipyramid differential cross section integrated over the objective lens's solid angle. The peak scattering cross section to the objective is 1.2×10^{-16} m^2, and the narrow spectral width is consistent with previous reports of single bipyramid spectra.[26]

In addition to the cross section, Figure 14 displays σ_{obj} for a sphere of the equivalent volume calculated from the full Mie solution as in Figure 13. Under the imaging conditions reported here, the bipyramid is approximately two times brighter than its equivalent sphere.

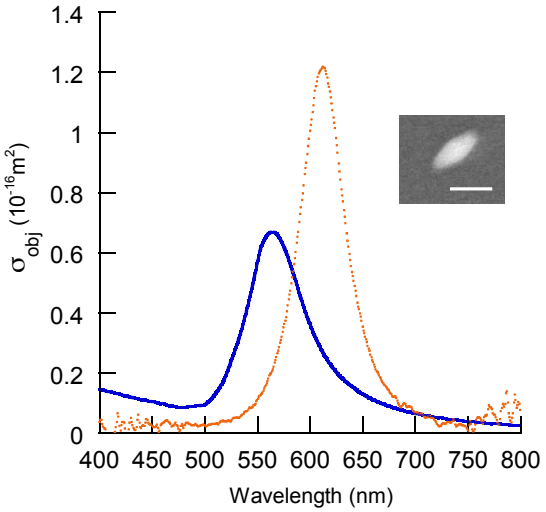

Figure 14 The measured gold bipyramid scattering cross section (red) and the calculated cross section for a gold sphere of equivalent volume (green). The inset shows an ESEM image of the bipyramid on glass (scale bar is 100 nm).

2.5.2 Gold nanorod

In an attempt to measure single nanorod scattering, it has been found that individual nanorods (up to 50 x 15nm) do not scatter sufficiently to be detected by dark field microscopy at NA=0.5 with a halogen lamp illumination.[73] Figure 15a shows an AFM image a region near alignment marks that are also visible in the optical images (c and d). A zoomed AFM image (b) reveals a large nanosphere in the upper right (triangular shape is a tip artifact) and a nanorod in the lower left. The nanorod is clearly revealed in the inset. Its size is exaggerated by the tip. Two detectors, a high sensitivity CCD (c) and a color CCD (d) were used, yet the individual particle does not scatter a

detectable amount of light. These small, dim particles, however, can be imaged by more sensitive methods such as confocal reflectance microscopy.[70, 74, 75]

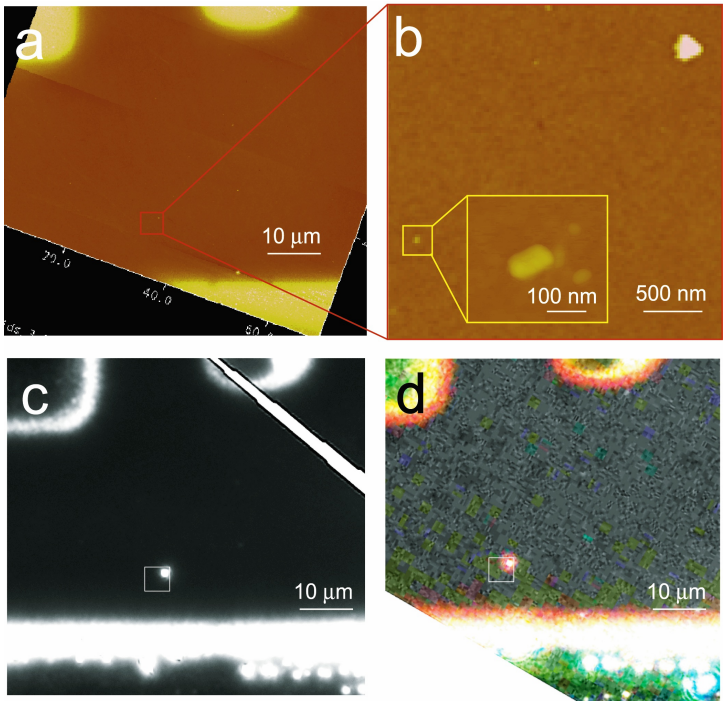

Figure 15 Individual gold nanorod ~50 x 15nm. AFM (a&b), and optical dark field (c&d).

In order to measure the differential scattering cross section of a single nanorod by dark field microscpectroscopy, an isolated patch of nanorods was created by scratching a nanorod film. The one micron square patch contained 28 isolated nanorods with an average size of 40 x 13nm, as determined by AFM. The dark field scattering rate was analyzed as above and divided by the number of nanorods in the patch to obtain the average cross section of a single nanorod (Figure 16). The nanorod, being much smaller, is 100 times less bright than the bipyramid in the dark field microscope. The peak is broadened due to the presence of various shapes of nanorods in the patch, which were

found to have lengths ranging from 33 to 57 nm and diameters ranging from 10 to 15 nm. The noise in the measurement is a result of being at the lower detection limit.

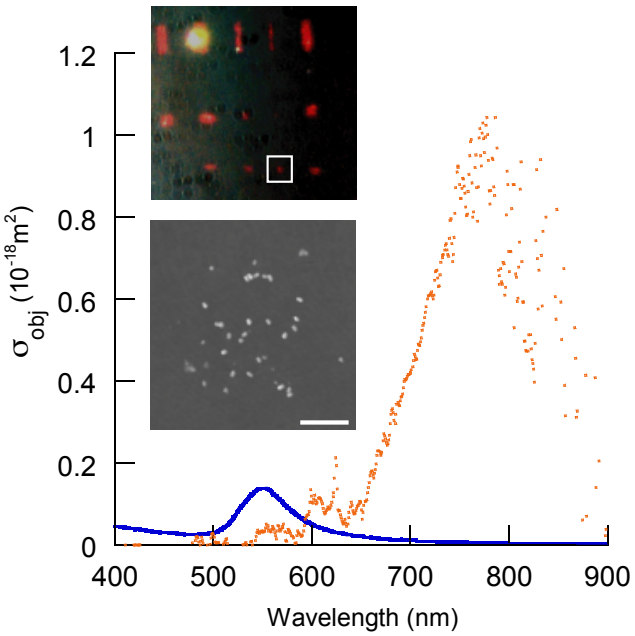

Figure 16 The average scattering cross section for a single nanorod (orange) measured from a patch of 28 nanorods shown in dark field microscopy (top inset) and AFM (bottom inset, scale bar = 500 nm). The calculated equivalent gold sphere cross section is also plotted (blue).

For an ellipse of this size, the single particle approximations that are included in the Gans expression is correct to within 10%. Figure 17 shows the Gans solution total scattering cross section averaged over all illumination angles and nanorod sizes from the patch in Figure 16. After fitting the average Gans solution to a Gaussian distribution, the ratio between the scattering peak of the elongated particle and the spherical particle is found to be approximately equal to the value measured for σ_{obj} (~7.5). Therefore, for particles of this size, the total scattering cross section is an accurate predictor of the relative contrast in dark field microscopy. For larger particles of complex shapes,

however, it is likely that this relationship does not hold. Small particles tend to scatter in a dipole pattern, regardless of their shape. As particle size increases the angular scattering becomes less of a dipole pattern and exhibits more forward scattering. Particle shape will change this far-field scattering pattern in a way that cannot be described with simple analytical expressions.

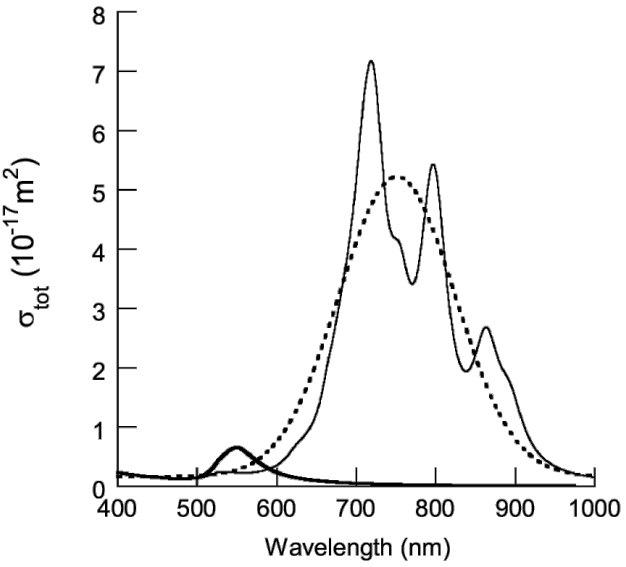

Figure 17 The average total scattering cross section calculated with the Gans Solution for the various sizes of nanorods in the spectrum measured in Figure 16 (fine line) with a Gaussian fit to that curve (dashed line) along with the total scattering cross section for a sphere of the equivalent average volume (bold line).

2.6 Discussion

These measurements show that elongated plasmon resonant nanoparticles scatter more brightly than their equivalent volume spheres. This is due to the reduced plasmon damping in gold at the near-infrared wavelengths of their peak plasmon resonance.[19] However, many other factors may affect the observed scattering signal, such as the increased wavelength, polarization dependence, and angular pattern of the scattered light. The Gans solution is only applicable to very small particles, therefore, in addition to the shape mismatch, it is of no use in predicting bipyramid scattering.

These results are in good agreement with the report by Schultz *et al.* [63] The 109 nm sphere in Figure 13a, integrated over detectable wavelengths, generates approximately 10^6 counts per second from the CCD, which correlates well to the photon flux reported by Schultz *et al* given that the measurements reported here are on a larger nanoparticle made of gold (as opposed to silver which supports stronger plasmon resonances), and using a lower NA objective. Even bright fluorophores with extinction coefficients as high as 100,000 $M^{-1}cm^{-1}$ and high quantum efficiencies have emission cross sections on the order of 10^{-22} m^2. These results establish a baseline cross section detectivity of approximately 10^{-18} m^2 for single nanoparticle scattering in the dark field setup described here, but that is certainly not a lower limit. Transmitted illumination dark field microscopy with both oil immersion condenser and objective generally provides more signal (due to the higher NA) and a darker background. Also, this geometry will capture scattering in the forward hemisphere, which is predominant for larger nanoparticles. However, this imaging mode may prove more difficult to calibrate since the illumination is manually aligned.

2.7 Conclusion

The spectral scattering for a NA=0.5 dark field microspectrometer was calibrated using measurements on gold nanospheres and the corresponding full Mie theory solution. The calibration was applied to gold nanorods and bipyramids to quantitatively characterize their spectral scattering properties. These results show that elongated particles scatter strongly for their volume and are ideal for many applications that require small, bright nanoparticles. The brightness of small, elongated nanoparticles can be accurately predicted by simple small-particle formulas for the total scattering cross section. Larger particles, however, would be best treated with numerical calculations.

3 Gold Nanobelts

This section will discuss the optical properties of gold nanowires with rectangular cross sections, referred to as gold nanobelts.[76] This structure combines the tunability and sharp resonances of sub-wavelength sized nanoparticles with the extended structure of nanowires.

3.1 Methods

3.1.1 Gold Nanobelt Synthesis

In a typical synthesis, aqueous CTAB (cetyltrimethylammonium chloride, 50 mM, 650 μL) and SDS (sodium dodecylsulfate, 10 mM, 500 μL) were added to 3.45mL of DI water at room temperature. After allowing the surfactants to mix for several minutes, $HAuCl_4$ (10mM, 100 μL) was added. The solution was then thermostated for 30 minutes at 27°C. Finally, freshly prepared L-ascorbic acid (100 mM, 300 μL) was added and the solution was allowed to sit at 27°C for 12 hours. During the growth reaction, the solution gradually became turbid and exhibited a reddish hue (Figure 18a). The color is typical of plasmon resonant gold nanoparticle solutions, and the turbidity was due in part to the formation of micron-scale surfactant crystals that are visible in an optical microscope. The spectral extinction exhibits a weak band at 520 nm (Figure 18b), which is also consistent with the presence of gold nanoparticles. Small aliquots of as-prepared nanobelt solutions were deposited onto glass substrates and, allowed to dry, and then rinsed with methanol to remove the excess surfactant. For correlated measurements between the optical microscope and AFM/SEM/TEM, gold was evaporated over a TEM

grid and the pattern was used as a map to find the same particle in different instruments, as described on p.21.

3.1.2 Gold Nanobelt Geometric Characterization

Figure 18 displays electron micrographs that illustrate the flat, elongated geometry of the structures. The gold nanobelts described here have sub-100 nm cross-sectional dimensions and lengths greater than 10 μm. The high-resolution image and diffraction pattern are consistent with the previous report, which concluded that the nanobelt structure is single-crystalline gold that grows along the <211> direction and has a [111] plane on the top flat surface.

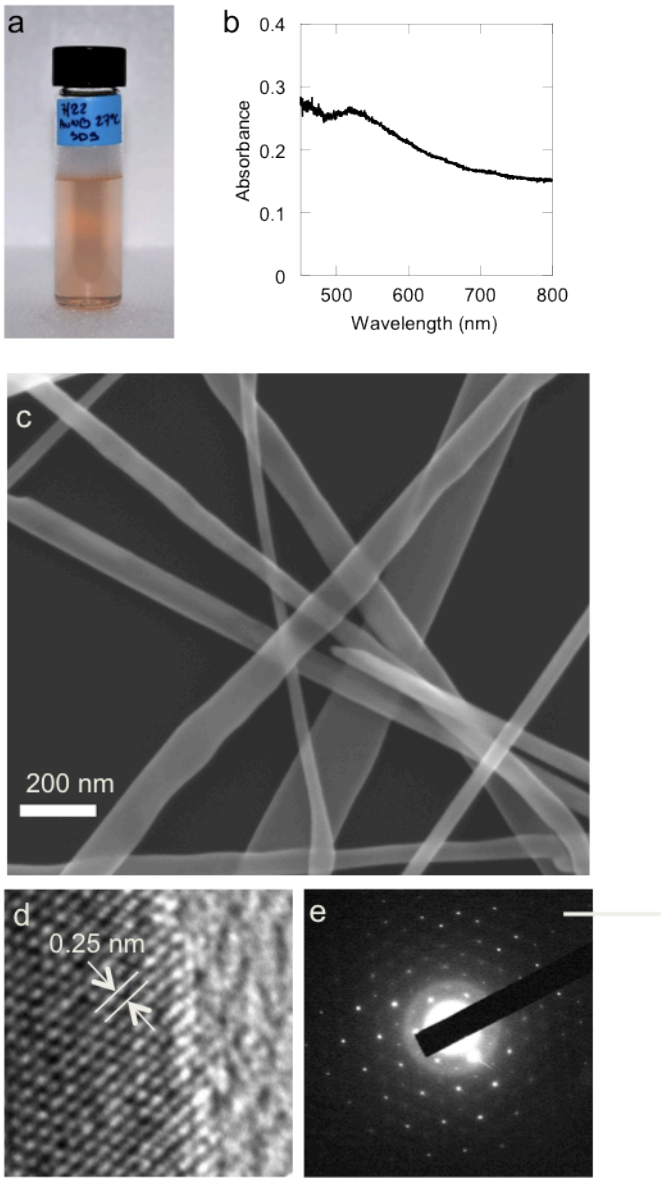

Figure 18 Gold nanobelts. The suspensions have (a) a pinkish turbid appearance, and (b) a weak plasmon resonant spectral absorption peak at 520 nm. Electron micrographs illustrate (c) the overall ribbon-like morphology and (d) high resolution crystalline structure. (e) Electron diffraction confirms the single-crystalline gold structure.

Well-isolated belts that were near reference marks were chosen for spectral analysis. The same nanobelts were imaged by tapping mode AFM under ambient conditions with a Nanoscope IV Multimode AFM (Veeco). An image of the 100 x 20 nm

nanobelt from Figure 21 is in Figure 19. Note that the large structure at the top of the image corresponds to the yellow scattering at the end of the red nanobelt in Figure 21. The nanobelt heights and widths were taken from section analysis of the images. Figure 20 shows the analysis of the 100 x 20 nm nanobelt from Figure 21 and Figure 19. The height measurement is straightforward. For the width, a flat top surface is assumed, and the curved edges are considered tip broadening and ignored.

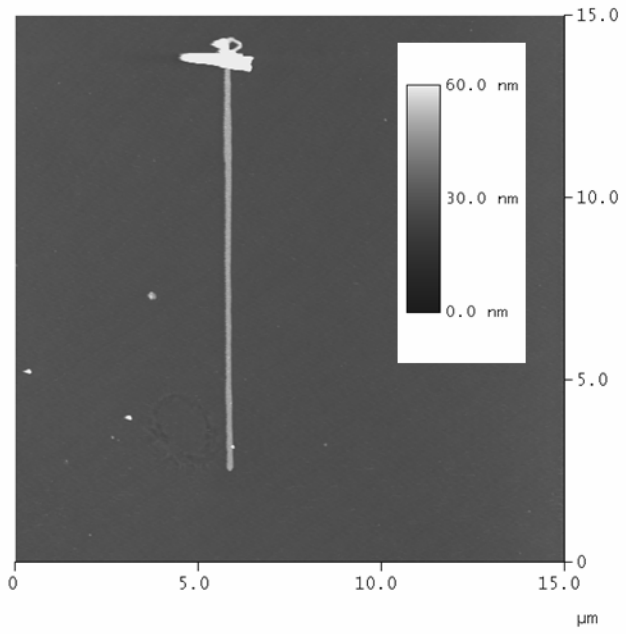

Figure 19 A tapping mode AFM image of the 100 x 20 nm gold nanobelt from Figure 21,

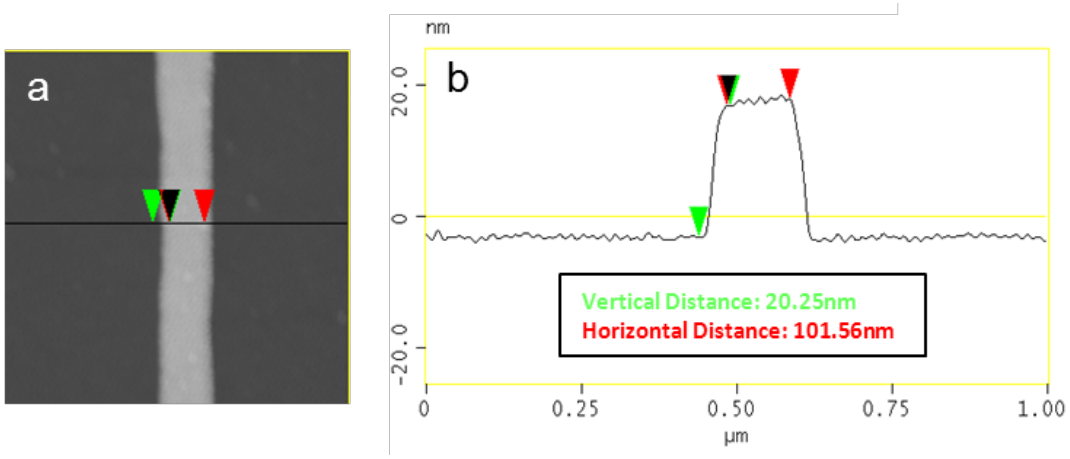

Figure 20 Section analysis of the AFM image in Figure 19. The red markers yield a width of 100 nm, and the green markers yield a heigh of 20 nm.

Here the cross-sectional aspect ratio, x-AR, is defined as the nanobelt width divided by the height. Since these nanobelts are very long, the length to width aspect ratio that has been addressed in previous studies is not considered.[71, 77]

3.2 Dark Field Scattering Spectra: Transverse Plasmon Modes

Dark field measurements, as described in Section 1.2, were performed on gold nanobelts. As seen in the dark field images (50X/0.5 NA objective, Zeiss Axiovert 200M), the existence of a tunable plasmon resonance is apparent, as nanobelts with low cross-sectional aspect ratio appear green and those with higher aspect ratio appear red. The nanobelt scattering spectra were recorded from the center of each belt by an imaging spectrograph and CCD camera. White light was incident through the annular dark field objective and was unpolarized. A polarizer behind the objective analyzed the scattered light and scattering images were recorded for polarizations parallel and perpendicular to the nanobelt length. As seen in Figure 21, the measurements reveal a plasmon mode polarized perpendicular to the nanobelt length which redshifts with increasing cross-sectional aspect ratio. Also shown are scattering spectra polarized parallel to the nanobelts, which were relatively featureless. The perpendicular spectra were plotted versus energy and fitted to find their line widths (Γ), which are also given in Table 1.

x-AR	Width (nm)	Height (nm)	Γ (meV)
1.0	25	25	268
1.4	50	35	303
2.1	55	26	308
3.3	100	30	510
5.0	100	20	358
5.9	100	17	261

Table 1 The nanobelt sizes and spectral line width from the data in Figure 21.

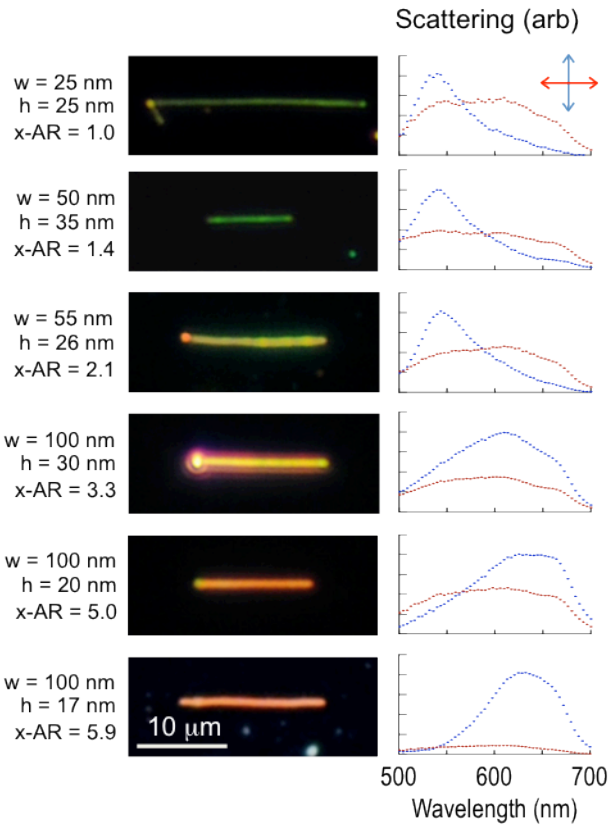

Figure 21 Dark field micrographs (left) and corresponding single nanobelt spectra (right). The blue spectra are polarized transverse to the nanobelt, and the red spectra are polarized parallel to the nanobelt.

Note that the measured spectra of the high cross-sectional aspect ratio nanobelts in Figure 21 appear to have some structure as though they are made up of multiple peaks. While such peaks can be attributed to substrate interactions,[24] here they are artifacts of the data analysis. Different choices of the background subtraction parameters cause somewhat different spectral shapes, although they do not affect the overall tunability. In addition, the measured linewidths given in Table 1 are similar to the homogeneous linewidths of single gold nanoparticles.[19]

3.2.1 Numerical Simulations

To understand the nature of the observed nanobelt plasmon resonance, finite-difference time-domain (FDTD) calculations were carried out for the nanobelt geometry using a measured dielectric function for gold.[78] The simulation geometry, shown schematically in Figure 22a, was designed to match the experimental dark field spectroscopy measurements. Illumination was incident at 45 degrees to the nanobelt long axis (as in the experiment) and the total scattering cross section for an infinitely long nanobelt was calculated. The infinite nanobelt was simulated by extending it through perfectly matched layer boundary conditions that minimize reflections.[79] With the incident *k*-vector along the nanobelt length and TE polarization across the nanobelt as shown in Figure 22a, a scattering resonance was found (Figure 22b) that shifts with aspect ratio in a manner similar to the experimental measurement. Analysis of the charge and field distributions showed that the bright scattering resonance is a plasmon mode with antisymmetric charge alignment across the nanobelt width as depicted by the charge distribution plot in Figure 22c. Note that the simulation results in Figure 22 do not include the substrate. A scattering spectrum was simulated by the finite element method (FEM) method for a gold nanobelt with cross-sectional aspect ratio of 3.3 both with and without a glass substrate. As seen in

Figure 23, the substrate caused an 18 nm red shift, but otherwise had no significant impact on the spectrum.

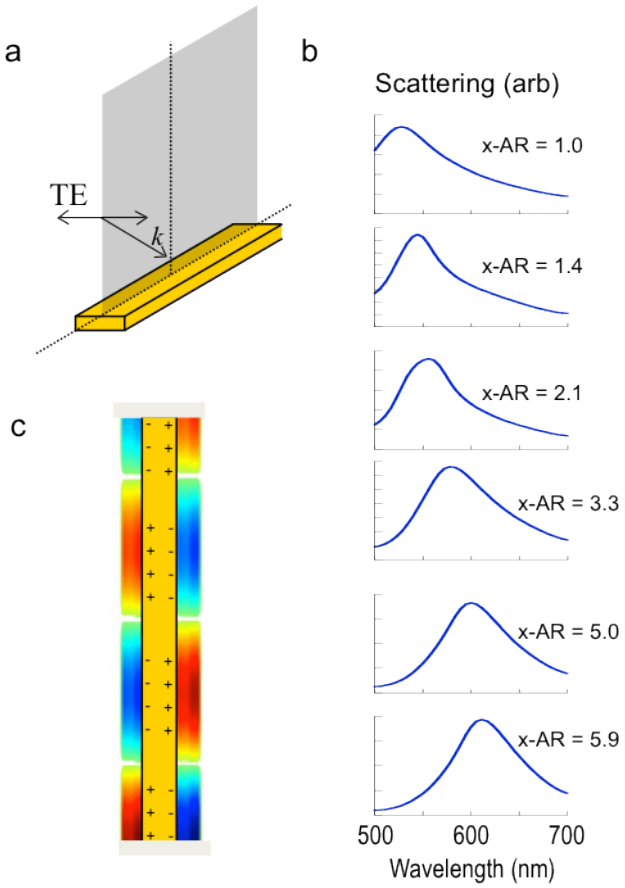

Figure 22 (a) Gold nanobelt simulation geometry and (b) resulting spectra for cross-sectional aspect ratios that match Figure 21 (c) The calculated charge distribution of the scattering mode.

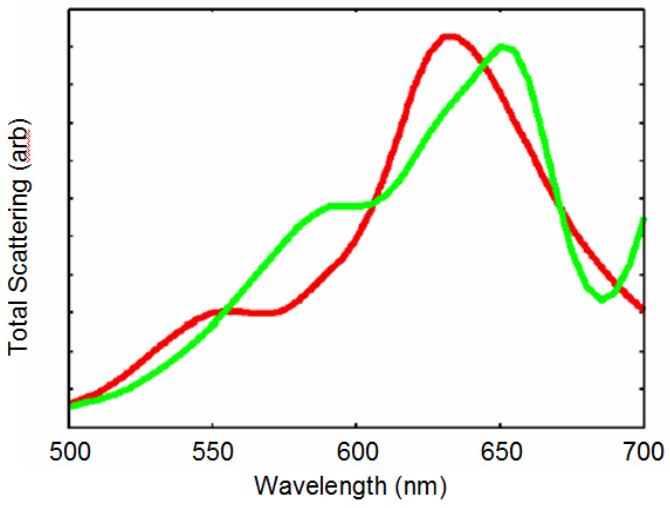

Figure 23 The total scattering cross section calculated by FEM for a gold nanobelt with (green) and without (red) a glass substrate.

To more closely match the experimental measurement, FDTD simulations were also carried out for a finite nanobelt and the differential scattering cross section was calculated. Due to computational complexity, these simulations were performed on a nanobelt of only 0.4 micron length, which resulted in strong Fabry-Perot resonances that do not occur in this experiment because the nanobelt lengths are greater than 10 microns. The experimental data is therefore compared to the total cross sections calculated for infinite nanobelts.

Other plasmon modes were found in the simulations that were not evident in the experiments. For instance, for TM polarization, the calculations revealed an antisymmetric mode, with its dipole moment oriented in a zig-zag pattern along the nanobelt length (Figure 24). This peculiar orientation of the dipole moment is due to an admixture of symmetric and antisymmetric plasmon modes on the upper and lower surfaces of the nanobelt.[80] The zig-zag mode was found to predominantly scatter in a direction outside the numerical aperture of the microscope objective, so it was not observed.

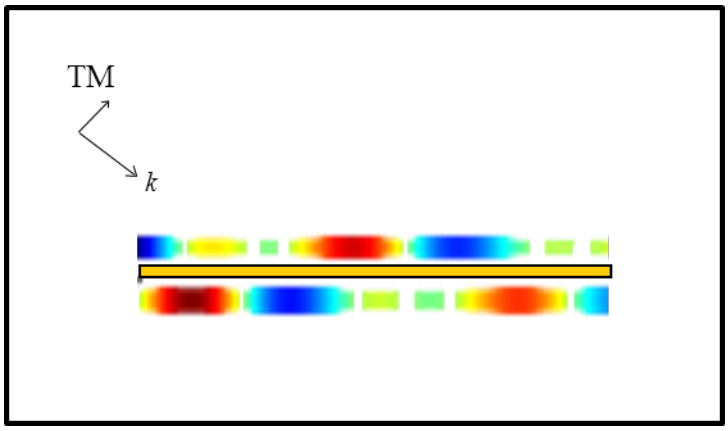

Figure 24 The calculated charge distribution of the zig-zag mode at 624 nm excited by incident TM illumination.

3.2.2 Discussion

Spectral scattering peaks for both the experiments and simulations were fitted to analyze the tunability of the transverse plasmon resonance in the nanobelt structure. The results, plotted in Figure 25, agree well and reveal an approximately linear relationship between the cross-sectional aspect ratio and resonance wavelength, which is very similar to the behavior for elongated nanoparticles such as gold nanorods.[64] Interestingly, the nanobelt structure has a lower sensitivity to the cross-sectional aspect ratio, shifting only 100 nm (~525 nm to ~625 nm) with cross-sectional aspect ratio increasing from 1 to 5. In contrast, gold nanorods (with their aspect ratio defined as the ratio of the length and width) shift over a similar spectral range with an aspect ratio change of only 1 to 2.5.[81] An additional increase in the nanobelt cross-sectional aspect ratio through synthesis may enable the plasmon resonance to be further tuned to the near infrared.

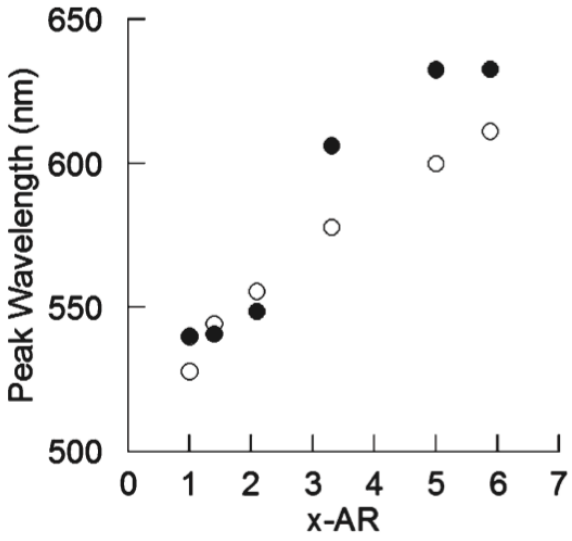

Figure 25 The dependence of the plasmon resonance peak on cross-sectional aspect ratio in the experiments (solid circles) and simulations (hollow circles).

3.2.1 Mie Scattering for an Infinite Cylinder

Although strong transverse resonances have not been previously reported in plasmonic nanostructures, the problem of light scattering from an infinite cylinder can be solved analytically. By solving Maxwell's Equations in a cylindrically symmetric system, as outlined by Bohren and Huffman[58] (p.194) and summarized here, it is possible to obtain the scattering cross section for an arbitrary size of cylindrical nanowire. For small sizes, a strong transverse plasmon mode is predicted for cylinders. This resonance, however, is not strongly tunable and quickly broadens with increasing cylinder radius.

In this case, the Mie scattering coefficients a_n and b_n for an infinite cylinder consist of parallel and perpendicular components. In an infinite cylinder with normally incident light, the plasmonic response is separated into components along both parallel and perpendicular axes.

As in the problem of absorption scattering by a sphere, the starting point is the vector wave equation $\nabla^2\psi + k^2\psi = 0$. Written in cylindrical polar coordinates, this equation becomes

$$\frac{1}{r}\frac{\partial}{\partial r}\left(r\frac{\partial\psi}{\partial r}\right) + \frac{1}{r^2}\left(\frac{\partial^2\psi}{\partial\phi^2}\right) + \frac{\partial^2\psi}{\partial z^2} + k^2\psi = 0$$

Solutions to this equation that are single-valued functions of ϕ are of the form

$$\psi_n(r,\phi,z) = Z_n(\rho)e^{in\phi}e^{ihz} \qquad (n = 0, \pm 1, \dots)$$

where $\rho = r\sqrt{k^2 - h^2}$ and Z_n is a solution to the Bessel equation

$$\rho\frac{d}{d\rho}\left(\rho\frac{d}{d\rho}Z_n\right) + (\rho^2 - n^2)Z_n = 0$$

The linearly independent solutions to this equation are Bessel functions of the first and second kind. In general, the separation constant h is unrestricted. The vector cylindrical harmonics generated are

$$\mathbf{M}_n = \nabla\times(\hat{\boldsymbol{e}}_z\psi_n), \qquad \mathbf{N}_n = \frac{\nabla\times\mathrm{M}_n}{k}$$

where the pilot vector is the unit vector $\hat{\boldsymbol{e}}_z$, parallel to the cylinder axis.

In component form

$$\mathbf{M}_n = \sqrt{k^2 - h^2}\left(in\frac{Z_n(\rho)}{\rho}\hat{\boldsymbol{e}}_r - Z_n'(\rho)\hat{\boldsymbol{e}}_\phi\right)e^{i(n\phi+hz)}$$

$$\mathbf{N}_n = \frac{\sqrt{k^2 - h^2}}{k}\left(ihZ_n'(\rho)\hat{\boldsymbol{e}}_r - hn\frac{Z_n(\rho)}{\rho}\hat{\boldsymbol{e}}_\phi + \sqrt{k^2 - h^2}Z_n(\rho)\hat{\boldsymbol{e}}_z\right)e^{i(n\phi+hz)}$$

where **M** and **N** are orthogonal. Similarly to Section 2.1.1 where the incident wave was expanded in vector spherical harmonics to solve for scattering from a sphere, both the incident electric field parallel (along the cylinder axis) and perpendicular (transverse to cylinder axis) to the xz plane and the incident electric field must be expanded in vector cylindrical harmonics. Starting with the field parallel to the cylinder axis:

$$\mathbf{E}_i = \sum_{n=-\infty}^{\infty} E_n \mathbf{N}_n^{(1)} \;\; ; \;\; \mathbf{H}_i = \frac{-ik}{\omega\mu} \sum_{n=-\infty}^{\infty} E_n \mathbf{M}_n^{(1)}$$

At large distances from the cylinder axis, the first and second order generating functions tend to zero, and the scattered far-fields are given as:

$$\mathbf{E}_\mathrm{s} = -\sum_{n=-\infty}^{\infty} E_n \left[b_{n\mathrm{I}} \mathbf{N}_n^{(3)} + i a_{n\mathrm{I}} \mathbf{M}_n^{(3)} \right] ; \; \mathbf{H}_s = \frac{ik}{\omega\mu} \sum_{n=-\infty}^{\infty} \left[b_{n\mathrm{I}} \mathbf{M}_n^{(3)} + i a_{n\mathrm{I}} \mathbf{N}_n^{(3)} \right]$$

When the incident light is normal to the cylinder axis, it follows from the relations $J_{-n} = (-1)^n Y_n$ that

$$a_{-n\mathrm{I}} = -a_{n\mathrm{I}}, \qquad b_{-n\mathrm{I}} = b_{n\mathrm{I}}, \qquad a_{0\mathrm{I}} = 0.$$

In this configuration$(\zeta = 90°)$, $a_{n\mathrm{I}}$ vanishes and

$$b_{n\mathrm{I}}(\zeta = 90°) = b_n = \frac{J_n(mx) J_n'(x) - m J_n'(mx) J_n(x)}{J_n(mx) H_n^{(1)\prime}(x) - m J_n'(mx) H_n^{(1)}(x)}$$

Similarly, for incident light perpendicular to the xz plane:

$$\mathbf{E}_i = -i \sum_{n=-\infty}^{\infty} E_n \mathbf{M}_n^{(1)}$$

the curl of which gives the incident magnetic field.

$$\mathbf{E}_\mathrm{s} = \sum_{n=-\infty}^{\infty} E_n \left[b_{n\mathrm{II}} \mathbf{N}_n^{(3)} + i a_{n\mathrm{II}} \mathbf{M}_n^{(3)} \right]$$

It follows that $b_{n\mathrm{II}}$ vanishes and

$$a_{n\mathrm{II}}(\zeta = 90°) = a_n = \frac{mJ_n'(x)J_n(mx) - J_n(x)J_n'(mx)}{mJ_n(mx)H_n^{(1)\prime}(x) - J_n'(mx)H_n^{(1)}(x)}$$

The incident and scattered fields of each polarization can be related through a scattering matrix (Bohren & Huffman p.202). From there, the Poynting vector and the total energy scattered can be obtained, leading to the scattered light per unit length of the cylinder:

$$Q_{sca,\mathrm{I}} = \frac{2}{x}\left[|b_{0\mathrm{I}}|^2 + 2\sum_{n=1}^{\infty}(|b_{n\mathrm{I}}|^2 + |a_{n\mathrm{I}}|^2)\right] \tag{10}$$

$$Q_{sca,\mathrm{II}} = \frac{2}{x}\left[|a_{0\mathrm{II}}|^2 + 2\sum_{n=1}^{\infty}(|a_{n\mathrm{II}}|^2 + |b_{n\mathrm{II}}|^2)\right] \tag{11}$$

Forms of these equations that are optimized for computation are outlined in Appendix C of Bohren and Huffman[58]. Matlab program was written to solve for the scattering and extinction of an infinite cylinder (Appendix E: Mie Scattering from an Infinite Cylinder). Figure 26 shows the plasmonic response of a 10nm diameter infinite cylinder both transverse to, and along the axis of the cylinder. Due to the small radial size, the transverse resonance is narrow, as in the case of the nanobelts. The peak due to the longitudinal oscillations of electrons, however, is not a resonance (a standing wave or mode), but is the result of interband transitions in gold. Note that the magnitude of the longitudinal plasmon response is much smaller than that of the transverse response.

Figure 27 shows the scattering cross section transverse to the cylinder axis for a range of cylinder radii. The plasmonic response perpendicular to the cylinder length exhibits a strong, narrow resonance for small sizes, but with increasing size, does not exhibit a substantial peak shift and quickly broadens in linewidth.

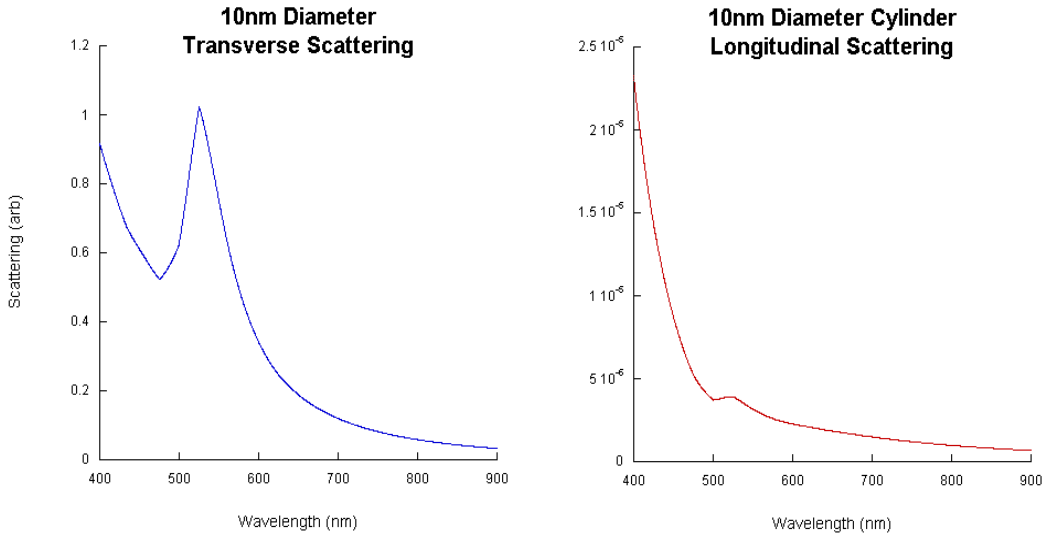

Figure 26 Light scattering from an infinitely long, 10nm diameter cylinder transverse (left) and along the cylinder axis (right). Notice the difference in magnitude.

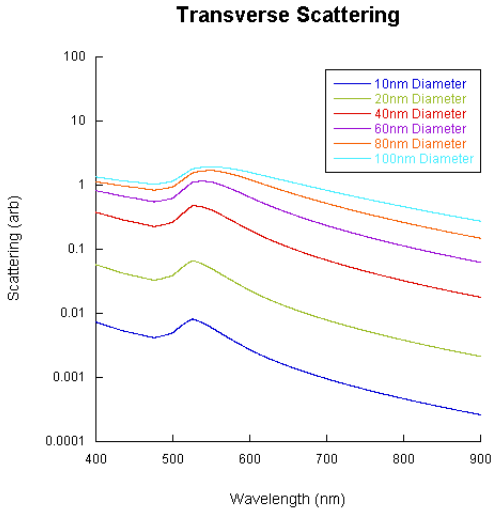

Figure 27 Scattering for infinite cylinders with a range of radii (logarithmic scale).

As seen in Figure 28, the transverse plasmon resonance peak of a small cylinder is similar in linewidth to the rectangular cross sectioned gold nanobelt (<115nm, as calculated and shown in Figure 22), but as cylinder radius grows, the peak quickly broadens. This is why most chemically synthesized nanowires appear white in dark field microscopy.

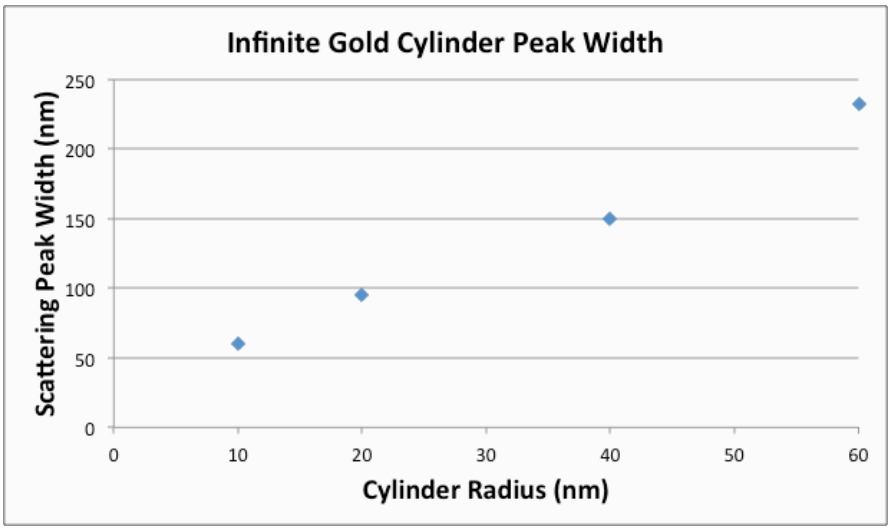

Figure 28 Calculated peak widths of infinite gold cylinders.

3.2.2 Conclusion

The results presented in this section describe a simple synthetic route towards an extended structure that exhibits sharp plasmon resonances for antisymmetric excitation across the nanobelt width. This transverse resonance is shown to be very narrow and tunable when compared to conventional cylindrical nanowires. These structures may find applications as sub-wavelength plasmonic bandpass filters, only allowing light of specific wavelengths determined by the cross-sectional geometry to be transmitted. Furthermore, gold nanobelts may be considered for biological applications that currently employ tunable nanoparticles. The larger size of the nanobelts will provide a larger scattering cross section for imaging contrast or detection, and nanobelts may offer unique interactions with cells and tissues due to their size and shape.

3.3 Tapered Gold Nanobelts

3.3.1 Characterization

The nanobelt synthesis outlined in section 3.1.1 has various products beyond the uniform nanobelts discussed in the last section. Based on an analysis of many nanobelt images like Figure 29, approximately 10% of the gold nanobelts are uniform and the rest show significant variations in color along their length. While most vary with no discernible pattern, about 10% of the nanobelts exhibit a uniform transition from green to red due to a smooth change in aspect ratio.

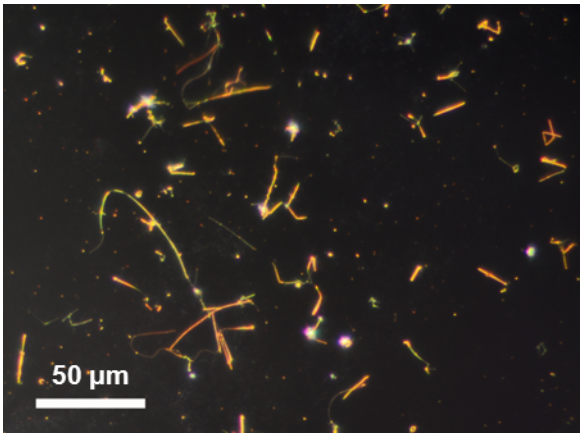

Figure 29 Optical dark field image of gold nanobelts produced in a typical synthesis. A range of nanobelt lengths, plasmon resonant frequencies, and structures are produced by the synthesis.

Several examples of uniformly tapered nanobelts are displayed in Figure 30, where the width variation occurs over lengths scales of nanometers to microns. The transmission and scanning electron micrographs (Figure 30a and Figure 30b respectively) directly display the variation in width, while the dark field optical image (Figure 30c) shows it indirectly through the variation in color. A single tapered nanobelt was analyzed

in detail by correlated atomic force microscopy and microspectroscopy. The peak wavelength and cross-sectional aspect ratio (width/ height) are plotted in Figure 31 along with the previously reported points for uniform nanobelts.[82] The tapered nanobelt peak wavelengths match those from uniform nanobelts, and confirm that the shift in color is due to a change in cross-sectional aspect ratio.

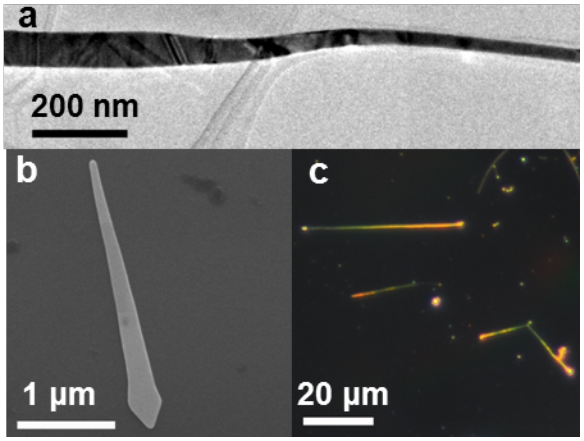

Figure 30 (a) TEM, (b) SEM, and (c) optical dark field images of tapered gold nanobelts that occur at different scales.

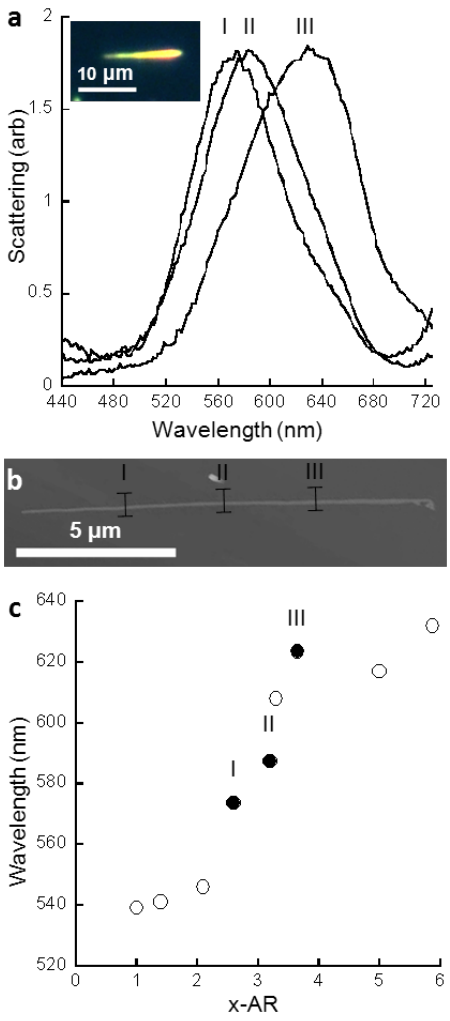

Figure 31 A tapered gold nanobelt characterized by (a) dark field microscpectroscopy showing spectra taken as a function of position along the belt (dark field image inset), (b) AFM. (c) The spectral peak wavelength along the tapered nanobelt (filled circles) plotted against x-AR with the spectral peak for uniform belts from a Section 3.2 (hollow circles).

3.3.2 The "Plasmometer"

The spatial dispersion of the plasmon resonant wavelength enables the tapered nanobelts to act as mesoscopic spectrometers for plasmonic interactions. Here, light emission from quantum dots near tapered gold nanobelts is described as an example. Plasmonic nanostructures enhance the electromagnetic field near their surface, which can

increase the absorption cross section and therefore enhance the excitation rate of a chromophore. The radiative decay rate may also be enhanced, and together these effects can increase the brightness of a nearby chromophore.[83, 84] The plasmonic nanostructure can also open new non-radiative decay channels, resulting in quenched chromophore emission.[85] These interwoven effects each have complicated dependences on the chromophore's position and orientation relative to the nanoparticle, the nanoparticle's electromagnetic near field enhancement pattern, and the spectral properties of both the plasmonic nanostructure and the chromophore. However, it is important to deconvolute their effects especially since excitation and emission contribute to different applications.[86] This has been achieved by studying different nanoparticles at different plasmon energies,[62, 86-90] but tapered gold nanobelts may bring unique capabilities due to the spatial separation of a continuum of plasmon resonances.

3.3.3 Methods

To demonstrate their spectroscopic capabilities, gold nanobelts on a glass substrate were then covered with a 20 nm thick layer of evaporated SiO, then spin-coated with a ~50nm polystyrene containing CdSe/ZnS quantum dots. CdSe/ZnS core/shell quantum dots capped in octadecylamine were purchased from Ocean NanoTech. The quantum dot emission peak was centered at λ_{em} = 600 nm with a quantum yield of over 50% (emission profile shown in Figure 32). The quantum dots were first dispersed in toluene at a concentration of 10mg/ mL. A 2% polystyrene solution in toluene was then prepared. Finally, a mixture of 588 uL of the 2% polystyrene solution and 12 uL of the quantum dot solution was prepared.

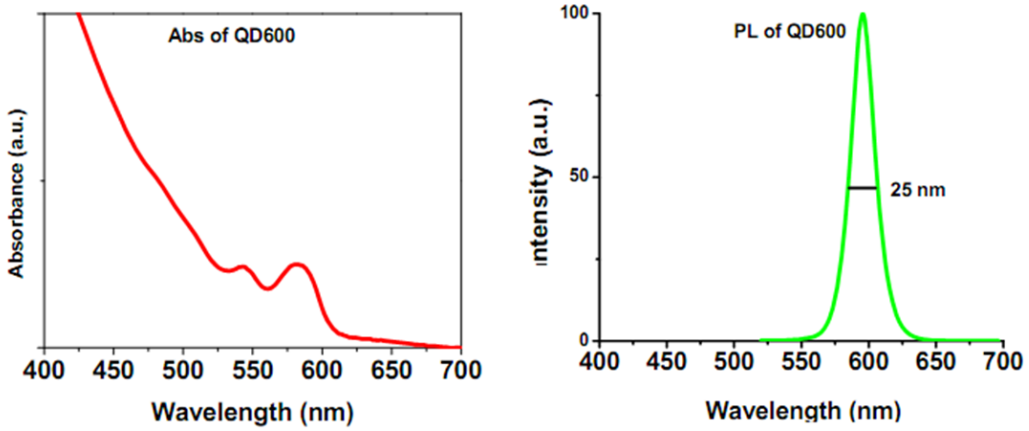

Figure 32 Emission profile of quantum dots used for emission enhancement studies, reproduced from specifications provided by Ocean NanoTech.

The spin coating process causes the quantum dots to segregate into domains on top of the film. This, along with the SiO layer results in the quantum dots being well-separated from the nanobelts (see AFM images in Figure 33).[91]

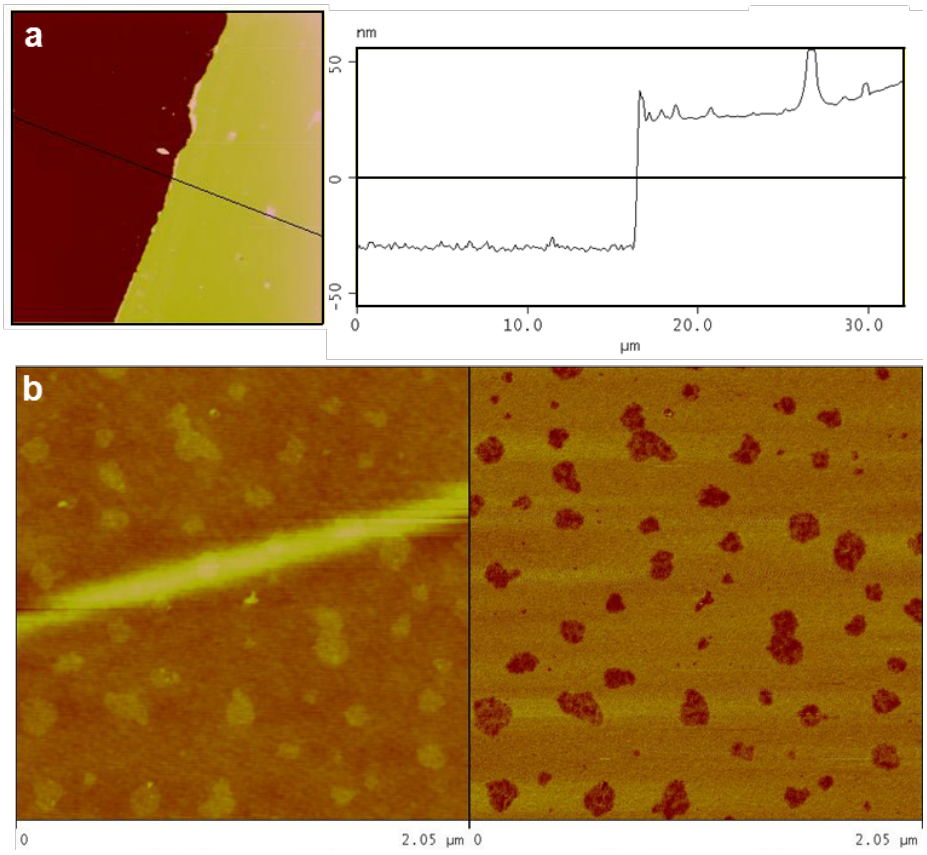

Figure 33 AFM of a glass substrate with a gold nanobelt that is covered by a polystyrene film with CdSe quantum dots. The (a) section analysis reveals the film thickness and (b) reveals islands of CdSe quantum dots situated on top of the polystyrene.

Dark field images were obtained with the same microscope and objective as the dark field system described section 2.3. Fluorescence images required using a fluorescence filter set rather than dark field illumination annulus and a Nikon D5000 color camera. The quantum dot emission and filter set curves are shown in Figure 34. Fluorescence images in counts were converted to emission enhancement by dividing the image counts by the average background counts from a region with no nanobelt. In this way, the emission enhancement of the background is 1 (no enhancement) and the image directly displays the enhancement above the nanobelts.

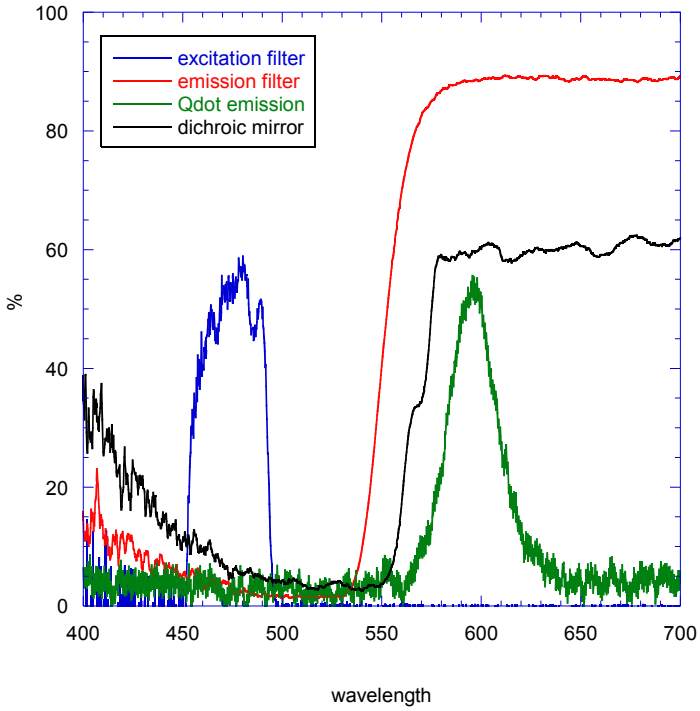

Figure 34 The spectral transmittance of the fluorescence filter set and the measured spectral quantum dot emission.

3.3.4 Results

Figure 35 presents both dark field scattering and fluorescence microscopy images of three tapered nanobelts on the substrate. For each nanobelt, the dark field image reveals which end is resonant near the emission peak of the quantum dots (λ_{em} = 600 nm). The enhancements are clearly more prominent at the red end of the nanobelt where the plasmon resonances match the quantum dot emission, which indicates an enhanced rate of emission rather than excitation. The enhancement values near the nanobelts are similar in magnitude to those reported for quantum dots near single silver nanoprisms.[86] Also, if quenching were to occur off the emission resonance, it would appear as a dip in

the fluorescence background, which is not observed for sufficient nanobelt/quantum dot spacer layers.

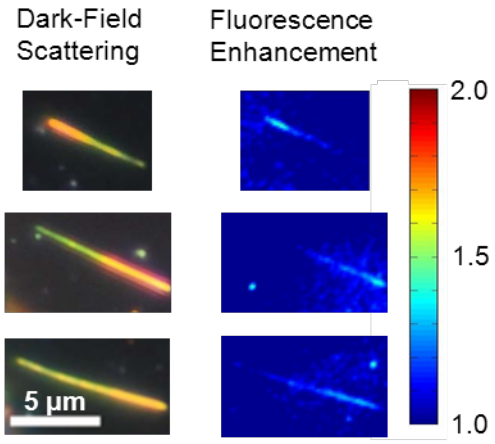

Figure 35 Quantum dot emission enhancement near a tapered gold nanobelt. The dark field images illustrate the wavelength and spatial location of the plasmon resonances, while the fluorescence images show increased quantum dot emission at the red end of the taper.

3.3.5 Conclusion

Tapered nanobelts have uniformly varying cross-sectional aspect ratio and peak plasmon frequency along their length. This spatial dispersion creates mesoscopic "plasmometers" to study enhanced light emission or other plasmonic effects. This capability was demonstrated by the spatially varying emission enhancement of quantum dots near tapered nanobelts.

3.4 Split Gold Nanobelts

3.4.1 Introduction

Another novel product of the nanobelt synthesis (Section 3.1.1) that is regularly found in these samples is the nanobelt dimer. In this structure, two nanobelts run side by side with a small, uniform sub-10 nm gap for lengths greater than one micron. Images of nanobelt dimers, displayed in Figure 36, suggest that these can form when two nanobelts come together upon deposition (Figure 36a, b). In other cases, it appears that the nanobelt splits during synthesis (Figure 36c) leading to two parallel daughter nanobelts. Nanobelt dimers may serve as an interesting nanostructure geometry for plasmon hybridization,[92] and they may create unique modes for plasmon propagation along the nanobelts considering they concentrate the electromagnetic field in the space between the nanobelts similar to plasmonic slot waveguides.[93-95] Plasmonic substrates have been shown to increase the molecular Raman Scattering signal from the bond vibrations within molecules near the metal surface because of large electric field enhancements. Because of the large gap with a well-defined spacing, nanobelt dimers may also serve as substrates for analytical SERS applications, which rely on large volumes of well-defined electromagnetic field enhancement.[96-98]

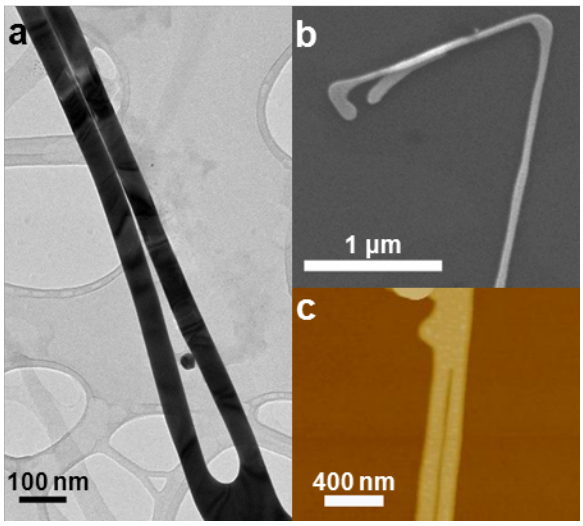

Figure 36 (a) TEM image of a gold nanobelt dimer showing that the two branches of the nanobelt run together with a uniform gap and (b) SEM of a nanobelt as it splits. (c) AFM imaging can also identify nanobelt dimers.

3.4.2 Methods

To evaluate their potential for analytical SERS, nanobelts were deposited on a glass slide from their native mixed surfactant solution and dried. A nanobelt dimer was located by AFM relative to alignment marks. SERS measurements were taken on the nanobelt dimer, on a single nanobelt, and on the bare glass substrate, all of which were covered with surfactant. Figure 37 displays the AFM image of the nanobelt dimer and includes an optical view of the excitation laser spot location. The laser was polarized horizontally across the vertically aligned nanobelt dimer.

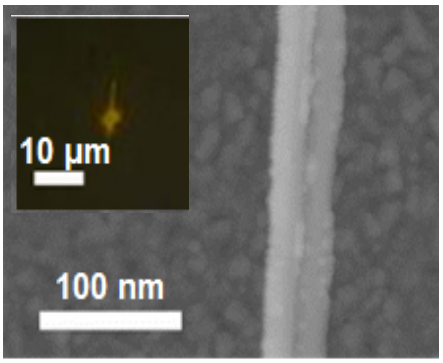

Figure 37 AFM of a nanobelt dimer with (inset) the optical image of the dimer in the Raman microscope.

To analyze the magnitude and spatial distribution of the field enhancement in the nanobelt dimer, the structure was simulated using the commercially available Finite Element Method (FEM) package, COMSOL Multiphysics (for step-by-step details of the simulation set-up, see Appendix D: COMSOL Multiphysics Simultation). The dielectric function of gold was taken from Johnson and Christy[78] and was interpolated using a linear interpolation method. Since the AFM image do not provide a precise gap size, a typical structure was simulated based on TEM observations: two 20 nm by 50 nm nanobelts separated by a 3 nm gap (Figure 38).[96] A schematic of the simulated nanobelt dimer is shown in Figure 39.

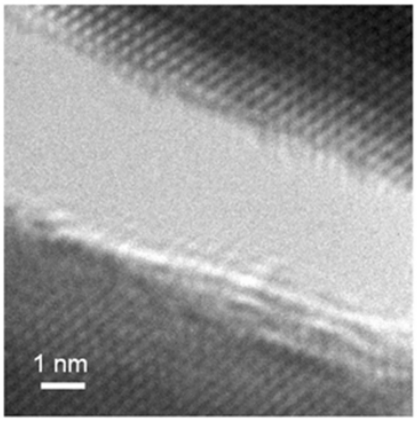

Figure 38 A high-resolution image of the gap of a nanobelt dimer.

Figure 39 Schematic of the nanobelt dimer.

The nanobelt dimers were simulated as 2D cross sections with infinite length. The simulated belt edges had a radius of curvature of 2nm. Perfectly sharp corners may pose problems with FEM techniques; also, perfectly sharp nanobelt corners are not physically realistic. A 1.1 μm circular simulation space surrounded the dimer cross section with a 200 nm thick perfectly matched layer (PML) to absorb waves reflected from the simulation space boundaries. The electromagnetic enhancement ($g = E/E_0$) was calculated at both the incident laser wavelength of 785 nm and a Raman shifted wavelength of 858 nm (which corresponds to a ~1200 cm^{-1} shift typical of a hydrocarbon mode), which was polarized perpendicular to the gap.

3.4.3 Results

SERS measurements were preformed on the nanobelt dimer shown in Figure 37. These measurements were compared with the signal from the glass substrate and single nanobelt. Both the glass and single nanobelt showed no significant SERS signal. The nanobelt dimer yielded several strong peaks between 900 and 1500 cm^{-1} which correspond to alkane chain modes of the surfactants (Figure 40).[96]

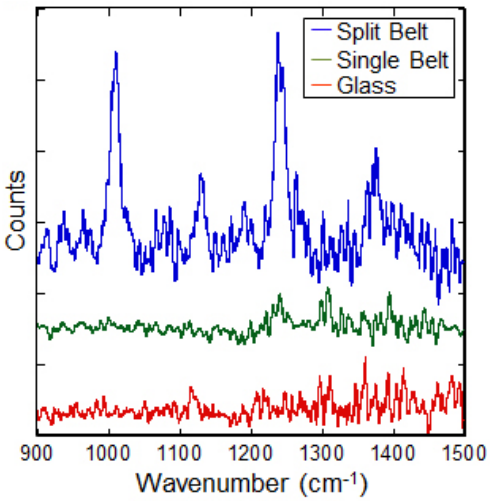

Figure 40 The corresponding SERS of dried surfactant on the nanobelt dimer (blue), on a single nanobelt (green), and on the glass substrate (red).

The result of the COMSOL simulation are shown in Figure 41, show a region between the nanobelts with field enhancements (g, g', where the prime denotes the field at the scattered frequency) reaching 16 and 12 for the incident and scattered wavelengths respectively, and yielding an overall enhancement factor ($EF = |gg'|^2$) of ~37,000. The total enhancement is not especially high, but that is expected given the large separation (relative to typical hot spots) and the lack of curvature in one dimension. The enhancement is similar to those at the ends of gold nanorods that were observed in a

recent analytical SERS study with this instrument (15,000 – 84,000).[96] Simulations of a single nanobelt generate a field enhancement at the corners of approximately 6 and an enhancement factor of only 1300 (shown in Figure 42).

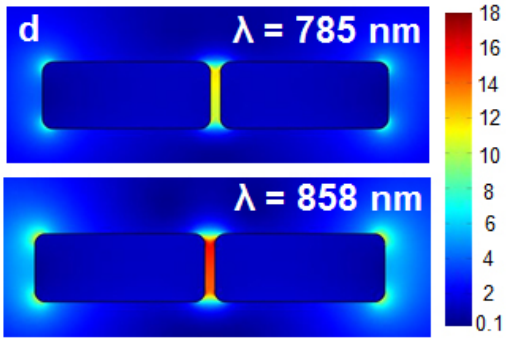

Figure 41 The theoretical electromagnetic enhancement of its cross section with a 3 nm gap at (top) 785 nm and (bottom) 858 nm.

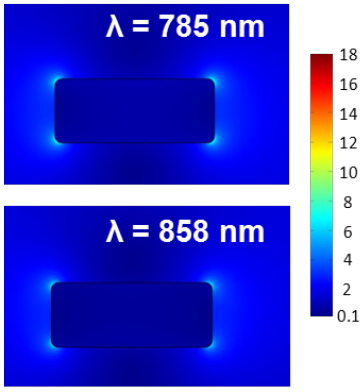

Figure 42 Electric field enhancement of a single belt at (top) 785 nm and (bottom) 858 nm.

Calculating the SERS enhancement factor, ($EF = |gg'|^2$) in between the belts for the 1200cm^{-1} Raman shift (hydrocarbon mode) for a range of excitation wavelengths, the near-field enhancement spectrum for a belt dimer is shown in Figure 43. With small nanobelt seperations, these spectra are highly sensitive to the gap size, however, in theory, could be used to optimize future experiments.

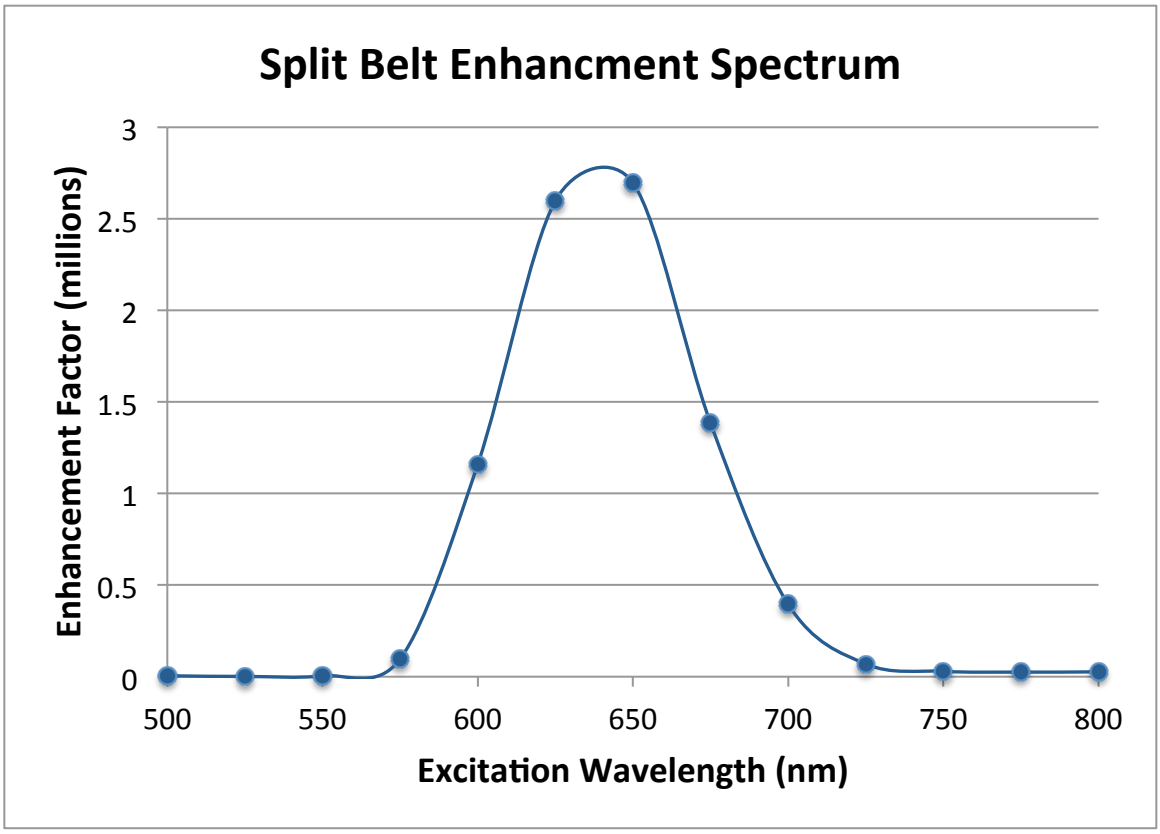

Figure 43 SERS enhancement spectrum the 1200cm^{-1} shift hydrocarbon mode for various excitation wavelengths for two parallel 20 x 50nm gold nanobelts with a 3nm separation.

The same procedure for the single belt gives us the SERS Enhancement factor near one corner of the belt (highest region of enhancement) (Figure 44). The enhancement spectrum is weaker, blueshifted, and more narrow than the belt dimer case, as would be expected.

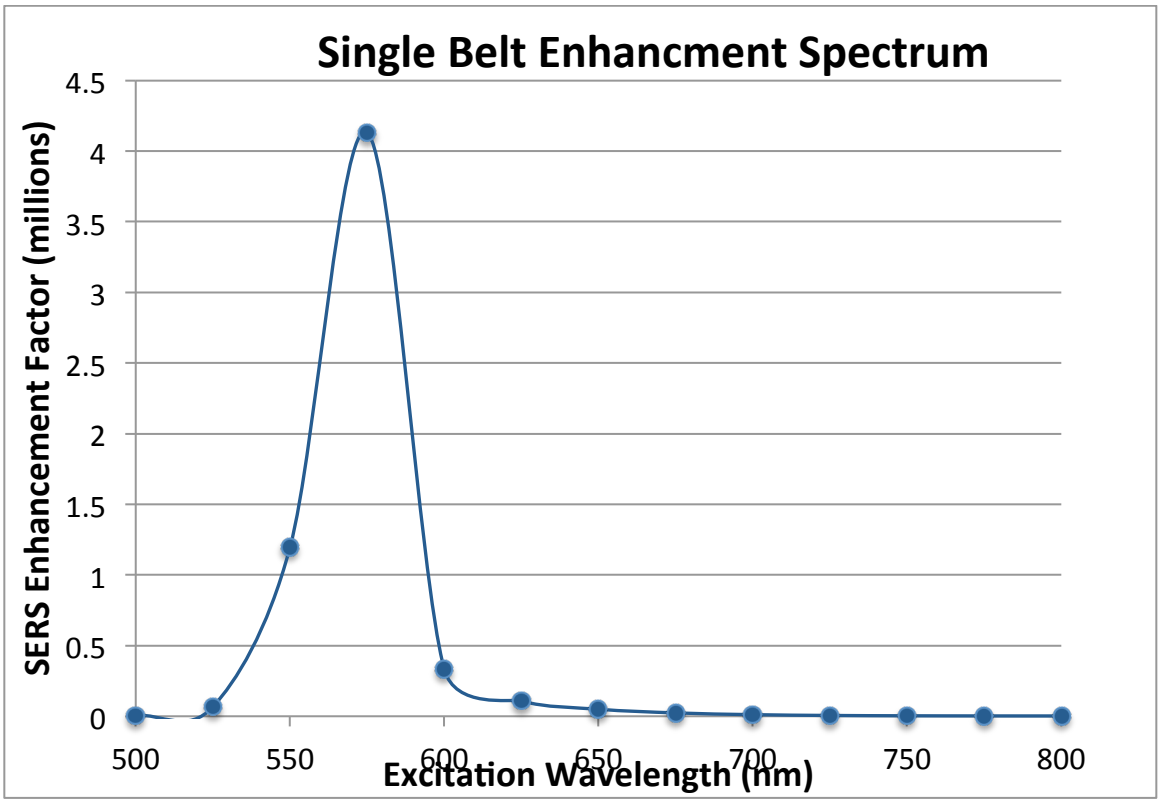

Figure 44 SERS enhancement spectrum the 1200cm^{-1} shift hydrocarbon mode for various excitation wavelengths for a single 20 x 50nm gold nanobelt.

3.4.4 Conclusion

Nanobelt dimers with uniform sub-10 nm gaps over micron-scale lengths were described. These structures have sufficient electromagnetic field enhancement to yield SERS spectra from molecules in the gap, and uniquely create large enhancement volumes since the gap runs through the entire excitation beam spot. These nanostructures are created by a simple chemical synthesis and can be easily identified by optical or AFM imaging, making them widely available for further study and development.

3.5 Gold Nanobelts as Plasmonic Waveguides

3.5.1 Introduction

Gold and silver nanostructures have been actively investigated for manipulation of light at the nanometer scale since they localize light to deep sub-wavelength dimensions through the formation of surface plasmons. [13] Nobel metal nanowires support surface plasmons that propagate along their length. These propagating plasmons may serve as interconnects in future nanophotonic circuitry, where light is coupled into one end of a nanowire and emitted at the other.[42, 46, 56, 99] Looking beyond the classical description, propagating plasmons in nanowires are quasiparticles that retain the quantum information of the photons that generate them.[100-103] Intriguing device architectures have been considered based on strong interactions between quantum emitters and plasmonic nanowires, including all optical transistors and single photon sources.[51, 53] However, the intrinsic losses in gold and silver at optical frequencies limit the propagation distances to several microns. Recent attention has focused on characterizing the propagating modes, and how the propagation lengths depend on nanowire geometry, wavelength, dielectric environment, substrate, and metal crystallinity. [43, 56, 57, 104-110]

Silver exhibits lower intrinsic losses than gold, and has been the focus on most work on plasmon propagation in nanowires.[43, 56, 101, 108-112] The propagation can be directly measured with far field optics by focusing a light at one end of the nanowire and observing emission at the other end. Chemically synthesized silver nanowires yield the longest propagation lengths, while lithographically fabricated wires offer the opportunity to investigate complex nanowire architectures. Reflections of surface plasmons at nanowire ends result in Fabry-Perot resonances within the nanowire which can be probed to

extrapolate the wavelength and decay length of propagating plasmons.[56, 105, 107-110, 112] Experimental results are in good agreement with both analytical solutions and numerical simulations using the measured dielectric function of silver.

There is much interest in increasingly thinner nanowires to explore strong interactions between propagating plasmons and nearby quantum emitters.[55] However, smaller diameter nanowires have shorter propagation lengths and weaker emission signals. In addition, gold is superior to silver in terms of chemical stability and ease of functionalization, but again the higher intrinsic loss in gold leads to shorter propagation lengths. Plasmon propagation in gold nanowires is therefore difficult to study with far field optics since the emitting nanowire end will be dim and imaged very close to the brightly scattering excitation end. Recent reports have found alternative methods to study gold nanowire propagation. Through excitation by total internal reflection at the surface of a prism, emission from lithographically fabricated gold nanowires was observed and spectrally analyzed. A Fabry-Perot model yielded a decay length of 2 to 4 μm depending on frequency, although the Fabry-Perot fringes were not as clear as those for silver nanowires.[105] Propagation in gold nanowires has been observed by near field excitation of fluorophores. Fluorescence images of Coumarin 30 near the nanowires yields propagation lengths of 2.4 to 3.6 μm.[107] Also, a method has been developed based on the near field bleaching of flourophores and monitoring their recovery. This yields propagation lengths of 1.8 +/- 0.4 μm at a wavelength of 532 nm[57] and 7.5 +/- 2.0 μm at 785 nm.[106] With this method, the fundamental propagating mode (m=0) is quenched by the fluorophore layer. The longer measured propagation length in these experiments was found to be due to a higher-order propagating mode (m=1) which decays much slower

than the fundamental propagating mode. All of these results are in reasonable agreement with theory, but each is either indirect or relies on models with some assumptions (such as reflectance coefficients of the nanowire ends) or some ambiguity regarding the propagating mode.

3.5.2 Methods

Gold nanobelts are attractive structures for plasmon propagation due to their single crystal gold structure, their relatively small cross-sectional size for strong confinement, and their flattened cross sections, which may lead to stronger interactions with nearby emitters. For plasmon propagation experiments, gold nanobelts on glass substrates were imaged with an oil immersion 100X/NA=1.25 objective under epi-brightfield illumination with a white light emitting diode (LED). To observe plasmon propagation, a separate 850 nm LED was positioned approximately 1 meter behind the objective lens and coupled in with a pellicle to produce a tightly focused spot in the object plane. The focused light was placed at one end of the nanobelt and light emission was observed at the other end, as seen for two short nanobelts in Figure 45. Efforts to generate propagation images like those in Figure 45 with focused laser spot were unsuccessful due to the background of interference fringes and speckle patterns inherent to high coherence illumination. With low coherence LED illumination, the background is smooth and easily subtracted.

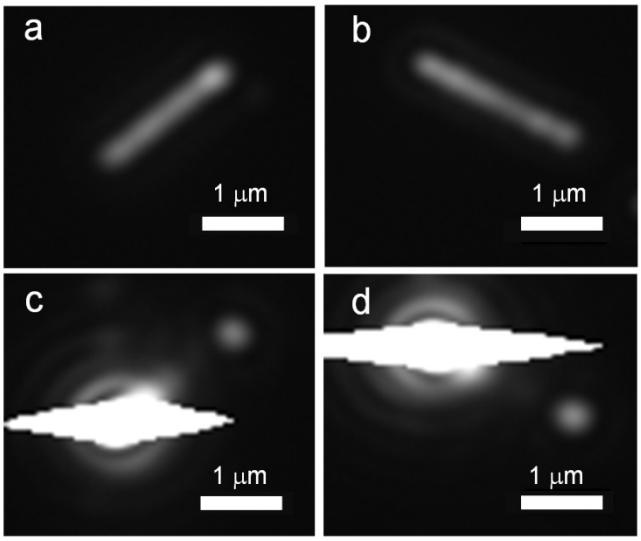

Figure 45 Two gold nanobelts imaged with a,b) epi-bright field illumination and c,d) focused illumination to display propagation. The left nanobelt (a,c) is 1.6 μm in length and the right nanobelt (b,d) is 1.8 μm. The illumination wavelength is 850 nm.

To compare these measurements with previous reports on silver nanowires, similar experiments were performed with 100 nm diameter silver nanowires synthesized following the extensive parametric polyol synthesis study by Coskun et al.[113] Using a polyvinylpyrrolidone (PVP, MW = 55,000) to silver ratio of 3:1.[1] A 10 mL solution of ethylene glycol containing 0.45 M PVP (monomer-based molarity) and 0.007g NaCl was heated in a round bottom flask to 170 °C under moderate stirring. Once the solution was at a constant temperature, 5 mL of 0.12 M $AgNO_3$ dissolved in ethylene glycol was injected into the flask at a rate of 5 mL/hour. After all of the $AgNO_3$ solution was added, the flask was held for an additional thirty minutes at 170 °C before being cooled to room temperature. At this point the solution was opaque and pale gray in color.

The solution was then added to 75 mL of acetone and centrifuged at 6,000 rpm for 20 minutes. The supernatant was decanted. The remaining gray precipitate was then resuspended in acetone and washed again following the same procedure. Finally, after the second round of decantation, ethanol was added and the resulting product was briefly

probe sonicated to suspend the nanowires. The silver nanowires were imaged by optical dark field (Figure 46), atomic force microscopy (Figure 47), and transmission electron microscopy (Figure 48), and plasmon propagation (Figure 49) was studied as described in the text.

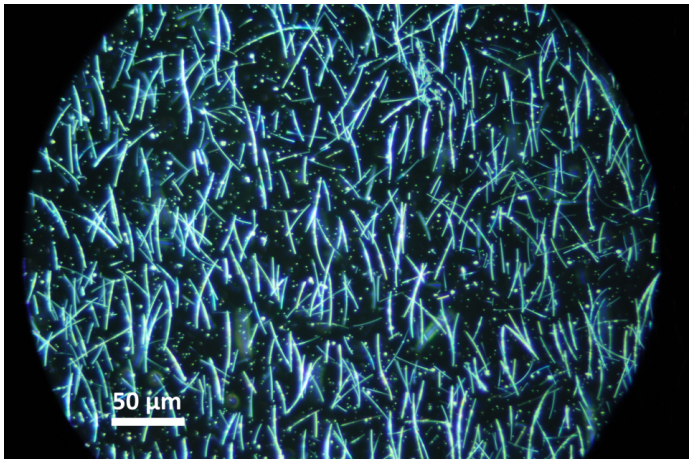

Figure 46 An optical dark field image of the silver nanowires in solution.

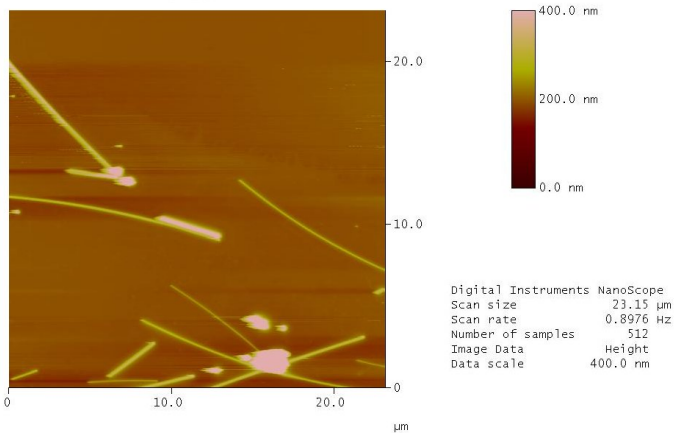

Figure 47 Atomic force microscopy images, recorded on glass with tapping mode, of silver nanowires.

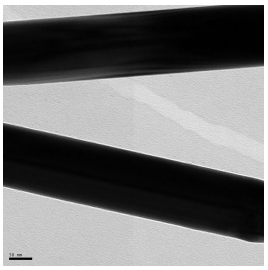

Figure 48 A transmission electron micrograph of two silver nanowires. The scale bar is 50 nm.

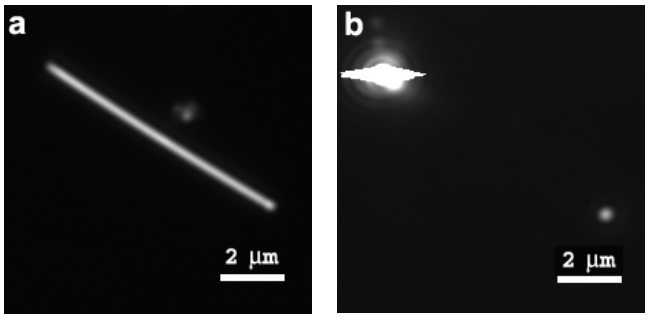

Figure 49 A single silver nanowire (a) imaged in epi-bright field at 850 nm, and (b) imaged with an 850 nm LED focused at one end. The emission at the other end is seen in the lower right corner.

3.5.3 Plasmon Propagation Lengths in Gold Nanobelts

The propagation lengths were determined from measurements on gold nanobelts and silver nanowires with different lengths. However, the data must be corrected for different nanowire diameters and nanobelt heights and widths since the size affects the quantity of light absorbed and re-emitted. Rather than correct the data with detailed size measurements and scattering calculations, three relevant processes that scale with size were considered for a cylindrical nanowire of radius r, as illustrated in Figure 50a. At the illuminated end the absorption of light will scale as r^3 (roughly treating the nanowire end

as a sphere). Emission at the distal end will also scale approximately as r^3. Taken together, the entire process will scale as r^6. Direct scattering at the illuminated end also scales as r^6 (again approximating the end as a sphere) and can be measured from the experimental images. Both the excitation scattering and distal emission images were converted to signal rates (counts/second), and the emission and excitation scattering were scaled for each nanobelt or nanowire. The ratio is plotted versus nanowire length in Figure 50 for both silver nanowires and gold nanobelts. Uncertainties were taken as the square root of the total counts for both the tip image and the nearby background. The data were fit to simple exponential decay by nonlinear least squares regression, weighting each data point by its uncertainty. The resulting propagation lengths were 8.0 μm for silver nanowires (with a 3.6 to 35 μm 95% confidence interval) and 0.94 μm for the gold nanobelts (with a 0.61 to 2.1 μm 95% confidence interval).

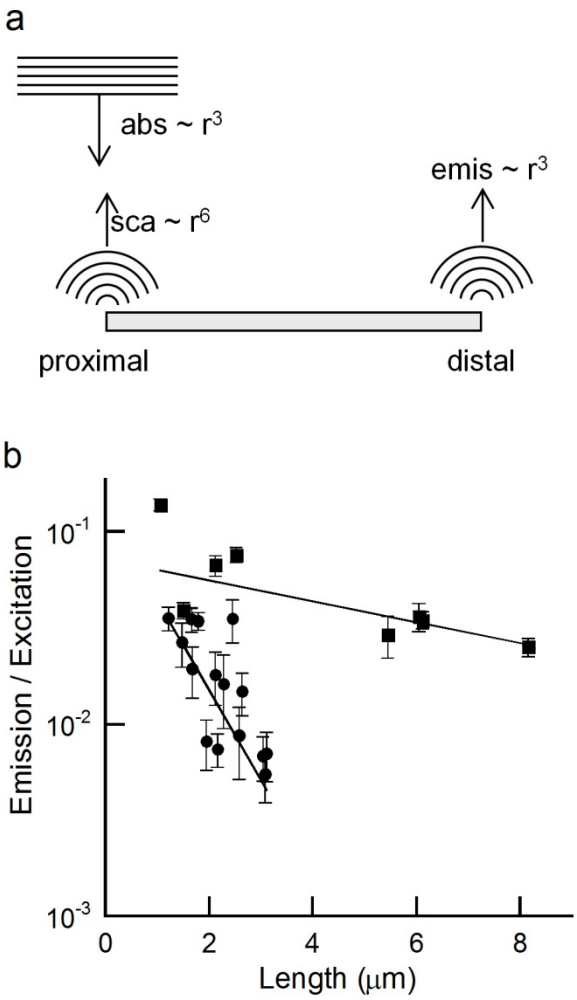

Figure 50 The plasmon propagation length of gold nanobelts and silver nanowires. a) A schematic that illustrates the scaling rationale. b) Emission/excitation rates for gold nanobelts (circles) and silver nanowires (squares), with the exponential decay fits resulting in 0.94 and 8 μm propagation lengths, respectively.

Even using the emission/excitation ratio to account for different sizes, there is still significant scatter in the data and significant uncertainty in the resulting propagation lengths. While plotting the emission/excitation ratio accounts for the different signal magnitudes, it does not account for the fact that different nanowire diameters have different decay lengths. Since each point in Figure 50 corresponds to a nanowire or nanobelt of different size, each point also corresponds to a different plasmon propagation

length, and the resulting fit is therefore an average. The expected propagation lengths for thin cylindrical gold nanowires were calculated by solving the electromagnetic wave equation for an infinitely long right circular cylinder. Boundary conditions lead to the following characteristic equation for the fundamental mode:

$$\frac{k_2^{\,2}}{\sqrt{k_2^{\,2}-k_p^{\,2}}}\frac{J_o'\left(\sqrt{k_2^{\,2}-k_p^{\,2}}R\right)}{J_o\left(\sqrt{k_2^{\,2}-k_p^{\,2}}R\right)}-\frac{k_1^{\,2}}{\sqrt{k_1^{\,2}-k_p^{\,2}}}\frac{H_o'\left(\sqrt{k_1^{\,2}-k_p^{\,2}}R\right)}{H_o\left(\sqrt{k_1^{\,2}-k_p^{\,2}}R\right)}=0 \qquad (1)$$

Following Chang et al,[55] R is the nanowire radius, k_1 is the wave vector in the surrounding dielectric medium and k_2 is the wave vector in the nanowire:

$$k_1=\sqrt{\varepsilon_1}k_o \qquad\qquad k_2=\sqrt{\varepsilon_2}k_o$$

where ε_1 and ε_2 are the dielectric functions of the medium and nanowire, respectively. k_o is the magnitude of the vacuum wave vector and J_o and H_o are Bessel functions. The surrounding dielectric of immersion oil and glass was set to ε_1=2.23 and ε_2 was assumed to be the dielectric function of gold from Johnson and Christy.[78] The solution to this equation reveals the complex wave number for a specific nanowire diameter and excitation wavelength. The imaginary part of the wave number, k_I, yields the expected propagation length. The predicted decay lengths for gold cylinders are shown in Figure 51. The measured average propagation length (line) and 95% confidence interval (dash) are shown.

.

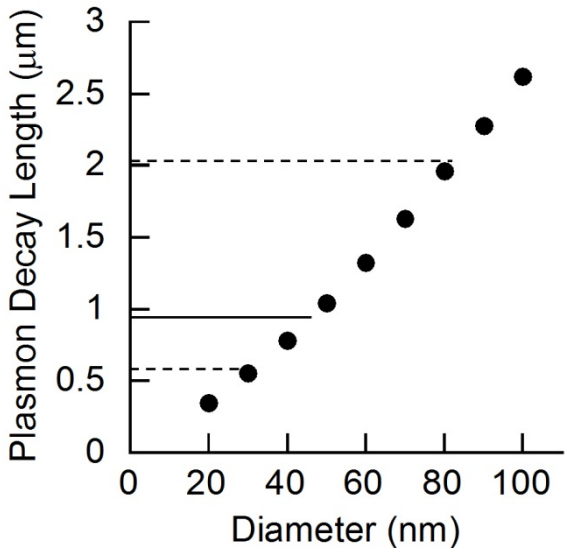

Figure 51 The calculated plasmon decay length as a function of nanowire diameter for cylindrical gold nanowires in a surrounding dielectric.

The average propagation length measured for gold nanobelts is what one would expect for 45nm diameter gold wire, and 30-80nm diameter wires fall within the confidence interval of the measurement. The gold nanobelt propagation lengths are therefore, within the range of what would be expected for a structure of this size.

3.5.4 Propagating Modes

Figure 52a and Figure 52b show a dark field and propagation image, respectively, for a particular gold nanobelt that was measured in AFM. The 5.5μm long, 125nm wide, 40nm tall belt has the smallest cross-sectional area of any elongated structure that has been shown to support propagating plasmons. From earlier characterizations of nanowire modes,[106, 107] two dominant propagating modes were expected. Figure 52c shows the calculated charge distribution for a nanobelt of this size (topview) of both the fundamental m=0 mode and the higher-order m=1 mode. The fundamental mode is generally the expected propagation mode for thinner nanowires.[50] Figure 52d shows the

FDTD-calculated Poynting vector on a logarithmic scale. This plot of the directional energy flux is proportional to the emission that would take place if the belt were to terminate at that given length. Simulations predict that the m=0 mode is much stronger at shorter lengths, but decays more quickly than the m=1 mode, leaving the m=1 mode to dominate at longer lengths.

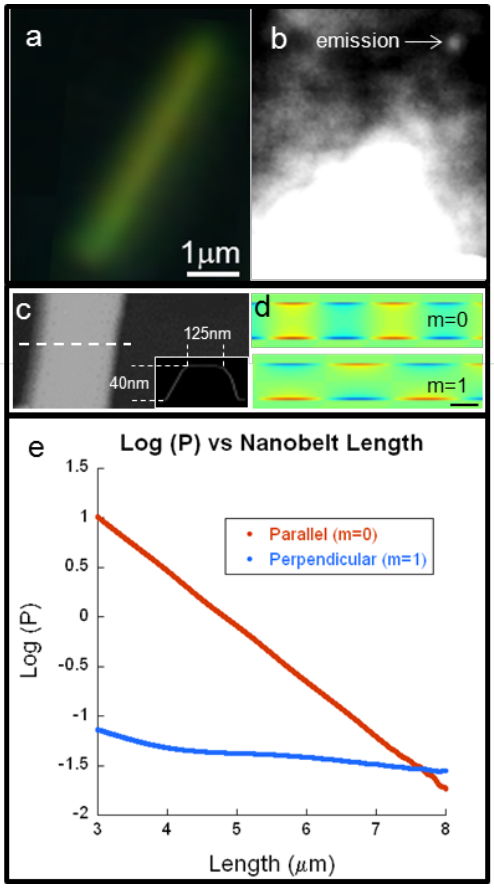

Figure 52 a) Dark field image of 5.5µm long, 125nm wide, 40nm tall gold nanobelt. b) Plasmon propagation image of the same nanobelt, illuminated at one end with a 850nm LED. c) AFM of the nanobelt cross section. d) Calculated charge distribution for the fundamental m=0 mode and the higher-order m=1 mode (scale bar = 100nm). e) Calculated Poynting vector for two propagating modes along a 125nm x 40nm nanobelt.

To illustrate how sensitive the mode cross-over length is to geometry, Figure 53 shows the propagation length for the m=0 and m=1 modes for a 100nm wide, 25nm tall

nanobelt. Here, the cross-over to the m=1 mode dominating happens at a much shorter length (~5.2mm) than the 125nm x 40nm nanobelt (~7.6mm).

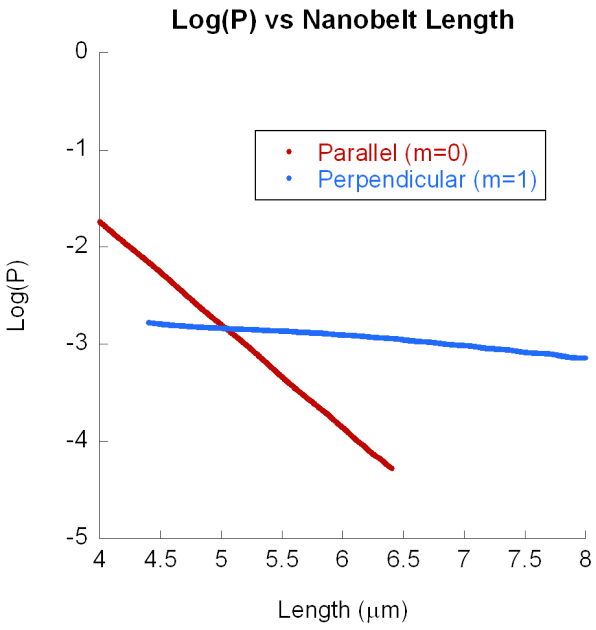

Figure 53 Calculated Poynting vector for two propagating modes along a 100nm x 25nm nanobelt.

FDTD calculations show that for this experimental geometry, the m=0 mode results in emission at the nanobelt tip that is highly polarized parallel to the belt length and the m=1 mode emission is polarized transverse to the belt. Angular scattering patterns for a 125nm x 40nm nanobelt lying along the vertical axis are shown in Figure 54. These signals were integrated over the experimental detection angle to find that for the m=0 mode, tip emission in the longitudinal polarization is ~7 times greater than in the transverse polarization. For the m=1 mode, the transverse polarization emission is ~30 times that of the longitudinal polarization.

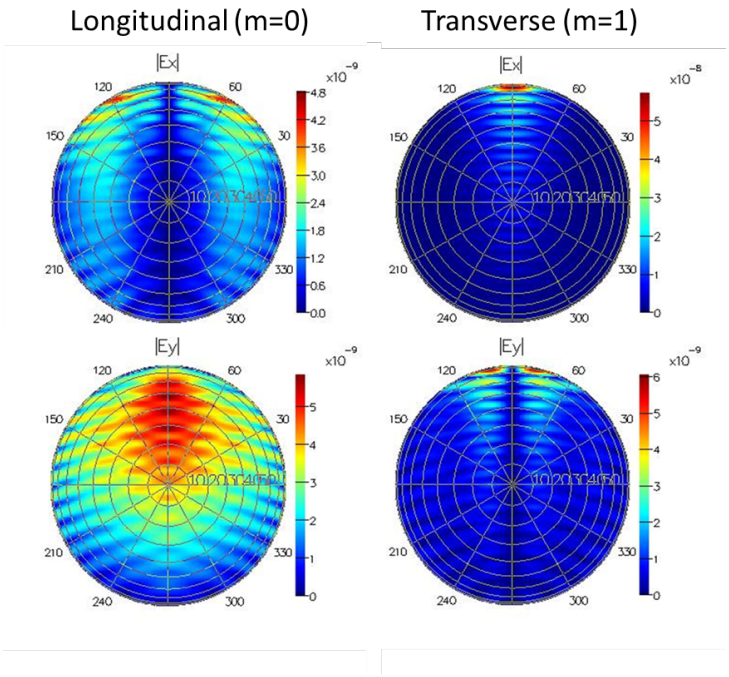

Figure 54 The angular scattering patterns of the tip emission for both modes, x and y polarizations.

This result makes sense based on the direction of the electric fields in both cases and considering that light is always emitted perpendicular to an electric field. The fundamental mode results in electric fields perpendicular to the belt, the m=1 mode parallel to the belt (Figure 52). To identify the propagation modes present, a Wollaston prism was placed in the path of the emitted and scattered light. This element consists of two orthogonal calcite prisms, connected at their bases, which spatially separate the two polarizations of the signal. One axis of the prism was rotated to the orientation of the nanobelt on the sample so that the resulting images were of the light emitted parallel and perpendicular to the nanobelt. Nanobelts of similar brightness to that of the nanobelt measured in AFM were chosen. Measurements on nanobelts with geometric defects or bulbus end shapes were ignored as it was seen to affect the emission polarization.

Figure 55a and Figure 55b display doubled propagation images with both polarizations of the scattering and emission signals for a 2.4μm and a 5.8μm long gold nanobelt, respectively. In order to get measurable emission for the longer nanobelt in part b, the excitation signal was saturated. The scattering at the excitation end of the shorter nanobelt, however, is visibly polarized more strongly perpendicular to the nanobelt (part a, left), as expected based on the previous study of resonant nanobelt scattering in Section 3.2. In both cases, the emission is highly polarized along the nanobelt length. This confirms that the light imaged at the distal end is not simply scattered from the illumination beam spot or from the excitation end, since it would either be polarized perpendicular to the nanobelt or be unpolarized. Emission polarization along the nanobelt length suggests that the plasmon propagation is primarily due to the fundamental mode (m=0) where the sign of the charge has no azimuthal angle dependence. As predicted, the difference between the two polarizations in the longer belt is less than the difference of the two in the shorter belt.

For belts of this geometry, the calculated cross-over for the m=1 mode to dominate should happen at over 7.6μm (Figure 52). Highly uniform nanobelts of this length are difficult to find, but a comparison of the polarized emission signals from nanobelts at several lengths reveals that the ratio of parallel to perpendicular light emitted at the nanobelt tip decreases exponentially as predicted by the simulations (Figure 55c). An exponential fit of these data give a cross-over length of 7.7μm, which is in very good agreement with the FDTD calculation shown in Figure 52, considering error and geometric heterogeniety.

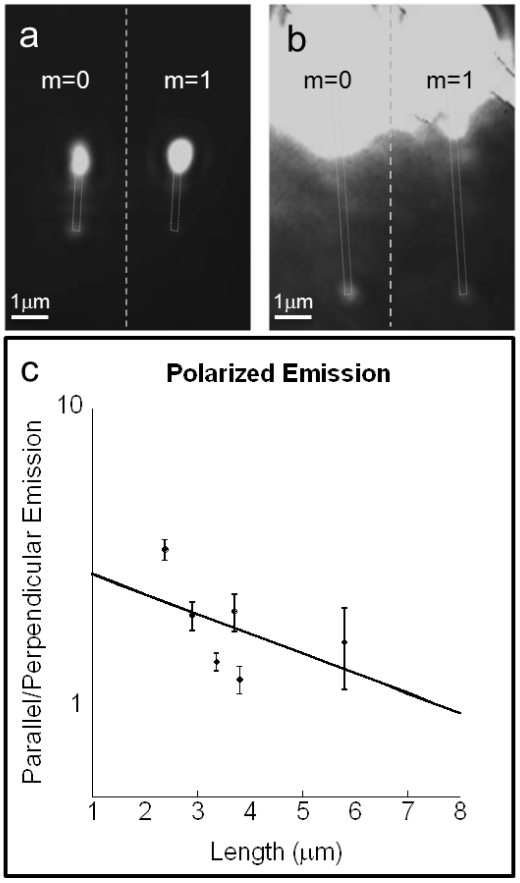

Figure 55 a) Plasmon propagation through a gold nanobelt for scattering and emission polarizations perpendicular (blue) and parallel (red) to the belt. (scale bar = 1μm) b) The ratio of the parallel to perpendicular components of the emission for several nanobelts.

3.5.5 Confinement of Energy

For further insight into the propagation lengths of the m = 0 and m = 1 modes, their cross-sectional field intensity and corresponding heat distribution were calculated by FDTD (Figure 56). The m = 0 mode generates higher intensity fields than the m = 1 mode, but most of the m=1 field intensity is localized outside the nanobelt in the dielectric medium. The loss is mostly due to heat generation due to the field just inside the metal, which can be difficult to predict based on static charge distributions like Figure

52d. However, the heat plots in Figure 56 make it clear that the m = 0 mode also has higher losses, especially near the metal's surface, where the field intensity is highest. This is why the m=0 mode has a shorter propagation length than the m = 1 mode.

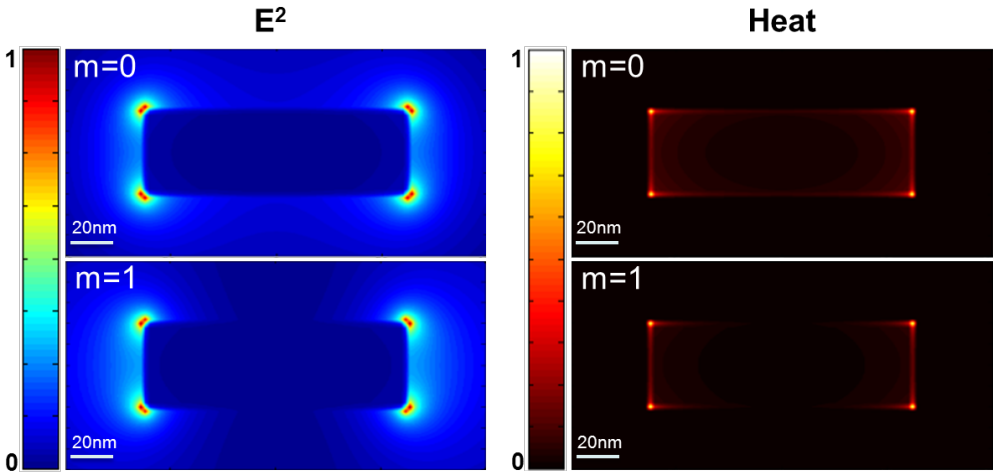

Figure 56 Cross sections of intensity (left) and heat distribution (right) in a 125 x 40 nm gold nanobelt for both the m=0 and m=1 modes. Arbitrary Units, Scale bar = 20nm.

Note that all simulations were done for nanobelts with infinitely sharp corners, which is not physically realistic. Not having the measurement sensitivity to measure the corner curvature, all calculations were repeated on a nanobelt with a realistic corner radius of 4nm. It was seen that accounting for curvature made less than 10% difference in the propagation length, and since it lowers both the mode area and the propagation length, the figure of merit was relatively unchanged.

For plasmonic waveguides there is a trade-off between high field confinement, which strengthens interactions with nearby emitters, and propagation length, which is important for transmitting information.[114] As the cross-sectional diameter decreases, the field confinement increases due to tighter localization of the electromagnetic field, but the propagation length decreases due to an increased fraction of the field being present inside

the metal. For 2D strip waveguides a figure of merit (FOM) was proposed by Buckley et al that accounts for both confinement and propagation length: [115]

$$M_1^{2D} = 2\sqrt{\frac{\pi}{A_e}}L_{prop} \quad (12)$$

The mode area A_e is defined as the area bounded by the closed *1/e* field magnitude contour relative to the electric field maximum, and L_{prop} is the propagation length. The m = 1 mode has a higher FOM than the m = 0 mode for the studied gold nanobelt because the former has a L_{prop} of ~17.5 μm (fitted from Figure 52e), which is about 9 times larger than the m=0 propagation length, while they have comparable mode areas. The calculated figure of merit for m = 1 mode is ~1300, better than those reported for microns wide strip waveguides (~300) at the wavelength of interest (850 nm).[115] The strip waveguides were microns in width, so they have longer plasmon propagation lengths, but lower confinement. Simulations of other subwavelength-sized waveguide architectures at telecom wavelengths have reported maximum figures of merit of ~240 for slot waveguides [116] and ~1000 for gold rectangular waveguides in InGaAsP. [117, 118] The maximum FOM of dielectric-loaded waveguides operating at 780nm has been reported as ~400.[119] Another common definition of figure of merit for nanoscale waveguides is the ratio of the propagation length to the effective mode diameter. This FOM is simply a factor of 4 smaller than the one defined above. Converting these values, our figure of merit exceeds the calculated values for metal-coated hollow nanowires (~800) [120] and silver nanowires exhibiting substrate-coupled modes (~360). [121]

When strong coupling interactions with nearby structures are desired, the mode area is of primary importance. The mode area for the 125 x 40 nm nanobelt is calculated to be

around 2400 nm^2, which is only 48% of its cross-sectional area and is roughly two orders of magnitude smaller than the mode area of the larger strip waveguides. Our calculations also show that a 100 nm diameter cylindrical silver nanowire, as a comparison, has a mode area of around 10,300 nm^2 (131% of its cross-sectional area). The improved strong confinement achieved with gold nanobelts may be useful for studying interactions between plasmons and quantum emitters – bridging the gap between plasmonic and quantum systems.

3.5.6 Spectral Emission Properties

To the spectral properties of the propagating plasmon modes were characterized. The 850 nm LED was replaced by white light from a fiber coupled halogen lamp. A color image of the nanobelt taken in epi-illumination bright field is presented in Figure 57a, which shows a nanobelt with a scattering plasmon resonance near the middle of the visible spectrum (green/yellow). The white light was focused at one end where strong yellow scattering was observed, but the faint emission observed at the opposite end was red, as seen in Figure 57b. The emission was sent through a microspectrometer. The resulting spectra, plotted in Figure 57c, was corrected for the spectral efficiency of the instrument with a 2 μm silver colloid as a white scattering standard. The spectral emission reveals that the plasmon propagation is most efficient in the near infrared, with the majority of the emission beyond a wavelength of 750 nm. The inset to Figure 57c displays the emission spectrum magnified to reveal that there is detectable propagation at visible frequencies and that there is some structure in the spectrum. Note that in the gold nanobelts, a very smooth spectral curve was seen with no evidence of Fabry-Perot fringes

that are often seen in silver nanowires.[56, 107, 108, 110, 112, 122] This may be attributed to the reduced propagation length in these thin gold nanostructures.

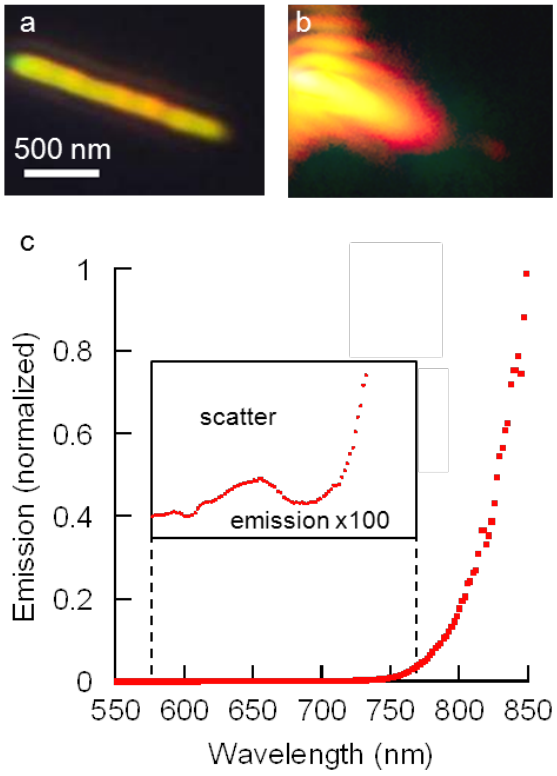

Figure 57 Spectral properties of plasmon propagation in gold nanobelts. A color image a) under wide field white light illumination and b) under propagation c) The emission spectrum strongly favors near infrared wavelengths and the inset displays some structure in the visible.

To compare, the analytical model for cylindrical nanowires was solved as a function of wavelength for three different wire diameters. The result of the calculation, plotted in Figure 58, captures the spectral effect of intrinsic propagation loss, but ignores possible spectral influence of absorption and scattering geometry of the nanobelt ends. Still, given these limitations, the predicted emission spectra are very similar to Figure 57c with a strong increase in propagation efficiency with wavelength, although they do so at shorter wavelengths. The calculations show that the wavelength where the emission rapidly

increases is sensitive to the size, so it is not surprising that it is also apparently sensitive to cross-sectional shape.

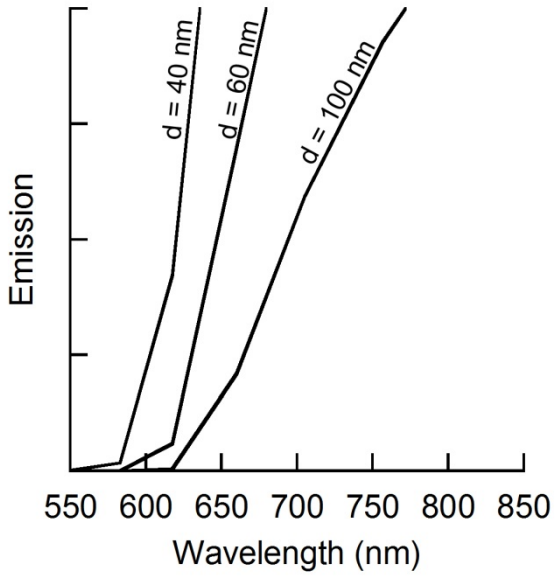

Figure 58 Calculated plasmon propagation spectra for gold nanowires with given diameters.

3.5.7 Conclusion

In summary, plasmon propagation in thin gold nanobelts has been directly observed in gold nanobelts by focusing light at one end and imaging the emission from the other. Problems with imaging short propagation lengths and weak emission signals were overcome through the use of low coherence LED illumination. Propagation was found to be highly efficient in the near-infrared, where gold is minimally lossy. Emission measurements from multiple nanobelts were scaled for different sizes with the scattering signal from the nanobelt excitation end to reveal the average propagation length of the fundamental propagating mode to be 0.94 μm at a wavelength of 850 nm. The propagation was also found to strongly favor near infrared frequencies, agreeing with an analytical model of a cylindrical gold nanowire.

FDTD calculations and experiments show that the measurement is dominated by the fundamental propagating mode, but with increasing nanobelt length, a higher-order mode begins to dominate. This m=1 mode has a propagation length of 17.5 μm and a figure of merit of 1300, the highest reported for nanoscale plasmonic waveguides. The high confinement factor for these structures represent an important step towards studying strong interactions of propagating plasmons with nearby quantum emitters, given the reduced cross-sectional size and the facile surface chemistry of gold nanobelts. Future studies attempting selective mode in-coupling via nearby antennas and photon sources would be of great interest.

.

Conclusion

Nobel metal plasmonic structures have been studied for their properties that may be useful in various medical and information-processing applications. By quantifying individual nanoparticle scattering cross sections in a dark field microscope, it was found that certain nanoparticle geometries scatter very brightly for their volume. This finding may prove valuable in imaging applications that require highly efficient scatterers that can permeate into small spaces.

Novel elongated plasmonic structures, gold nanobelts, have been shown to support a strong and highly tunable transverse standing mode as well as longitudinal propagating modes. The transverse mode is bright and narrow and its peak position varies linearly with the cross-sectional aspect ratio of the nanobelt (width/height). The nanobelts measured have transverse resonances that traverse much of the visible spectrum. Longitudinal plasmons were launched in gold nanobelts using a tightly focused 850nm LED source. The average measured propagation length for these nanobelts is 940nm. For small cross section elongated nanostructures, the fundamental, azimuthally symmetric mode is dominant. It has been found, however, that a higher-order mode exists that decays more slowly and therefore begins to dominate at longer lengths. The polarization of the gold nanobelt emission was characterized and shows this trend, which is supported by FDTD simulations.

Gold nanobelts have the smallest cross section of any elongated plasmonic structure that has been shown to support longitudinal propagating plasmon modes. The m=1 propagating mode has the highest figure of merit reported for a nanoscale plasmonic waveguide. Because of their small size, nanobelts tightly confine electromagnetic energy,

an important step towards strong coupling between plasmonic structures and objects that are small enough to display quantum behaviors.

References

1. Cortie, M. B.; McDonagh, A. M. *Chem Rev* **2011,** 111, (6), 3713-3735.
2. Rycenga, M.; Cobley, C. M.; Zeng, J.; Li, W. Y.; Moran, C. H.; Zhang, Q.; Qin, D.; Xia, Y. *Chem Rev* **2011,** 111, (6), 3669-3712.
3. Maier, S. A.; Atwater, H. A. *Journal of Applied Physics* **2005,** 98, (1), 011101.
4. Halas, N. J.; Lal, S.; Link, S.; Chang, W. S.; Natelson, D.; Hafner, J. H.; Nordlander, P. *Adv. Mater.* **2012,** 24, (36), 4842-4877.
5. Eichelbaum, M.; Rademann, K.; Müller, R.; Radtke, M.; Riesemeier, H.; Görner, W. *Angewandte Chemie International Edition* **2005,** 44, (48), 7905-7909.
6. Liao, H. W.; Nehl, C. L.; Hafner, J. H. *Nanomedicine-Uk* **2006,** 1, (2), 201-208.
7. Hirsch, L. R.; Gobin, A. M.; Lowery, A. R.; Tam, F.; Drezek, R. A.; Halas, N. J.; West, J. L. *Annals Of Biomedical Engineering* **2006,** 34, (1), 15-22.
8. Khlebtsov, N. G.; Dykman, L. A. *Journal of Quantitative Spectroscopy & Radiative Transfer* **2010,** 111, (1), 1-35.
9. Lee, S. E.; Lee, L. P. *Current Opinion in Biotechnology* **2010,** 21, (4), 489-497.
10. Schlücker, S. *ChemPhysChem* **2009,** 10, (9-10), 1344.
11. Golightly, R. S.; Doering, W. E.; Natan, M. J. *Acs Nano* **2009,** 3, (10), 2859-2869.
12. Mayer, K. M.; Hafner, J. H. *Chem Rev* **2011,** 111, (6), 3828-3857.
13. Giannini, V.; Fernandez-Dominguez, A. I.; Heck, S. C.; Maier, S. A. *Chem Rev* **2011,** 111, (6), 3888-3912.
14. Muskens, O. L.; Giannini, V.; Sanchez-Gil, J. A.; Rivas, J. G. *Nano Letters* **2007,** 7, (9), 2871-2875.
15. Link, S.; Mohamed, M.; El-Sayed, M. *Journal of Physical Chemistry B* **1999,** 103, (16), 3073-3077.
16. Klar, T.; Perner, M.; Grosse, S.; von Plessen, G.; Spirkl, W.; Feldmann, J. *Phys Rev Lett* **1998,** 80, (19), 4249-4252.
17. Sonnichsen, C.; Geier, S.; Hecker, N. E.; von Plessen, G.; Feldmann, J.; Ditlbacher, H.; Lamprecht, B.; Krenn, J. R.; Aussenegg, F. R.; Chan, V. Z. H.; Spatz, J. P.; Moller, M. *Applied Physics Letters* **2000,** 77, (19), 2949-2951.
18. Mock, J. J.; Barbic, M.; Smith, D. R.; Schultz, D. A.; Schultz, S. *Journal of Chemical Physics* **2002,** 116, (15), 6755-6759.
19. Sonnichsen, C.; Franzl, T.; Wilk, T.; von Plessen, G.; Feldmann, J. *Phys Rev Lett* **2002,** 88, (7), 077402.
20. Mock, J. J.; Smith, D. R.; Schultz, S. *Nano Letters* **2003,** 3, (4), 485-491.
21. Raschke, G.; Kowarik, S.; Franzl, T.; Sonnichsen, C.; Klar, T. A.; Feldmann, J.; Nichtl, A.; Kurzinger, K. *Nano Letters* **2003,** 3, (7), 935-938.
22. McFarland, A. D.; Van Duyne, R. P. *Nano Letters* **2003,** 3, 1057-1062.
23. Nehl, C.; Grady, N.; Goodrich, G.; Tam, F.; Halas, N.; Hafner, J. *Nano Letters* **2004,** 4, (12), 2355-2359.
24. Sherry, L. J.; Chang, S.-H.; Van Duyne, R. P.; Schatz, G. C.; Wiley, B. J.; Xia, Y. N. *Nano Letters* **2005,** 5, (10), 2034-2038.
25. Nehl, C. L.; Liao, H. W.; Hafner, J. H. *Nano Letters* **2006,** 6, (4), 683-688.

26. Liu, M.; Guyot-Sionnest, P. *Journal of Physical Chemistry B* **2005,** 109, (47), 22192-22200.
27. Markel, V. A.; Shalaev, V. M.; Zhang, P.; Huynh, W.; Tay, L.; Haslett, T. L.; Moskovits, M. *Phys Rev B* **1999,** 59, (16), 10903-10909.
28. Dorfmuller, J.; Vogelgesang, R.; Weitz, R. T.; Rockstuhl, C.; Etrich, C.; Pertsch, T.; Lederer, F.; Kern, K. *Nano Letters* **2009,** 9, (6), 2372-2377.
29. Schaffer, B.; Hohenester, U.; Trugler, A.; Hofer, F. *Phys Rev B* **2009,** 79, (4), -.
30. Eggeman, A. S.; Dobson, P. J.; Petford-Long, A. K. *Journal of Applied Physics* **2007,** 101, (2), -.
31. Gomez-Medina, R.; Yamamoto, N.; Nakano, M.; Abajo, F. J. G. *New Journal of Physics* **2008,** 10, -.
32. van Wijngaarden, J. T.; Verhagen, E.; Polman, A.; Ross, C. E.; Lezec, H. J.; Atwater, H. A. *Applied Physics Letters* **2006,** 88, (22), -.
33. Anker, J. N.; Hall, W. P.; Lyandres, O.; Shah, N. C.; Zhao, J.; Van Duyne, R. P. *Nature Materials* **2008,** 7, (6), 442-453.
34. Murphy, C. J.; Gole, A. M.; Stone, J. W.; Sisco, P. N.; Alkilany, A. M.; Goldsmith, E. C.; Baxter, S. C. *Accounts of Chemical Research* **2008,** 41, (12), 1721-1730.
35. Lal, S.; Link, S.; Halas, N. J. *Nature Photonics* **2007,** 1, (11), 641-648.
36. Steinberger, B.; Hohenau, A.; Ditlbacher, H.; Stepanov, A. L.; Drezet, A.; Aussenegg, F. R.; Leitner, A.; Krenn, J. R. *Applied Physics Letters* **2006,** 88, (9), 094104.
37. Bouhelier, A.; Huser, T.; Tamaru, H.; Guntherodt, H. J.; Pohl, D. W.; Baida, F. I.; Van Labeke, D. *Phys Rev B* **2001,** 63, (15), 155404.
38. Barnes, W. L.; Dereux, A.; Ebbesen, T. W. *Nature* **2003,** 424, (6950), 824-830.
39. Ditlbacher, H.; Krenn, J. R.; Hohenau, A.; Leitner, A.; Aussenegg, F. R. *Applied Physics Letters* **2003,** 83, (18), 3665.
40. Wang, C.-J.; Lin, L. Y. *Nanoscale Research Letters* **2007,** 2, (5), 219.
41. Halas, N. J.; Lal, S.; Chang, W. S.; Link, S.; Nordlander, P. *Chem Rev* **2011,** 111, (6), 3913-3961.
42. Dickson, R. M.; Lyon, L. A. *Journal of Physical Chemistry B* **2000,** 104, (26), 6095-6098.
43. Knight, M. W.; Grady, N. K.; Bardhan, R.; Hao, F.; Nordlander, P.; Halas, N. J. *Nano Letters* **2007,** 7, (8), 2346-2350.
44. Gray, S. K.; Kupka, T. *Phys Rev B* **2003,** 68, (4), 045415.
45. Rybczynski, J.; Kempa, K.; Herczynski, A.; Wang, Y.; Naughton, M. J.; Ren, Z. F.; Huang, Z. P.; Cai, D.; Giersig, M. *Applied Physics Letters* **2007,** 90, (2), 021104-3.
46. Krenn, J. R.; Weeber, J.-C. *Philosophical Transactions of the Royal Society of London. Series A: Mathematical, Physical and Engineering Sciences* **2004,** 362, (1817), 739-756.
47. Sanders, A. W.; Routenberg, D. A.; Wiley, B. J.; Xia, Y.; Dufresne, E. R.; Reed, M. A. *Nano Letters* **2006,** 6, (8), 1822-1826.
48. Li, Z. P.; Hao, F.; Huang, Y. Z.; Fang, Y. R.; Nordlander, P.; Xu, H. X. *Nano Letters* **2009,** 9, (12), 4383-4386.
49. Veronis, G.; Fan, S. *Applied Physics Letters* **2005,** 87, (13), 131102.
50. Chang, D. E.; Sorensen, A. S.; Hemmer, P. R.; Lukin, M. D. *Phys Rev Lett* **2006,** 97, (5), 053002.

51. Chang, D. E.; Sorensen, A. S.; Demler, E. A.; Lukin, M. D. *Nat Phys* **2007,** 3, (11), 807-812.
52. Liu, M. Z.; Lee, T. W.; Gray, S. K.; Guyot-Sionnest, P.; Pelton, M. *Phys Rev Lett* **2009,** 102, (10), 107401.
53. Akimov, A. V.; Mukherjee, A.; Yu, C. L.; Chang, D. E.; Zibrov, A. S.; Hemmer, P. R.; Park, H.; Lukin, M. D. *Nature* **2007,** 450, (7168), 402-406.
54. Fedutik, Y.; Temnov, V. V.; Schops, O.; Woggon, U.; Artemyev, M. V. *Phys Rev Lett* **2007,** 99, (13), 136802.
55. Chang, D. E.; Sorensen, A. S.; Hemmer, P. R.; Lukin, M. D. *Phys Rev B* **2007,** 76, (3), 035420.
56. Ditlbacher, H.; Hohenau, A.; Wagner, D.; Kreibig, U.; Rogers, M.; Hofer, F.; Aussenegg, F. R.; Krenn, J. R. *Phys Rev Lett* **2005,** 95, (25), 257403.
57. Solis, D.; Chang, W.-S.; Khanal, B. P.; Bao, K.; Nordlander, P.; Zubarev, E. R.; Link, S. *Nano Letters* **2010,** 10, (9), 3482-3485.
58. Bohren, C. F.; Huffman, D. R., *Absorption and Scattering of Light by Small Particles*. 2 ed.; Wiley-Interscience: 1998; p 544.
59. Liao, H. W.; Hafner, J. H. *Chem. Mat.* **2005,** 17, (18), 4636-4641.
60. Orendorff, C. J.; Murphy, C. J. *Journal of Physical Chemistry B* **2006,** ASAP.
61. Chen, Y.; Munechika, K.; Plante, I. J. L.; Munro, A. M.; Skrabalak, S. E.; Xia, Y.; Ginger, D. S. *Applied Physics Letters* **2008,** 93, (5), -.
62. Chen, Y.; Munechika, K.; Ginger, D. S. *Nano Letters* **2007,** 7, (3), 690-696.
63. Schultz, S.; Smith, D. R.; Mock, J. J.; Schultz, D. A. *Proceedings of the National Academy of Sciences of the United States of America* **2000,** 97, (3), 996-1001.
64. Link, S.; El-Sayed, M. A. *Int Rev Phys Chem* **2000,** 19, (3), 409-453.
65. Encina, E. R.; Coronado, E. A. *The Journal of Physical Chemistry C* **2008,** 112, (26), 9586-9594.
66. Jain, P. K.; Lee, K. S.; El-Sayed, I. H.; El-Sayed, M. A. *Journal of Physical Chemistry B* **2006,** 110, (14), 7238-7248.
67. Ni, W.; Kou, X.; Yang, Z.; Wang, J. F. *Acs Nano* **2008,** 2, (4), 677-686.
68. Papavissiou, G. C. *Progess in Solid State Chemistry* **1979,** 12, (3-4), 185-271.
69. Asano, S.; Yamamoto, G. *Applied Optics* **1975,** 14, (1), 29-49.
70. Le, Q.; Larson, T. A.; Smith, D. K.; Vitkin, E.; Songhua, Z.; Modell, M. D.; Itzkan, I.; Hanlon, E. B.; Korgel, B. A.; Sokolov, K. V.; Perelman, L. T. *Selected Topics in Quantum Electronics, IEEE Journal of* **2007,** 13, (6), 1730.
71. Bryant, G. W.; De Abajo, F. J. G.; Aizpurua, J. *Nano Letters* **2008,** 8, (2), 631-636.
72. Knight, M. W.; Wu, Y. P.; Lassiter, J. B.; Nordlander, P.; Halas, N. J. *Nano Letters* **2009,** 9, (5), 2188-2192.
73. Rostro, B. C.; Bickford, L.; Hafner, J. H. *Nanotechnology* **2009,** In press.
74. Zuchner, T.; Wackenhut, F.; Failla, A. V.; Meixner, A. J. *Applied Surface Science* **2009,** 255, (10), 5391-5395.
75. Javier, D. J.; Nitin, N.; Roblyer, D. M.; Richards-Kortum, R. *Journal of Nanophotonics* **2008,** 2, -.
76. Zhao, N.; Wei, Y.; Sun, N. J.; Chen, Q. J.; Bai, J. W.; Zhou, L. P.; Qin, Y.; Li, M. X.; Qi, L. M. *Langmuir* **2008,** 24, (3), 991-998.

77. Payne, E. K.; Shuford, K. L.; Park, S.; Schatz, G. C.; Mirkin, C. A. *Journal of Physical Chemistry B* **2006,** 110, (5), 2150-2154.
78. Johnson, P. B.; Christy, R. W. *Phys Rev B* **1972,** 6, (12), 4370-4379.
79. Berenger, J. P. *J Comput Phys* **1994,** 114, (2), 185-200.
80. Zhang, S. P.; Wei, H.; Bao, K.; Hakanson, U.; Halas, N. J.; Nordlander, P.; Xu, H. X. *Phys Rev Lett* **2011,** 107, (9), 096801.
81. Brioude, A.; Jiang, X. C.; Pileni, M. P. *Journal of Physical Chemistry B* **2005,** 109, (27), 13138-13142.
82. Anderson, L. J. E.; Payne, C. M.; Zhen, Y.; Nordlander, P.; Hafner, J. H. *Nano Letters* **2011,** ASAP.
83. Thomas, K. G.; Kamat, P. V. *Accounts of Chemical Research* **2003,** 36, (12), 888-898.
84. Ming, T.; Chen, H.; Jiang, R.; Li, Q.; Wang, J. *The Journal of Physical Chemistry Letters* **2012,** 3, (2), 191.
85. Dulkeith, E.; Morteani, A. C.; Niedereichholz, T.; Klar, T. A.; Feldmann, J.; Levi, S. A.; van Veggel, F. C. J. M.; Reinhoudt, D. N.; M√∂ller, M.; Gittins, D. I. *Phys Rev Lett* **2002,** 89, (20), 203002.
86. Munechika, K.; Chen, Y.; Tillack, A. F.; Kulkarni, A. P.; Plante, I. J.-L.; Munro, A. M.; Ginger, D. S. *Nano Letters* **2010,** 10, (7), 2598.
87. Bharadwaj, P.; Novotny, L. *Opt. Express* **2007,** 15, (21), 14266-14274.
88. Chen, C.-T.; Liu, C.-C.; Wang, C.-H.; Chen, C.-W.; Chen, Y.-F. *Applied Physics Letters* **2011,** 98, (26), 261918-261918-3.
89. Ming, T.; Zhao, L.; Chen, H.; Woo, K. C.; Wang, J.; Lin, H.-Q. *Nano Letters* **2011,** 11, (6), 2296-2303.
90. Tam, F.; Goodrich, G. P.; Johnson, B. R.; Halas, N. J. *Nano Letters* **2007,** 7, (2), 496-501.
91. Coe, S.; Woo, W. K.; Bawendi, M.; Bulovic, V. *Nature* **2002,** 420, (6917), 800-803.
92. Prodan, E.; Radloff, C.; Halas, N. J.; Nordlander, P. *Science* **2003,** 302, (5644), 419-422.
93. Maier, S. A.; Brongersma, M. L.; Kik, P. G.; Meltzer, S.; Requicha, A. A. G.; Atwater, H. A. *Adv. Mater.* **2001,** 13, (19), 1501-5105.
94. Dionne, J. A.; Sweatlock, L. A.; Atwater, H. A.; Polman, A. *Phys Rev B* **2006,** 73, (3), 035407.
95. Dionne, J. A.; Lezec, H. J.; Atwater, H. A. *Nano Letters* **2006,** 6, (9), 1928-1932.
96. Lee, S.; Anderson, L. J. E.; Payne, C. M.; Hafner, J. H. *Langmuir* **2011,** 27, (24), 14748-14756.
97. Le Ru, E. C.; Meyer, M.; Blackie, E.; Etchegoin, P. G. *Journal of Raman Spectroscopy* **2008,** 39, (9), 1127-1134.
98. Sackmann, M.; Materny, A. *Journal of Raman Spectroscopy* **2006,** 37, (1-3), 305-310.
99. Krenn, J. R.; Lamprecht, B.; Ditlbacher, H.; Schider, G.; Salerno, M.; Leitner, A.; Aussenegg, F. R. *Europhysics Letters* **2002,** 60, (5), 663.
100. Jacob, Z.; Shalaev, V. M. *Science* **2011,** 334, (6055), 463-464.
101. Kolesov, R.; Grotz, B.; Balasubramanian, G.; Stohr, R. J.; Nicolet, A. A. L.; Hemmer, P. R.; Jelezko, F.; Wrachtrup, J. *Nat Phys* **2009,** 5, (7), 470-474.

102. Fasel, S.; Robin, F.; Moreno, E.; Erni, D.; Gisin, N.; Zbinden, H. *Phys Rev Lett* **2005,** 94, (14).
103. Huck, A.; Smolka, S.; Lodahl, P.; Sorensen, A. S.; Boltasseva, A.; Janousek, J.; Andersen, U. L. *Phys Rev Lett* **2009,** 102, (24).
104. Bracher, G.; Schraml, K.; Jakubeit, C.; Kaniber, M.; Finley, J. J. *Journal of Applied Physics* **2011,** 110, (12), 123106.
105. Kusar, P.; Gruber, C.; Hohenau, A.; Krenn, J. R. *Nano Letters* **2012,** 12, (2), 661-665.
106. Paul, A.; Solis, D.; Bao, K.; Chang, W.-S.; Nauert, S.; Vidgerman, L.; Zubarev, E.; Nordlander, P.; Link, S. *Acs Nano* **2012,** asap.
107. Wild, B.; Cao, L. N.; Sun, Y. G.; Khanal, B. P.; Zubarev, E. R.; Gray, S. K.; Scherer, N. F.; Pelton, M. *Acs Nano* **2012,** 6, (1), 472-482.
108. Allione, M.; Temnov, V. V.; Fedutik, Y.; Woggon, U.; Artemyev, M. V. *Nano Letters* **2007,** 8, (1), 31.
109. Li, Z. P.; Bao, K.; Fang, Y. R.; Guan, Z. Q.; Halas, N. J.; Nordlander, P.; Xu, H. X. *Phys Rev B* **2010,** 82, (24).
110. Rewitz, C.; Keitzl, T.; Tuchscherer, P.; Goetz, S.; Geisler, P.; Razinskas, G.; Hecht, B.; Brixner, T. *Opt. Express* **2011,** 20, (13), 14632.
111. Wei, H.; Li, Z. P.; Tian, X. R.; Wang, Z. X.; Cong, F. Z.; Liu, N.; Zhang, S. P.; Nordlander, P.; Halas, N. J.; Xu, H. X. *Nano Letters* **2011,** 11, (2), 471-475.
112. Hohenau, A.; Kusar, P.; Gruber, C.; Krenn, J. R. *Opt. Lett.* **2012,** 37, (4), 746.
113. Coskun, S.; Aksoy, B.; Unalan, H. E. *Cryst Growth Des* **2011,** 11, (11), 4963-4969.
114. Oulton, R. F.; Bartal, G.; Pile, D. F. P.; Zhang, X. *New Journal of Physics* **2008,** 10, (10), 105018.
115. Buckley, R.; Berini, P. *Opt. Express* **2007,** 15, (19), 12174-12182.
116. Lee, K.-S.; Jung, J.-H. *J. Opt. Soc. Korea* **2011,** 15, (3), 305-309.
117. Krasavin, A. V.; Zayats, A. V. *Opt. Lett.* **2010,** 35, (13), 2118-2120.
118. Krasavin, A. V.; Zayats, A. V. *Opt. Lett.* **2011,** 36, (16), 3127-3129.
119. Grandidier, J.; Massenot, S.; des Francs, G. C.; Bouhelier, A.; Weeber, J. C.; Markey, L.; Dereux, A.; Renger, J.; González, M. U.; Quidant, R. *Phys Rev B* **2008,** 78, (24), 245419.
120. Yalin, S.; Zheng, Z.; Yusheng, B.; Lei, L.; Xin, Z.; Jiansheng, L.; Tao, Z.; Shize, G.; Wei, N.; Yulong, L.; Jinsong, Z. *Journal of Optics* **2012,** 14, (9), 095501.
121. Zhang, S.; Xu, H. *ACS Nano* **2012,** 6, (9), 8128-8135.
122. Shegai, T.; Miljkovic, V. D.; Bao, K.; Xu, H. X.; Nordlander, P.; Johansson, P.; Kall, M. *Nano Letters* **2011,** 11, (2), 706-711.

Appendix

Appendix A: Matlab Code, Mie Solution

Calculating σ_{tot} and σ_{obj}

```
clear
%input nanosphere radius
din=input('diameter in nm? ','s');
%radius=diameter/2
rad=str2num(din)/2;
r=rad*1e-9;
load gold_diel2
nm=1.515;
n=gold_dielectric2(:,2);
k=gold_dielectric2(:,3);
%input angular detection range
%minimum detection angle (radians)
thetaMin=3.2909;
%maximum detection angle (radians)
thetaMax=3.9635;
%phi range = theta range
phi=thetaMax-thetaMin;
for t=1:600;
        w(t)=t+400;
        m=(n(t)+i*k(t))/nm; %ratio of indecies of refraction particle/medium
        l=t+400; %wavelegth (nm)
        kn=(2*pi*nm)/(l*10^(-9)); %wavenumber
        x=kn*r;
        %getting "a" and "b" (L is the multipole order)
        for L=1:9
                psix=sqrt((pi*x)/2)*besselj(L+(1/2),x);
                psix2=sqrt(pi/2)*(((L+1)/sqrt(x))*besselj(L+(1/2),x)-
        (sqrt(x)*besselj(L+(3/2),x)));
                psimx=sqrt(pi*m*x/2)*besselj(L+(1/2),m*x);
                psimx2=sqrt(pi/2)*(((L+1)/sqrt(m*x))*besselj(L+(1/2),m*x)-
                (sqrt(m*x)*besselj(L+(3/2),m*x)));
                ksix=sqrt(pi*x/2)*besselh(L+(1/2),x);
                ksix2=sqrt(pi/2)*(((L+1)/sqrt(x))*besselh(L+(1/2),x)-
        (sqrt(x)*besselh(L+(3/2),x)));
                ksimx=sqrt(pi*m*x/2)*besselh(L+(1/2),m*x);
                ksimx2=sqrt(pi/2)*(((L+1)/sqrt(m*x))*besselh(L+(1/2),m*x)-
                (sqrt(m*x)*besselh(L+(3/2),m*x)));
                a(L)=(m*psimx*psix2-psix*psimx2)/(m*psimx*ksix2-ksix*psimx2);
                b(L)=(psimx*psix2-m*psix*psimx2)/(psimx*ksix2-m*ksix*psimx2);
```

```
S(L)=(2*pi/(kn^2))*(2*L+1)*(abs(a(L))*(abs(a(L)))+(abs(b(L)))*(abs(b(L))));
        end %end L-loop

        %total scattering cross section:
        scaap(t)=(S(1)+S(2)+S(3)+S(4)+S(5)+S(6)+S(7)+S(8)+S(9));
        %Find peak amplitude of scattering to the objective:
        MaxTotal=max(scaap);

        %angular loop
        dTheta = .0001;
        numSteps=(thetaMax-thetaMin)/dTheta;
        clear theSum;
        theSum = 0;
        for ii=1:numSteps;
                theta = thetaMin + ii*dTheta;
                %Calculate the scattering parameters tau and pi
                %initial conditions on pi
                pi1=1;
                pi2=3*cos(theta);
                pi3=(5/2)*cos(theta)*pi2-(3/2)*pi1;
                pi4=(7/3)*cos(theta)*pi3-(4/3)*pi2;
                pi5=(9/4)*cos(theta)*pi4-(5/4)*pi3;
                pi6=(11/5)*cos(theta)*pi5-(6/5)*pi4;
                pi7=(13/6)*cos(theta)*pi6-(7/6)*pi5;

                tau1=cos(theta);
                tau2=6*(cos(theta)*cos(theta))-3;
                tau3=3*cos(theta)*pi3-4*pi2;
                tau4=4*cos(theta)*pi4-5*pi3;
                tau5=5*cos(theta)*pi5-6*pi4;
                tau6=6*cos(theta)*pi6-7*pi5;

                %some scattering parameters that depend on tau, pi, a and b
                S101=(3/2)*(a(1)*pi1+b(1)*tau1);
                S102=(5/6)*(a(2)*pi2+b(2)*tau2);
                S103=(7/12)*(a(3)*pi3+b(3)*tau3);
                S104=(9/20)*(a(4)*pi4+b(4)*tau4);
                S105=(11/30)*(a(5)*pi5+b(5)*tau5);
                S106=(13/42)*(a(6)*pi6+b(6)*tau6);
                S1=S101+S102+S103+S104+S105+S106; %sum of 6 terms above

                S201=(3/2)*(a(1)*tau1+b(1)*pi1);
                S202=(5/6)*(a(2)*tau2+b(2)*pi2);
                S203=(7/12)*(a(3)*tau3+b(3)*pi3);
                S204=(9/20)*(a(4)*tau4+b(4)*pi4);
```

```
                S205=(11/30)*(a(5)*tau5+b(5)*pi5);
                S206=(13/42)*(a(6)*tau6+b(6)*pi6);
                S2=S201+S202+S203+S204+S205+S206; %sum of 6 terms above


                S11=.5*(abs(S2)*abs(S2)+abs(S1)*abs(S1));
                ds_dt=S11/(kn*kn);

                theSum = theSum + abs(ds_dt*sin(theta)) * dTheta;

        end
        %Scattering cross section for wavelength t over the solid angle of the
        %detector:
        scatter(t)=phi*theSum;
end

%Find peak amplitude of scattering to the objective:
MaxDiff=max(scatter);

%Find peak wavelength:
temporary=scatter;
for ii=1:600
      if MaxDiff==temporary(ii)
         peakpsc=ii;
      end
   end
peak_wavelength_sc=peakpsc+400;
```

Appendix B: Matlab Code, Approximations to Mie Solution

Comparing σ_{tot} (dipole term only, small particle approximation, Gans solution)

```
clear
%Calculate the extinction, absorption, and scattering from a gold sphere or
%ellipsoid using Mie or Gans theory (Gan's is in the small particle limit).
load gold_diel
n2=input('Medium index of refraction (n)?','s');
nm=str2num(n2);
em=nm^2;
type=input('Would you like to model a sphere or an ellipsoid? (sphere=0,
ellipsoid=1):','s');
model=str2num(type);

%sphere
if model==0
   rad=input('Sphere radius (in nm): ','s');
   rd=str2num(rad);
   r=rd*10^(-9);  %nanoparticle radius in nanometers
   small=input('Is ka<<1? (yes(1) or no(0)): ');

%Full Mie expression
   if small==0
      for P=1:10
         for t=1:2400
            l=(.25)*t+400;
            n=gold_dielectric(:,2);
            k=gold_dielectric(:,3);
            m=(n(t)+i*k(t))/nm;
            kn=(2*pi*nm)/(l*10^(-9));
            x=kn*r;
            psix=sqrt((pi*x)/2)*besselj(P+(1/2),x);
            psix2=sqrt(pi/2)*(((P+1)/sqrt(x))*besselj(P+(1/2),x)-
(sqrt(x)*besselj(P+(3/2),x)));
            psimx=sqrt(pi*m*x/2)*besselj(P+(1/2),m*x);
            psimx2=sqrt(pi/2)*(((P+1)/sqrt(m*x))*besselj(P+(1/2),m*x)-
         (sqrt(m*x)*besselj(P+(3/2),m*x)));
            ksix=sqrt(pi*x/2)*besselh(P+(1/2),x);
            ksix2=sqrt(pi/2)*(((P+1)/sqrt(x))*besselh(P+(1/2),x)-
(sqrt(x)*besselh(P+(3/2),x)));
            ksimx=sqrt(pi*m*x/2)*besselh(P+(1/2),m*x);
             ksimx2=sqrt(pi/2)*(((P+1)/sqrt(m*x))*besselh(P+(1/2),m*x)-
         (sqrt(m*x)*besselh(P+(3/2),m*x)));
            a=(m*psimx*psix2-psix*psimx2)/(m*psimx*ksix2-ksix*psimx2);
            b=(psimx*psix2-m*psix*psimx2)/(psimx*ksix2-m*ksix*psimx2);
```

```
            S(P,t)=(2*pi/(kn^2))*(2*P+1)*((abs(a))^2+(abs(b))^2);
            E(P,t)=(2*pi/(kn^2))*(2*P+1)*real(a+b);
            w(t)=(.25)*t+399;
         end %end t-loop
      end %end P-loop
      scaap=(S(1,:)+S(2,:)+S(3,:)+S(4,:)+S(5,:)+S(6,:)+S(7,:)+S(8,:)+S(9,:)+S(10,:));
      extap=(E(1,:)+E(2,:)+E(3,:)+E(4,:)+E(5,:)+E(6,:)+E(7,:)+E(8,:)+E(9,:)+E(10,:));
      absap(t)=extap(t)-scaap(t);
   end %end if small==0

%Small particle approximation
   if small==1
      for t = 1:2400
         n=gold_dielectric(:,2);
         k=gold_dielectric(:,3);
         ep(t)=n(t)*n(t)-k(t)*k(t);
         epp(t)=2*n(t)*k(t);
         lambda(t)=((.25)*t+400)*10^(-9);
         scoeff(t)=(128*pi*pi*pi*pi*pi*em*em*r*r*r*r*r*r)/(3*(lambda(t)^4));
         ecoeff(t)=(24*pi*pi*r*r*r*(em^(3/2)))/lambda(t);
         scaap(t)=scoeff(t)*(((ep(t)-em)*(ep(t)-
         em))+(epp(t)*epp(t)))/(((ep(t)+2*em)*(ep(t)+2*em))+ (epp(t)*epp(t)));

         extap(t)=ecoeff(t)*(epp(t)/(((ep(t)+2*em)*(ep(t)+2*em))+(epp(t)*epp(t))));

         absap(t)=extap(t)-scaap(t);

         w(t)=(.25)*t+399;
      end %end t-loop
    end %end if small==1
end %end if model=0


if model==1
   maj=input('Major radius (in nm): ','s');
   a0 = str2num(maj);
   min=input('Minor radius (in nm): ','s');
   a1 = str2num(min);
   a=a0*10^(-9);  %nanoparticle major radius in nanometers
   b=a1*10^(-9);  %nanoparticle minor radius in nanometers
   V=4*pi*a*b*b/3;
   eccen=sqrt(1-(b/a)^2);
   Pa=(1/eccen^2 -1)*((1/(2*eccen))*(log((1+eccen)/(1-eccen)))-1);
   Pb=(1-Pa)/2;
   Pc=Pb;
```

```
    for L = 1:3
        for t = 1:2400
            n=gold_dielectric(:,2);
            k=gold_dielectric(:,3);
            ep(t)=n(t)*n(t)-k(t)*k(t);
            epp(t)=2*n(t)*k(t);
            lambda=(.25)*t+400;
            extap(t)=10^9*18*pi*(em)^(3/2)*V*(1/Pa^2)*epp(t)/(lambda*((ep(t)+(1/Pa -
            1)*em)^2+(epp(t))^2))   +
            10^9*18*pi*(em)^(3/2)*V*(1/Pb^2)*epp(t)/(lambda*((ep(t)+(1/Pb -
            1)*em)^2+(epp(t))^2))  +
            10^9*18*pi*(em)^(3/2)*V*(1/Pc^2)*epp(t)/(lambda*((ep(t)+(1/Pc -
            1)*em)^2+(epp(t))^2));
            scaap(t)=10^36*8*pi^3*em^2*V^2*(1/Pa^2)*((ep(t)-
em)^2+(epp(t))^2)/(3*lambda^4*((ep(t)+(1/Pa-1)*em)^2+(epp(t))^2))   +
10^36*8*pi^3*em^2*V^2*(1/Pb^2)*((ep(t)-
em)^2+(epp(t))^2)/(3*lambda^4*((ep(t)+(1/Pb-1)*em)^2+(epp(t))^2))  +
10^36*8*pi^3*em^2*V^2*(1/Pc^2)*((ep(t)-
em)^2+(epp(t))^2)/(3*lambda^4*((ep(t)+(1/Pc-1)*em)^2+(epp(t))^2));
            absap(t)=extap(t)-scaap(t);
            w(t)=(.25)*t+400;
        end %end t-loop
    end %end L-loop
end %end model=1

%Find the peak height and peak wavelength
Maximum=max(scaap);
temporary=scaap;
for ii=1:2400
    if Maximum==temporary(ii)
      peakp=ii;
    end
end
```

Appendix C: Matlab Code, Spectral Analysis and Calculation of K

Analyzing Spectra and Calculating K_λ

```
clear

load Mie; %load angular mie result
load std; %load spectral wavelength values

%Create wavelength values 400-1000nm
for t=1:600
   w(t)=t+400;
end

%Analyze spectral data:

%Find the file and save the filename and path
[file,path]=uigetfile('*','Select the image to analyze');

%Load the image
ve = imread([path,file],'tiff');

%convert integers to floating point numbers
ve = double(ve);

%flip the image upside down so orientation appears same as original
for i = 1:512
   for j = 1:512
         vd(i,j)=ve(513-i,j);
   end
end
%Plot the image to specify particle location and width
   figure
   drawnow
   pcolor(vd)
   shading interp

st = input('Based on the image, enter the pixel of the spectrum center:  ','s');
center=str2num(st);

st1 = input('What width (in pixels) do you want to sum over?  ','s');
 width = str2num(st1);

dt =input('What is the integration time of the image? ','s');
 time=str2num(dt);
```

```
%isolate data in this range (where the particle is)
v1raw=vd(:,(center-width):(center+width));
%sum the sqrt of the data in this range to get the error for each
%wavelength
for i = 1:512
   error(i)=sum(sqrt(vd(i,center-width:center+width))/(time));
end


%create x-axis: spatial values
x=1:512;
x((center-width):(center+width))=[];
%subtract particle out of data (for bkg fit)
vd(:,(center-width):(center+width))=[];
plot(x,vd(:,:))

%choose range to fit background (in pixel values)
 rl=input('Lower bound on background fit? ','s');
  range1 = str2num(rl);
 ru=input('Upper bound on background fit? ','s');
  range2=str2num(ru);

for ii=1:(512-((2*width)+1))
   if x(ii)==range1
      r1=ii;
   end
   if x(ii)==range2
      r2=ii;
   end
end %end ii-loop
 vd=vd(:,(r1+1):(r2-1));
 %Take out edges and change the x-axis accordingly
 x(r2:(512-((2*width)+1)))=[];
 x(1:r1)=[];

N=input('What order polynomial would you like to fit the background to?' );

for i=1:512%(each wavelength)
   drawnow
   plot(x,vd(i,:))
   hold on
   %for each wavelength, fit a curve to vd(signal-paricle) as a function of
   %space
   P=polyfit(x,vd(i,:),N);
   for ii=1:(r2-1-r1)%each spatial value
      %Nth order
```

```
        for j=1:N+1
            vb2(j)=P(j)*x(ii)^(N-(j-1));
        end %j-loop
        %The background as a function of spatial pixel values. (there is one of
        %these for each wavelength
        vb(i,ii)=sum(vb2);
    end %ii-loop
    %extend vb to include the center (actually, entire spatial axis)
    for jj=1:512
        for j=1:N+1
            back(j)=P(j)*(jj)^(N-(j-1));
        end
        bkg(i,jj)=sum(back);
    end %jj-loop

    plot(x,vb(i,:))
    hold off
end %i-loop

    bkgd=(bkg(:,center-width:center+width));

for i=1:512
    for j=1:2*width+1
        tot(i,j)=v1raw(i,j)-bkgd(i,j);
    end
    v1(i)=sum(tot(i,:))/(time);
end

v1=v1';
Maxv1=max(v1);
newv1=interp1(spswavelengths,v1,w);
newerv1=(1/1.945)*newv1;
newerv1=newerv1';

%Solve for K
for i=1:600
    K(i)=newerv1(i)/scatter(i);
end

error=error';
plot(spswavelengths,v1)
plot(w,K)
K=K';
```

Appendix D: COMSOL Multiphysics Simultation

Gold nanobelt dimers were simulated using the commercially available software package, COMSOL. This software uses the widely known Finite Element Method, which finds numerical solutions to partial differential equations (in this case, the equations of electrodynamics). The method relies on dividing up the simulation space into small pieces and solving the equations in each of these elements in relation to one another. The solutions of a PDE are approximated by solutions to an ODE in the time-varying case, and an algebraic equation in the steady-state case. This is vast a simplification over solving the complex problem everywhere in the simulation space, and is known to give accurate answers.

For the simulation of two parallel gold nanobelts, it is sufficient to do a 2D cross section of the actual 3D problem, and is actually superior to a 3D simulation. The full 3D simulation is very computationally expensive, and does not realistically allow for microns-long nanobelt lengths given the computational limits. This leaves the option of simulating nanobelts that are shorter than the experimental nanobelts, say a few microns or less. This poses problems because, at this length scale, standing plasmon modes can form longitudinally, resulting in a longitudinal resonance, which is not true in the experimental case; in reality, the nanobelts are too long for a standing longitudinal resonance to form. The 2D simulation solves this problem perfectly because a 2D cross section treats the belts as infinite, which they essentially are, in comparison to their cross-sectional dimensions.

Opening the COMSOL Multiphysics package, the user is presented with a Model Navigator window (Figure 59). Under “Space Dimension”, 2D should be selected from

the drop-down box. For electrostatics problems, the RF module is used. We are interested in an incident plane wave that is normal to the nanobelt dimer and polarized perpendicular to the belts (across the gap). We will choose the "Perpendicular Waves" module, and under that, "TM waves" (Figure 59).

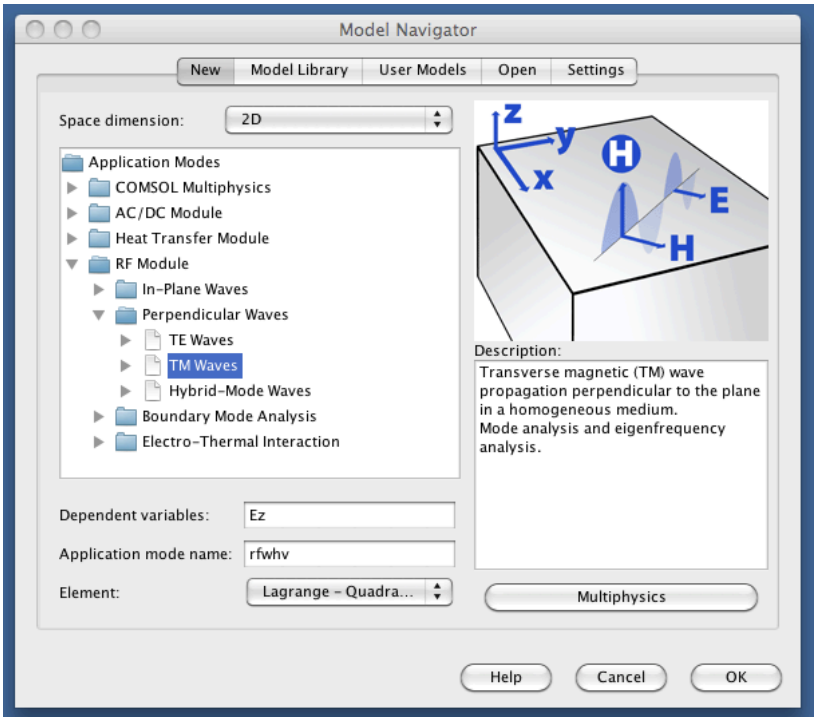

Figure 59 Model Navigator in COMSOL Multiphysics.

Upon clicking "OK", the COMSOL Module will open. First, we want to create all of the geometric objects, this will include the nanobelts, the simulation space and a "perfectly matched layer" (PML). The PML is an artificial absorbing layer that is commonly used in wave simulations with open boundaries to eliminate reflections at the imposed boundary. For adding geometry, we want to be in "Draw Mode". There should be a button with a small pencil: , once pressed the user is in this mode. There will be a number of drawing tools, for which the placement may vary depending on the software

version and operating system. To create the rectangular nanobelt cross sections, we will click the rectangle button ( ). By dragging the cursor in the simulation space, we will get a rectangle whose properties can be manipulated by going to Draw -> Object Properties. For the simulation results shown in Section 3.4, the nanobelt size was 50nm x 20nm. To have the dimer gap in the center of the simulation space, we also shift the first belt position (

Figure 60). Note that the "zoom extents" button will zoom to make the current geometric objects fill up the field of view.

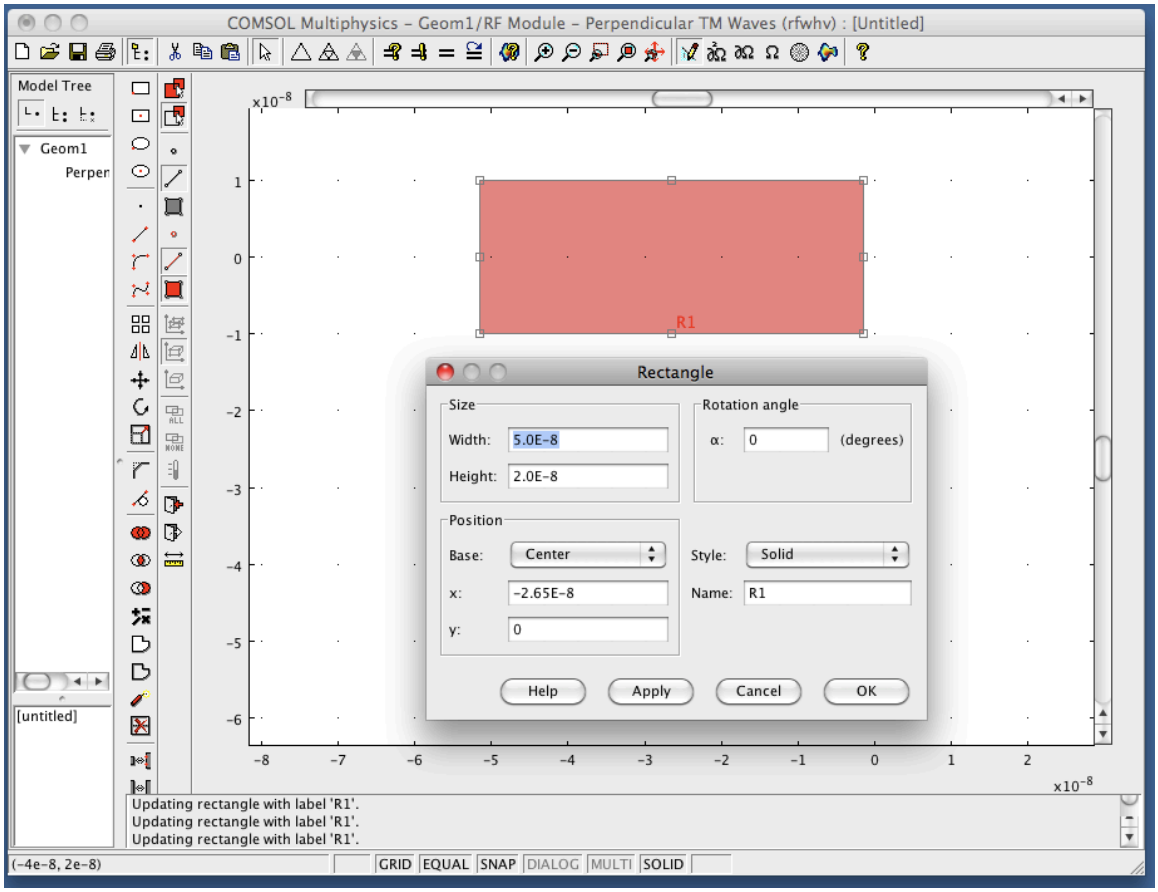

Figure 60 Specifying the nanobelt geometry in COMSOL.

We repeat the last step to make the second nanobelt, with the only difference being in the position. The x coordinate of the rectangle bases should be at ±(nanobelt width + gap size)/2.

The FEM method has difficulty solving in domains with sharp corners – which are also not realistic. We therefore, give the nanobelt corners a slight curvature. To do this, we click the "Fillet/Chamfer" button in Draw Mode:  . The pop-up window will give all corners in the simulation, which at this point are the nanobelt corners. They should all be selected and a small, realistic radius of curvature should be specified, in this case, we chose 2nm (

Figure 61).

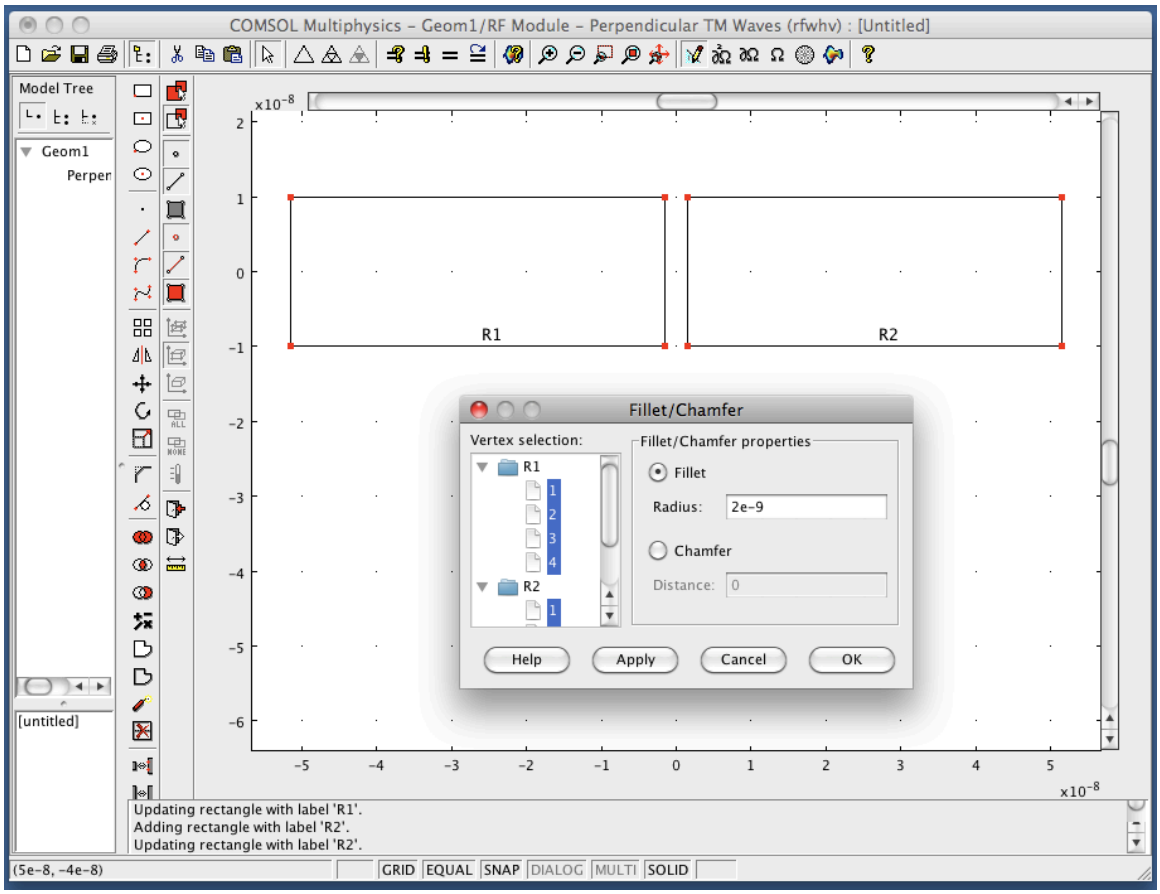

Figure 61 Rounding the nanobelt corners in COMSOL

Next, we will create an outer boundary for the space and a PML layer. By clicking the "ellipse/circle (centered)" button in Draw Mode, and modifying the object properties, as above, two circles should be created: an outer boundary (r=750nm is more than sufficient) and an inner boundary where the PML will start (r=550nm, in this case). Our simulation space and PML will be simply the dielectric of oil, but the frequency-dependent dielectric function of the gold nanobelts is more complicated and can be manually defined for COMSOL via a text file as follows:

```
lib.version.name='COMSOL 3.4';
```

```
lib.version.ext='';

lib.name='User Materials';

lib.descr='';

lib.mat{1}.name='Gold (J&C)';
lib.mat{1}.variables.nu='0.44';
lib.mat{1}.variables.epsilonr='jcEpsReal(nu_rfweh)';
lib.mat{1}.variables.rho='19300[kg/m^3]';
lib.mat{1}.variables.E='78e9[Pa]';
lib.mat{1}.variables.C='129[J/(kg*K)]';
lib.mat{1}.variables.sigma='2*pi*epsilon0_rfweh*nu_rfweh*jcEpsImag(nu_rfweh)';
lib.mat{1}.variables.alpha='14.2e-6';
lib.mat{1}.variables.n='jcN(nu_rfweh)+j*jcK(nu_rfweh)';
lib.mat{1}.variables.T0='298.15[K]';
lib.mat{1}.variables.k='316[W/(m*K)]';
clear fcns
fcns{1}.type='interp';
fcns{1}.name='jcEpsReal';
fcns{1}.method='linear';
fcns{1}.extmethod='extrap';
fcns{1}.x={'1.5475131e+14','1.8618517e+14','2.1520105e+14', ...
  '2.4663491e+14','2.7565078e+14','3.0466665e+14','3.3610051e+14', ...
  '3.6511638e+14','3.9655024e+14','4.2556611e+14','4.5458199e+14', ...
  '4.8601585e+14','5.1503172e+14','5.4646558e+14','5.7548145e+14', ...
  '6.0449732e+14','6.3593118e+14','6.6494705e+14','6.9638091e+14', ...
  '7.2539679e+14','7.5441266e+14','7.8584652e+14','8.1486239e+14', ...
  '8.4629625e+14','8.7531212e+14','9.0432799e+14','9.3576185e+14', ...
  '9.6477772e+14','9.9621159e+14','1.0252275e+15','1.0542433e+15', ...
  '1.0856772e+15','1.1146931e+15','1.1461269e+15','1.1751428e+15', ...
  '1.2041587e+15','1.2355925e+15','1.2646084e+15','1.2960423e+15', ...
  '1.3250581e+15','1.354074e+15','1.3855079e+15','1.4145237e+15', ...
  '1.4459576e+15','1.4749735e+15','1.5039893e+15','1.5354232e+15', ...
  '1.5644391e+15','1.5958729e+15'};
fcns{1}.data={'-189.042','-125.3505','-90.426461','-66.218525','-51.0496', ...
  '-40.2741','-32.040669','-25.811289','-20.610164','-16.817709', ...
  '-13.648209','-10.661884','-8.112669','-5.842125','-3.946161', ...
  '-2.278289','-1.702701','-1.758996','-1.692204','-1.702164','-1.649404', ...
  '-1.604889','-1.400625','-1.231956','-1.310241','-1.169489','-1.230804', ...
  '-1.242549','-1.227421','-1.306784','-1.332261','-1.366509','-1.346409', ...
  '-1.236501','-1.080444','-0.891261','-0.744529','-0.616896','-0.551009', ...
  '-0.4155','-0.346329','-0.233769','-0.1325','-0.010416','0.138171', ...
  '0.203899','0.292524','0.295191','0.227056'};
fcns{2}.type='interp';
fcns{2}.name='jcEpsImag';
fcns{2}.method='linear';
fcns{2}.extmethod='extrap';
fcns{2}.x={'1.5475131e+14','1.8618517e+14','2.1520105e+14', ...
  '2.4663491e+14','2.7565078e+14','3.0466665e+14','3.3610051e+14', ...
  '3.6511638e+14','3.9655024e+14','4.2556611e+14','4.5458199e+14', ...
  '4.8601585e+14','5.1503172e+14','5.4646558e+14','5.7548145e+14', ...
  '6.0449732e+14','6.3593118e+14','6.6494705e+14','6.9638091e+14', ...
  '7.2539679e+14','7.5441266e+14','7.8584652e+14','8.1486239e+14', ...
  '8.4629625e+14','8.7531212e+14','9.0432799e+14','9.3576185e+14', ...
  '9.6477772e+14','9.9621159e+14','1.0252275e+15','1.0542433e+15', ...
```

```
  '1.0856772e+15','1.1146931e+15','1.1461269e+15','1.1751428e+15', ...
  '1.2041587e+15','1.2355925e+15','1.2646084e+15','1.2960423e+15', ...
  '1.3250581e+15','1.354074e+15','1.3855079e+15','1.4145237e+15', ...
  '1.4459576e+15','1.4749735e+15','1.5039893e+15','1.5354232e+15', ...
  '1.5644391e+15','1.5958729e+15'};
fcns{2}.data={'25.3552','12.5552','8.18634',' 5.7015',' 3.861',' 2.794', ...
  '1.92542','1.62656','1.27176','1.06678','1.03516','1.37424','1.66054', ...
  ' 2.1113','2.58044','3.81264','4.84438','5.28264',' 5.6492','5.71736', ...
  '5.73888','5.64436',' 5.6092',' 5.598','5.53816','5.42568','5.84584', ...
  '5.79258','5.78034','5.59644','5.49486','5.28242','4.97628',' 4.7223', ...
  '4.49008','4.33846','4.16328','4.05504',' 3.8922',' 3.8252',' 3.7102', ...
  ' 3.6062','  3.51',' 3.3904','3.39682','3.32766','3.28568','3.17592', ...
  '3.04128'};
fcns{3}.type='interp';
fcns{3}.name='jcN';
fcns{3}.method='linear';
fcns{3}.extmethod='extrap';
fcns{3}.x={'1.5475131e+14','1.8618517e+14','2.1520105e+14', ...
  '2.4663491e+14','2.7565078e+14','3.0466665e+14','3.3610051e+14', ...
  '3.6511638e+14','3.9655024e+14','4.2556611e+14','4.5458199e+14', ...
  '4.8601585e+14','5.1503172e+14','5.4646558e+14','5.7548145e+14', ...
  '6.0449732e+14','6.3593118e+14','6.6494705e+14','6.9638091e+14', ...
  '7.2539679e+14','7.5441266e+14','7.8584652e+14','8.1486239e+14', ...
  '8.4629625e+14','8.7531212e+14','9.0432799e+14','9.3576185e+14', ...
  '9.6477772e+14','9.9621159e+14','1.0252275e+15','1.0542433e+15', ...
  '1.0856772e+15','1.1146931e+15','1.1461269e+15','1.1751428e+15', ...
  '1.2041587e+15','1.2355925e+15','1.2646084e+15','1.2960423e+15', ...
  '1.3250581e+15','1.354074e+15','1.3855079e+15','1.4145237e+15', ...
  '1.4459576e+15','1.4749735e+15','1.5039893e+15','1.5354232e+15', ...
  '1.5644391e+15','1.5958729e+15'};
fcns{3}.data={'0.92','  0.56','  0.43','  0.35','  0.27','  0.22', ...
  '0.17','  0.16','  0.14','  0.13','  0.14','  0.21','0.29', ...
  '  0.43','  0.62','  1.04','  1.31','  1.38','1.45','  1.46', ...
  '  1.47','  1.46','  1.48','   1.5','1.48','  1.48','  1.54', ...
  '  1.53','  1.53','  1.49','1.47','  1.43','  1.38','  1.35', ...
  '  1.33','  1.33','1.32','  1.32','   1.3','  1.31','   1.3', ...
  '   1.3','1.3','   1.3','  1.33','  1.33','  1.34','  1.32', ...
  '  1.28'};
fcns{4}.type='interp';
fcns{4}.name='jcK';
fcns{4}.method='linear';
fcns{4}.extmethod='extrap';
fcns{4}.x={'1.5475131e+14','1.8618517e+14','2.1520105e+14', ...
  '2.4663491e+14','2.7565078e+14','3.0466665e+14','3.3610051e+14', ...
  '3.6511638e+14','3.9655024e+14','4.2556611e+14','4.5458199e+14', ...
  '4.8601585e+14','5.1503172e+14','5.4646558e+14','5.7548145e+14', ...
  '6.0449732e+14','6.3593118e+14','6.6494705e+14','6.9638091e+14', ...
  '7.2539679e+14','7.5441266e+14','7.8584652e+14','8.1486239e+14', ...
  '8.4629625e+14','8.7531212e+14','9.0432799e+14','9.3576185e+14', ...
  '9.6477772e+14','9.9621159e+14','1.0252275e+15','1.0542433e+15', ...
  '1.0856772e+15','1.1146931e+15','1.1461269e+15','1.1751428e+15', ...
  '1.2041587e+15','1.2355925e+15','1.2646084e+15','1.2960423e+15', ...
  '1.3250581e+15','1.354074e+15','1.3855079e+15','1.4145237e+15', ...
  '1.4459576e+15','1.4749735e+15','1.5039893e+15','1.5354232e+15', ...
  '1.5644391e+15','1.5958729e+15'};
fcns{4}.data={'  13.78','  11.21','  9.519','  8.145','   7.15','   6.35', ...
```

```
  ' 5.663',' 5.083',' 4.542',' 4.103',' 3.697',' 3.272',' 2.863', ...
  ' 2.455',' 2.081',' 1.833',' 1.849',' 1.914',' 1.948',' 1.958', ...
  ' 1.952',' 1.933',' 1.895',' 1.866',' 1.871',' 1.833',' 1.898', ...
  ' 1.893',' 1.889',' 1.878',' 1.869',' 1.847',' 1.803',' 1.749', ...
  ' 1.688',' 1.631',' 1.577',' 1.536',' 1.497','  1.46',' 1.427', ...
  ' 1.387','  1.35',' 1.304',' 1.277',' 1.251',' 1.226',' 1.203', ...
  ' 1.188'};
lib.mat{1}.functions = fcns;
```

This text file can be uploaded under Options -> Materials/Coefficients Library, then clicking the button "Add Library". Under Physics -> Subdomain Settings, the nanobelts subdomains (2 & 3) should be specified as gold (under the Physics tab), while the other subdomains (1 & 4) are defined as n=1.5. For the largest domain (4), under the PML tab, we select "Cylindrical" and the other fields will auto-fill. We are now done with Subdomain Settings and click "OK".

Next, we select Physics -> Boundary Settings. The outmost boundary, which can be selected on the left side, or by clicking the lines in the simulation space, must be set to a "Scattering boundary condition" with "Plane wave" selected as the "Wave type". Not that it is useful to check the "Select by group" box here. After clicking "OK', we go to Physics -> Application Mode Properties, we want to select "Free Space Wavelength" from the "Specify wave using:" drop-down box, then select "OK". Under Physics -> Scalar Variables, we can specify an incident plane wave. In this case, the incident magnetic field is defined as $H_o = \frac{n^2}{120\pi} e^{iky}$, which will be written as ((exp(-j*k0_rfweh*y))/((120*pi/(1.5^2))) in the "H0iz_rfweh" field. There is no need to specify the wavelength here, as we will override that field in a next step. Under Solve -> Solver Parameters (or the  button), we will select the "Parametric" solver from the left column and, under the General tab, define the "Parameter Name" as "lambda0_frweh".

Under “Parameter Values”, we define the wavelengths we want to solve for. In this case, that is usually just the excitation and emission wavelengths of the particular Raman mode being studied, or many more wavelengths in the case of calculating a full spectrum. For the “Linear system solver”, we select “Direct (PARADISO)”. “GMRES” is also good if the former option will not run on a specific system (

Figure 62).

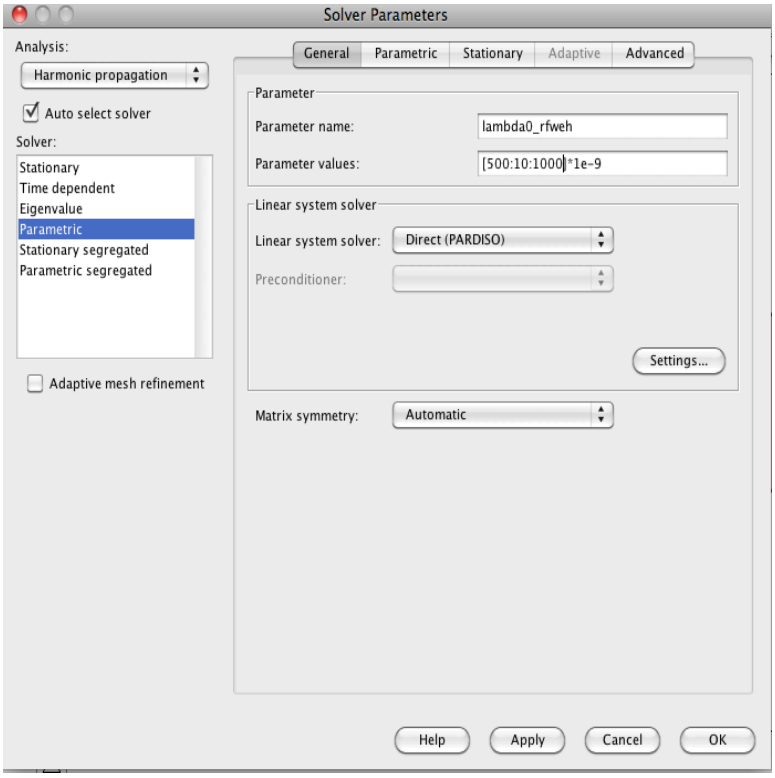

Figure 62 Solver Parameters window in COMSOL.

Next, we will create a mesh. The size of the mesh domains must be sufficiently small to get a good solution. For 2D problems, computational power should not be a problem and it is quite easy to obtain a good mesh. COMSOL has a complicated algorithm for creating the mesh, but we can specify sensitive regions of the simulation for

which we want to impose restraints. Under Mesh -> Free Mesh Parameters, we define a global “Maximum element size” of 50nm or so, with a Element growth rate of 1.3. Under the Subdomain tab, we can specify a very small maximum element size for the nanobelts themselves, (~1nm, 1.1 element growth rate is good), and possibly an even smaller size on the boundaries in the gap under the Boundaries tab. Under Mesh -> Mesh Visualization Parameters, we can check the Element color box and select “Quality” to see how good of a mesh we are getting. Now, we Initialize Mesh under the Mesh menu, and it will be displayed with a color scale that represents the quality of each element (Figure 63).

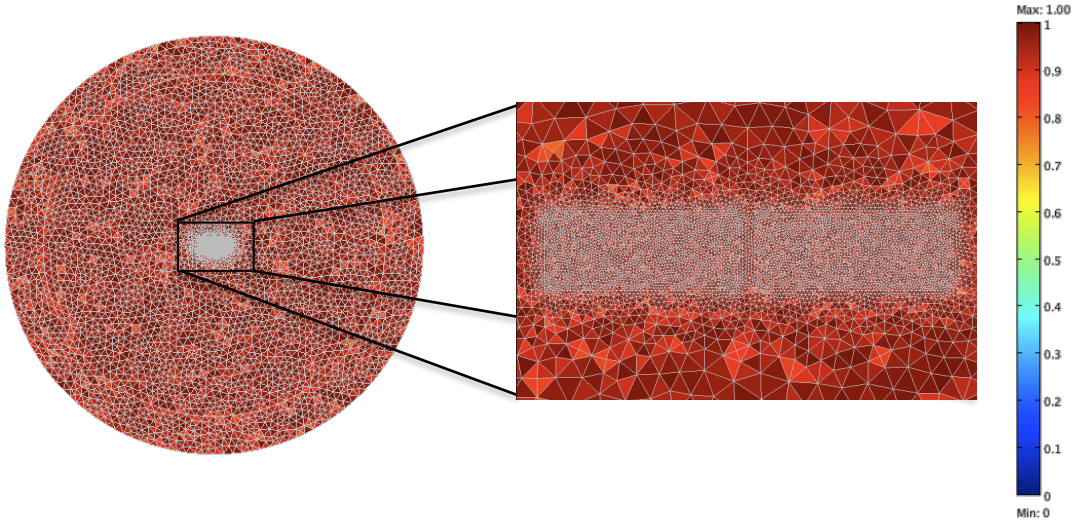

Figure 63 The COMSOL mesh with elements rated on their mesh quality from 0 to 1.

If the mesh quality is sufficient, we are ready to solve. Simply click the = button, the solution should take on the order of minutes, depending on how many wavelengths are being solved for. When the problem is solved, the “Progress” window will close and the solution should be plotted in the space. We have the option of plotting many different variables. In this problem, however, we are solely interested in the total electric field.

Under Postprocessing -> Plot Parameters, we select the “Surface” tab and select “Electric Field, norm” from the “Predefined quantities” drop-down box. Here we can also manipulate other plot properties, such as the color and scale. In this same window, under the “General” tab, we can select the wavelength solution we want to use, under the “Parameter Value” drop-down box. This gives us a nice color plot of the electric field enhancements, like Figure 41 and Figure **42**. For a spectrum of the electric field enhancements at a specific point, we select Postprocessing -> Cross section Plot Parameters. Under the “General” tab, we select “Point plot”, and make sure all of the wavelengths are highlighted in the “Solutions to use” section. We then go to the “Point” tab and select “Electric Field, norm” from the “Predefined Quantities” drop-down box then define the point (x,y). In this case, the point (0,0) was investigated, as it is centered in the gap. Upon clicking “OK”, a spectral plot will be generated, as in Figure 43 and Figure 44.

Appendix E: Mie Scattering from an Infinite Cylinder

```
r(j) = 5e-9; %cylinder radius
nm = 1.5; %index of refraction (n) of surrounding medium
n = gold_dielectric(:,2); %n gold
k = gold_dielectric(:,3); %k gold
l = gold_dielectric(:,1); %wavelength

for L = 1:10

   for t = 1:length(n)
      m = (n(t)+i*k(t))/nm;
      kn = (2*pi*nm)/(l(t)*10^(-9));
      x = kn*r(j);
      Dn_x = ((L*besselj(L, x))/x - besselj(L + 1,x))/(besselj(L,x));
          Dn_mx = ((L*besselj(L, m*x))/(m*x) –
                 besselj(L + 1,m*x))/(besselj(L,m*x));

a(L,t) = (((Dn_mx/m)+(L/x))*besselj(L,x)-   besselj(L1,x))/(((Dn_mx/m)+(L/x))*
besselh(L,x)-besselh(L-1,x));

b(L,t) = (((m*Dn_mx)+(L/x))*besselj(L,x)-
besselj(L-1,x))/(((m*Dn_mx)+(L/x))*besselh(L,x)-besselh(L-1,x));

w(t) = l(t);

   end %end t-loop

end %end L-loop

sc_per = (2/x)*((abs(a(1,:))).^2 +
2*((abs(b(2,:))).^2+(abs(a(2,:))).^2+(abs(b(3,:))).^2+(abs(a(3,:))).^2+(abs(b(4,:))).^2+(ab
s(a(4,:))).^2+(abs(b(5,:))).^2+(abs(a(5,:))).^2+(abs(b(6,:))).^2+(abs(a(6,:))).^2+(abs(b(7,:)
)).^2+(abs(a(7,:))).^2+(abs(b(8,:))).^2+(abs(a(8,:))).^2+(abs(b(9,:))).^2+(abs(a(9,:))).^2+(
abs(b(10,:))).^2+(abs(a(10,:))).^2));

sc_par = (2/x)*((abs(b(1,:))).^2 +
2*((abs(b(2,:))).^2+(abs(a(2,:))).^2+(abs(b(3,:))).^2+(abs(a(3,:))).^2+(abs(b(4,:))).^2+(ab
s(a(4,:))).^2+(abs(b(5,:))).^2+(abs(a(5,:))).^2+(abs(b(6,:))).^2+(abs(a(6,:))).^2+(abs(b(7,:)
)).^2+(abs(a(7,:))).^2+(abs(b(8,:))).^2+(abs(a(8,:))).^2+(abs(b(9,:))).^2+(abs(a(9,:))).^2+(
abs(b(10,:))).^2+(abs(a(10,:))).^2));
```